The Aero-Thermal Impact of Rim Seal Purge Flow in Axial Turbines

Zum Aero-Thermalen Einfluss der Sperrluft in Axialturbinen
Zur Erlangung des akademischen Grades Doktor-Ingenieur (Dr.-Ing.)
Genehmigte Dissertation von Tom Ostrowski aus Aachen
Tag der Einreichung: 18.04.2023, Tag der Prüfung: 31.05.2023

1. Gutachten: Prof. Dr.-Ing. H.-P. Schiffer
2. Gutachten: Prof. G. Paniagua, Ph.D.
Darmstadt – Technische Universität Darmstadt

TECHNISCHE UNIVERSITÄT DARMSTADT

Fachbereich Maschinenbau

Fachgebiet Gasturbinen, Luft- und Raumfahrtantriebe

The Aero-Thermal Impact of Rim Seal Purge Flow in Axial Turbines
Zum Aero-Thermalen Einfluss der Sperrluft in Axialturbinen

Genehmigte Dissertation von Tom Ostrowski

Tag der Einreichung: 18.04.2023
Tag der Prüfung: 31.05.2023

Darmstadt – Technische Universität Darmstadt

Bitte zitieren Sie dieses Dokument als:
URN: urn:nbn:de:tuda-tuprints-244833
URL: http://tuprints.ulb.tu-darmstadt.de/24483
Jahr der Veröffentlichung auf TUprints: 2023

Dieses Dokument wird bereitgestellt von tuprints,
E-Publishing-Service der TU Darmstadt
http://tuprints.ulb.tu-darmstadt.de
tuprints@ulb.tu-darmstadt.de

Abstract

The area between the stationary and rotating hub side endwall segments in axial turbines is featured with a specifically shaped annular clearance, termed as the rim seal. For the safe and reliable operation of a gas turbine, this seal depicts a pivotal component. The main design intent is to avoid the ingress of hot main flow to the vulnerable wheel-spaces in the inside of the turbine. To guarantee sealing, the internal cavities are permanently supplied with pressurized air. Termed as rim seal purge flow, a specific fraction is continuously passing the seal, before it is mixed with the main flow.

It is known, that rotating large scale instabilities in the rim seal region can effect or even dominate the spatio-temporal character of the flow field in the adjacent blade rows. Being superimposed by the unsteady stator-rotor interaction, appropriate test environments need to account for this multi-dimensional interdependency.

In a large scale, rotating turbine test facility, the model of a high pressure axial turbine stage is experimentally investigated. The flow characteristic in the seal region is altered by adjusting the purge flow mass fraction. In the scope of this work, experimentally determined flow quantities in the stator-rotor interface, the seal and the rotating blade row are combined with unsteady, three-dimensional computational fluid dynamics targeting the deviation of the spatio-temporal characteristic of the rim seal purge flow. The numerical setup represents a sixty degree sector of the stage including the seal and sub-cavity. The calculations are initiated with experimentally determined flow data at the boundaries. For validation, results are spot checked with selected unsteady experimental flow data.

To globally rate the effect of the purge flow, a framework of one-dimensional performance parameters is presented, in which a thermodynamically sound definition of the ideal reference process accounts for the unavoidable entropy of mixing. By increasing the dimensions considered, the spatio-temporal description of the stage is first introduced at mid-span. Visualizing the three-dimensional distribution of vortical structures, the spatio-temporal character of the interaction of main and purge flow is finally introduced.

Contents

1 Introduction and State of the Art

1.1 Motivation

Reaching greenhouse gas (GHG) neutrality is of major importance for a sustainable and safe continuance of modern societies. The conclusion of COP 21 in Paris (Paris Agreement) can probably be seen as the most extensive and visible measure for the attempt to guarantee a humanly friendly habitat for our species. Its main goal of limiting the global warming well below 2 °C, preferably to 1.5 °C, compared to the pre-industrial level, is evidentially connected with a transformation of our customary way of producing and consuming energy. The necessary changes are of global scale and the socio-economic challenges are on a barely conceivable level.
Besides the aspects concerning the global warming, a reliable and independent energy supply is forced towards renewable sources for a second reason. The finiteness of fossil fuels increases the competition for resources. Regions with little raw materials are historically dependent on energy imports with incalculable consequences for the long-term political stability. This fact has recently lead to a radical rethinking of unilateral dependencies. For Europe, the Russian invasion in Ukraine end of February 2022 has shown the difficulties related with its high import rates of Russian natural gas, coal and oil quite plainly. For the European Union (EU) the conflict is a painful reminder to diversify energy sources with a simultaneous reduction of its power consumption.
Germany's strategy on fulfilling its climate goals is closely embedded into the climate and energy framework of the EU. In the *European Union energy and climate policies* a clear roadmap to climate neutrality by 2050 is established. There are various technologies available to theoretically realize the energy transition towards a climate-neutral continent. Referencing the EU Strategy for Energy System Integration (COM [14]), the solution however will most probably be an integrated energy system where different infrastructures, energy carriers and consumption sectors are linked and considered as *a whole*.
There are many publicly available studies on forecasting the pathway on how the energy transformation will possibly look like in detail. All scenarios have in common that a tremendous increase in scalable renewables will depict the backbone of the power supply at mid-century. The EU decarbonization targets for 2030 highlight the increasing demand of renewable energy in the power secotor, see Fig. 1.1a, Agora Energiewende (2019) [1]. As hydro-power and bio-methane are limited by natural restrictions, the main proportion will be provided by wind and solar power-plants. The direct electrification on the consumer side is seen to be the most efficient way to phase-out fossil resources. The possible share of highly-electrified substitutions of current carbon-based technologies however depends strongly on the respective sector. As an example, the heating of buildings and short-distance road traffic is comparably easy to electrify, long distance transportation such as intercontinental shipping and aviation are not. Even with the most optimistic progress in battery-technology, electrochemical

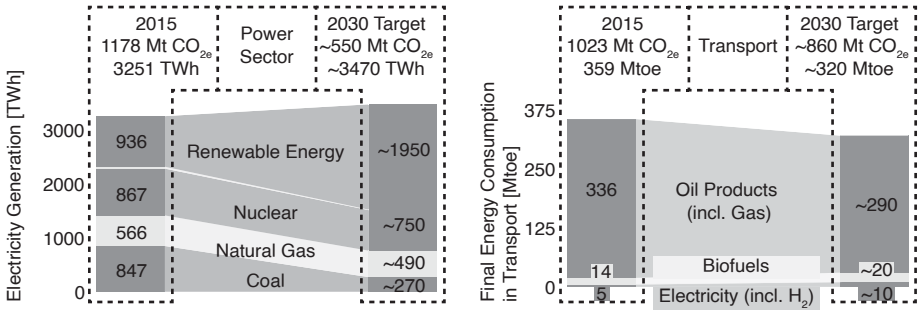

(a) Decarbonization targets in the power sector

(b) Decarbonization targets in the transport sector

Figure 1.1: EU emissions targets 2030 highlight the increasing demand of renewable energy in the power sector and simultaneously the limited potential in transportation. In both sectors, highly efficient gas turbines play an important role. Design and data adapted from Agora Energiewende (2019) [1].

storage capacities will be far away from the demands for long-haul transportation. All long-term forecasts therefore do not see alternatives to chemically based storage [1] systems for these two applications.

Due to the fluctuating character of wind and solar energy, the power sector itself will depend on reliable storage technologies, leaving the track of direct electrification. Again, various scenarios differ in forecasting the appropriate technological solution to guarantee a sustainable, cost-effective and resilient power production. In fact, multiple approaches are technically mature and compete against each other. On the sense of grid-scale seasonal energy storage, these are namely pumped-storage hydroelectricity, compressed air energy storage, grid-scale batteries and power-to-gas applications. All methods have their individual advantages and will play their role in an interconnected storage approach. However, a true resilience of the European electric grid against a potential *kalte Dunkelflaute* [2] or natural disasters with a temporal negative effect on the renewable energy production calls for large scale storage capacities. Even with technological improvements of e.g. battery chemistry or advanced geothermal storage, market trends indicate an important role of re-electrification of green hydrogen.

As indicated so far, their are two significant sub-sectors, where the direct use of wind and solar based electricity will most probably remain impossible in the foreseeable future. As depicted in Fig. 1.1, the short term decarbonization targets for the transport

[1] chemically based storage covers the whole range of e-fuels and power-to-X, which are based on green hydrogen and synthetic hydro-carbons

[2] common industrial term in Germany for "'dark doldrums'", i.e. prolonged simultaneous lulls in wind and solar generation (Agora Energiewende (2021) [2]).

sector mirrors some of the difficulties, as mentioned so far. From an engineering perspective, what are now the responsibilities to be solved for? Well, for both, the long-haul transportation as well as for the resilient electric grid operation, technologies are needed for the most cost-effective, reliable and after all sustainable conversion of the chemically bounded and stored renewable energy. As the exact applications differ in their needs concerning the power density, performance category, durability, acceptance of investment costs and so on, a general answer cannot be given. For long-distance shipping, there are much less restrictions concerning the power density of the driving unit than it is true for aviation. Same counts for the volume specific heating value of the fuel. Hence, for the decarbonization of marine shipping, various technologies are feasible. To name the most significant, the use of fuel cells, internal combustion engines and gas turbines running on green fuels are most probably the concept of choice. Fuels may be gaseous or liquid, as volume is not of major concerns in shipping. What will remain is the necessity to decarbonize long-haul aviation.
Gas turbine technology is currently the concept of choice for both named critical subsectors, namely the efficient electrification of liquid and gaseous fuels as well as to provide the propulsion in aviation (not limited to long-haul flights). Now, what is expected to be the role of gas turbines in the mid- and long-term future? In the energy sector, gas turbines are widely seen to be suitable to compensate for the fluctuating wind and solar power output. The wide operational range of modern gas turbines are well established to stabilize the electrical grid. Fired with sustainable fuel, e.g. stored or imported green hydrogen, they can securely deliver the power over periods with little sustainable energy supply. In Europe, this will most probably be the winter due to the high energy demands for electric heating, with simultaneous little solar capacity. As recent investigations have shown, an efficient re-electrification of hydrogen in a Combined Cycle Gas Turbine (CCGT) power plant with the use of heat pumps for residential heating is more efficient than a direct firing in local hydrogen boilers (compare Agora Energiewende (2021) [2]). If, at the end, gas turbines will keep a significant share in grid scale storage of renewables, is a question of their life-cycle costs and efficiencies. Currently, heavy Gas Turbine Combined Cycle (GTCC) power plants can offer over 60 % thermal efficiencies [3] with comparable little maintenance costs and tens of thousands of operating hours. However, the long-term perspective for heavy duty gas turbines with overall power outputs in the Gigawatt-range must be seen critical. For the re-electrification of green fuels the use of decentralized small and mid-size industrial turbines and aero-derivatives are more suitable for the local compensation of fluctuations in the electric grid. In this case, the overall efficiency drops significantly down to approximately 40 % (now without CCGT) but with the potential of enabling a more transient operation and to co-generate heat.
To conclude, the exact transformation of the power sector remains hard to forecast. Most likely, it be will strongly diversified and depend on the local availability of renew-

[3] e.g., the heavy duty gas turbine SGT5-8000H reached a combined net efficiency of 60.75 % in 2011 (Gülen [24])

able sources, natural storage potentials [4], policies, public acceptance and much more. For Germany, a country with currently high energy import rates and limited renewable potential, a net-zero energy market will dependent on imports. The imported energy can be electrical or chemical based and their share is a question of the overall strategy. With a look to the current global political landscape, a quick desertification however is of highest interest and the gas turbine will have its role in providing safe, reliable and panic-proof electricity.

Concerning the trends in powering next generation aircraft, scenarios differ in forecasting a climate-neutral and environmental friendly aviation. Many international aviation organizations regularly depict road maps on how to reach the overall target of net-zero aviation by 2050. Important to note is, that the global warming effect of aviation is not limited to Carbon Dioxide (CO_2) as jet engines, despite others, also emit nitrogen oxides (NO_x) [5] and create cirrus clouds as formed from the contrails.

On a global scale, the International Civil Aviation Organization (ICAO) formulates a regulatory framework to meet the climate goals as internationally confirmed by the Paris Agreement. As concluded in the 2019 Environmental Report ICAO [33], on a technical basis the further reduction of aviation climate impact will be a combination of substituting fossil kerosine with sustainable aviation fuels [6], aircraft technology improvements [7] and operational improvements. In its recently published report on the feasibility of a Long Term Global Aspirational Goal (LTAG) for international civil aviation ICAO [34], the ICAO Committee on Aviation Environmental Protection (CAEP) has presented a complex and in-depth analysis on the most possible developments on the path towards zero-emission aviation. The report shows mainly three scenarios with different assumptions on the shares of improvements in technology, fuels and operations. Even the most ambitious scenario [8], representing the maximum possible effort in terms of future technology roll-out, operational efficiencies and fuel availability, forecasts the need for highly efficient, but still conventional jet engine systems for the long-term period far over the 2050s ahead.

The results of the publicly funded CAEP-study generally coincides with the prospect of the industrial funded Air Transport Action Group (ATAG) as presented in their WAYPOINT 2050 forecast ATAG [4]. With reference to Fig. 1.2a, the inclusion of different efficiency development forecasts into the global aircraft fleet is sketched. The reports present conclusive reasoning, that the mid-term perspective of the propulsion system of medium- and long-haul aircraft will basically follow the turbofan-concept. In the foreseeable future, the only way towards carbon-neutrality of intercontinental

[4] salt and rock caverns, aquifers, depleted fields and so on

[5] NO_x has the potential to form ozone when emitted in high altitudes

[6] often distinguished between drop-in fuels or Sustainable Aviation Fuels (SAF) (bio-fuels and synfuels) and green hydrogen, see i.e. Zhou et al. [71]

[7] most likely an increase in efficiency of both, the aircraft body and propulsion system including radical innovations such as Blended Wing Body (BWB) and full or hybrid electric propulsion

[8] CAEP LTAG Integrated Scenario 3 - IS3, assumptions summarized in ICAO [36]

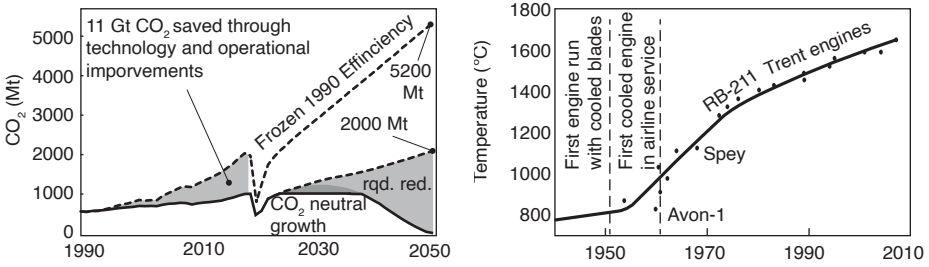

(a) Efficiency improvements and inclusion scenarios into the global aircraft fleet, adapted from ATAG [4]

(b) Turbine Inlet Temperature development of Rolls Royce Jet Engines, adapted from Saravanamuttoo et al. [58]

Figure 1.2: The interconnection of super-efficient aircraft propulsion systems to meet decarbonization goals and the historical development of turbine inlet temperatures

flights will then be the efficient and clean combustion of SAF. As their production is energy- and resource-intensive, a low Specific Fuel Consumption (SFC) will remain a central development target of next generation jet engines, as it always was for civil aviation. A comprehensive justification, why it is currently not seen to be possible to use carbon-free propulsion systems in long-haul aviation is reported by the LTAG Technology Sub Group in ICAO [35].

1.2 Cycle Performance and the High Pressure Turbine

Having highlighted the global long-term need for highly-efficient gas turbines and jet engines, the interconnection to the research topic of this dissertation is now given. Even if both applications serve completely different purposes, namely driving aircraft and vice versa producing electric energy, they are based on the exact same thermodynamic principal, namely the Joule-Brayton Cycle (JBC). As true for all heat engines, the JBC targets the conversion of heat to mechanically usable energy. To introduce, the main components of a gas turbine are depicted in their thermodynamic and turbo machinery representation, see Figs. 1.3a and 1.3b. In Fig. 1.3c, the corresponding idealized thermodynamic cycle is shown in a temperature-entropy chart. As will be discussed in the following, this configuration is termed a turbo-shaft and can be seen as the most simple representative for both, stationary gas turbines and the vast majority of modern aircraft engines. Highlighting the strong idealization, the process, as depicted in the chart, follows a sequence of four basic thermodynamic processes.

Pressure and temperature of the working fluid, in this case an ideal compressible gas with constant properties, is increased in the compressor section from state 1 to state 2. For the ideal cycle, this compression is adiabatic and reversible [9]. The temperature

[9] thermodynamically, an adiabatic and reversible process is isentropic

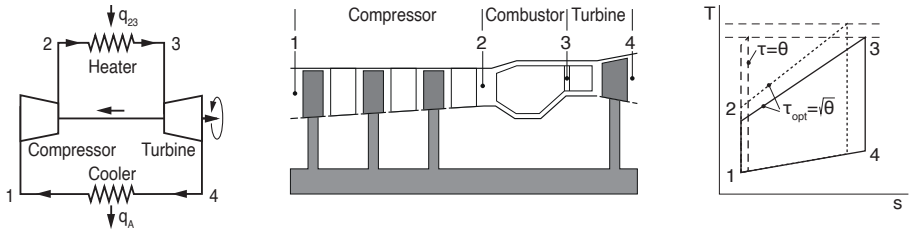

(a) Thermodynamic representation of the ideal gas turbine

(b) Turbo-machinery representation of the ideal gas turbine

(c) Thermodynamic states in the T-s diagram

Figure 1.3: The ideal Joule-Brayton cycle is the most simple thermodynamic representation of a gas turbine, where a compression, heat addition, expansion and heat release define the four thermodynamic processes.

of the fluid is then further increased, now at constant pressure, adding heat reaching state 3. The pressurized and heated fluid at state 3 is highly energetic and ready to be converted into mechanically usable power in the turbine. However, not all of the energy is net output, as the compressor power has to be delivered continuously. In the most simple configuration, this is realized by a shaft, connecting the turbine to the compressor unit. Thermodynamically, the gas has still a higher state, compared to 1. To deliver any net mechanical output, the gas is therefore further expanded in the turbine to state 4. This shaft power corresponds to the cycle output, where it is transferred to the appropriate device or application. For a ground based stationary gas turbine, the shaft is coupled to an electric generator and the shown configuration is an exact representative of such systems.

For aircraft propulsion, the shown configuration is close to the turbo-fan jet engine architecture. However, the exact configuration mostly differ, as the second expansion is usually realized in an extra turbine, which is then driving the fan, usually termed as the low pressure unit. In difference to the turbine for electric power production, the remaining energy after the turbine is expanded through a nozzle to produce thrust.

For both applications, land based and aircraft propulsion, there are various practical concepts, leading to a specific arrangement and interconnection of the low and high pressure segments. However, all of the variants share a common unit; the so called gas generator [10].

As gets clear from basic cycle analysis, it is the aero-thermal capability of the gas

[10] synonymously often named the core unit consisting of the high pressure compressor, the combustion chamber and the high pressure turbine. For single spool stationary gas turbines, a clear definition of a gas generator is not as clear, because the whole system runs on one single shaft. However, the turbine has usually still a distinguishable high pressure section.

generator, which is limiting the cycle performance. For the JBC, the general expression for the thermal efficiency ends up to be a function of pressure ratio only. With $\pi = p_2/p_1$ expressing the compressor ratio and $\tau = T_2/T_1$ the corresponding isentropic temperature ratio, the expression for the thermal efficiency can be written as

$$\eta_{\mathrm{th}} = \frac{w_{out}}{q_{in}} = \frac{w_{\mathrm{t}} - w_{\mathrm{c}}}{q_{23}} = 1 - \frac{1}{\tau} = 1 - \frac{1}{\pi^{\gamma-1/\gamma}} \tag{1.1}$$

For a given maximum cycle temperature ratio $\theta = T_3/T_1$, the highest thermal efficiency ends up to be reached for $\tau = \theta$. However, as in this hypothetical case no heat could be added between states 2 and 3, the cycle would degenerate to a single isentrope, and no net output is available, compare the dash-dotted cycle on the right in Fig. 1.3c. To conserve the specific power output, while increasing the pressure ratio, θ has to be increased simultaneously. The extractable work, as defined in the enumerator of Eq. (1.1), can be written in the normalized formulation

$$\bar{w}_{out} = \frac{w_{out}}{c_{\mathrm{p}} T_1} = (\frac{\theta}{\tau} - 1)(\tau - 1) \tag{1.2}$$

Equations (1.1) and (1.2) , as the result of the ideal, air-standard cycle analysis show, that the combination of τ and θ define the thermal efficiency and the specific work of the machine [11]. The thermal efficiency is a major contributor to the specific fuel consumption, whereas the specific work represents the power density or more generally the size of the gas turbine, when a absolute power output is given. Clearly, there is no easy answer on how to choose the respective ratio of these two key variables. In the real world, their practical choice is embedded into the complex design strategy and depends on the specific application and its operating conditions. The possible range however is limited by technological constraints. The question is, which of the two parameters is more restricted.

Leaving theory behind, now looking into the real world of compressors and turbines, it can be easily shown that the choice falls on the maximum cycle temperature. Thus, for a given θ, the pressure ratio must be somehow aligned. To give an overall expression for an *appropriate* pressure ratio, a first approach can be to target a maximum of the specific work. Mathematically, this is done by setting to zero the first derivative of the specific work with respect to τ

$$\frac{\mathrm{d}\bar{w}}{\mathrm{d}\tau} = \frac{\theta}{\tau^2} - 1 = 0 \rightarrow \tau_{opt} = \sqrt{\theta} \rightarrow \pi_{opt} = \theta^{\frac{\gamma}{2(\gamma-1)}} \tag{1.3}$$

The expression highlights, that the optimum pressure ratio relates exponentially to θ. For an ideal gas with a constant heat capacity ratio of $\gamma = 1.4$, this exponent takes a value of 1.75. Hence, the relation is close to quadratic. To sum up, a higher T_3 is the

[11] assuming a constant and predefined c_{p} and compressor inlet temperature T_1

key parameter to significantly allow higher pressure ratios, with its positive effect on the thermal efficiency, superimposed by an increase of the specific work.
Now, what is the technical conclusion to this statement? It is the Turbine Entry Temperature (TET), identified to be the bottleneck towards more efficient and compact gas turbines. Surely, the argumentation is highly simplified, but the key message well reflects the observed developments in the gas turbine sector. However, it must be stated at this point, that real cycle analysis is of a different level of complexity and the validity of the correlations, as derived so far, is reduced. By replacing the isentropic compression and expansion by polytropic processes, the exclusive dependency of the thermal efficiency on the pressure ratio is not given anymore. Besides, the real fluid properties have to be taken into account. Incorporating these *true* circumstances into a parametric cycle analysis is possible and may still be represented by analytical correlations, together with the thermodynamics of real gases. The outcome, though, is not generally weakening the significance of the TET.
A concise description of the thresholds to higher efficiencies can be as follows. Where compressor Research and Development (R&D) is mainly driven by aerodynamic and structural questions, on the turbine side the focus is more on thermal issues, dealing with explicit physical limits. First of all, the temperature resistance of the flow guiding structure [12] downstream the combustion chamber is historically limiting the possible temperature level. Methods to increase the TET were mainly coming from two different disciplines. On one side, the materials science, on the other the cooling technologies. Technologically, the combined evolution of both disciplines has led to impressive turbine inlet temperatures, being in the range of 1800 K to 1900 K for modern civil aircraft engines, see Figure 1.2b.
In the context of thermal efficiency, the value of TET however must be handled with care. This is primarily connected to the aforementioned cooling techniques. In the vast majority of applications, relatively cold bleed air is applied to adjust the thermal load in the HGP to an acceptable level. As this *cooling air* has to be available at the appropriate pressure, it is for sure not free of charge. For jet engines, and almost all stationary gas turbines [13], the cooling air is extracted from the compressor at the corresponding pressure level, and bypasses the combustor section. As obvious from basic thermodynamic cycle analysis, this portion of air is not able to create any net output. Depending on the losses, which are created in the cooling path and the complex process of re-entering the main flow, the work of compression may just be partially retrieved, when expanded in the subsequent turbine stages. This leads to the fact, that it is not the TET as the main driver of cycle performance.
As there is no work extracted in the first stator, it is more appropriate to define the thermodynamic state at its outlet being the parameter indicative for the maximum cycle temperature. In an early stage of the design process, an exact prediction of this so called Rotor Inlet Temperature (RIT) is hard to realize, as it incorporates

[12] all mechanical structure facing the hot gas is also called the Hot Gas Path (HGP)
[13] some heavy duty gas turbines partly use steam for cooling purposes

the full spectrum of internal and external cooling of the first stator. Heat transfer between and mixing of cooling and main flow produce different losses. Both, the transport of momentum and heat is highly coupled. From an engineering point of view, investigations are then often termed as aero-thermal, and they are surely not limited to the first stator row. As cooling is continued in the first high pressure rotor or and most likely further downstream, a large portion of the complete expansion path is effected by the introduction of turbine cooling.

Compared to an uncooled turbine, loss creation is usually intensified, which highlights a major issue, limiting a further increase of the thermal efficiency of practically realized JBC based machines. Higher TET do not automatically mean better cycle performance. As the gas temperature constantly decreases within the turbine section, the thermal load is naturally most critical in the first stage. The development of the most sophisticated cooling techniques is therefore triggered by getting them applicable in the first nozzle guide vane and the subsequent first blade row, so the first stage of the high pressure turbine (HPT).

The aero-thermal boundary conditions at the combustor-turbine interface has gone through tremendous changes within the last years. Low emission combustion technologies have increased inhomogeneities in the velocity and temperature distribution, compared to conventional concepts. Due to the weight and space constraints, as well as the safety requirements, the implementation of low emission combustors was and still is more challenging for aero engines, compared to ground based systems.

A consequence of very low-NO_x combustion technologies [14] is the redistribution of hot gas portions towards the endwalls, increasing the thermal stress in the hub and shroud regions. For the stationary endwalls, namely those of the stator passage and the rotor casing, [15] thermal management can be realized with well established cooling approaches. Furthermore, the application of step changing materials such as Ceramic Matrix Composites (CMC), are much easier to be implemented into non-rotating assemblies.

On top of the very high thermal load, the first rotor blade row is highly stressed by centrifugal forces. The structural implementation of appropriate cooling strategies is therefore much more driven by strength requirements. The blade hub side region thereby experiences the highest tensile loads, making the implementation of cooling patterns a compromise between cooling and loading capacity.

1.3 Rim Seal Purge Flow

Managing the aforementioned increasing loads within the HGP does not stand alone, when targeting higher maximum cycle temperatures. It is also the prohibition of hot gas ingestion into the cavities and wheel-spaces, as they exist naturally between the

[14] concepts are widely based on lean burn technologies where the majority of the air coming from the combustor takes part on the combustion itself.

[15] for a shroud-less rotor design only

rotating and stationary blade rows. As the turbine discs, the bearings and other internal structural parts had and still have much lower temperature resistances than those located in the main annulus, thermal fatigue needs to be avoided within all possible operating conditions. An unwanted ingress of the hot main flow into the wheel-spaces can quickly cause dramatic damage of structurally mandatory components, which can quickly lead to the failure of the entire machine.

The practical solution to avoid this so called hot gas ingestion is the systematic and guaranteed pressurization of all cavities and wheel spaces, which have a direct connection to the HGP. Following the fundamentals of flow theory [16], the flow field is locally oriented towards the negative gradient of the static pressure. Thus, the ultimate target for a fully sealed cavity could be reached with an evenly distributed and gradient free static pressure field at the respective transition area. If this very unique situation could be technically realized, there would be no sealing mass flow consumed at all, and the only effort to be taken technically would be the exact leveling of the pressurization.

In reality however, the situation at a sealing interface is the exact opposite; the boundary conditions on both sides, namely the internal and external flow and temperature fields, are characterized as highly fluctuating, with large gradients in time and space. Furthermore, a prospective net-zero mass flow within the cavity would often not fulfill internal cooling requirements. Besides a pure ingress of hot gases, it is also heat conduction and radiation, which is threatening the thermal persistence of vulnerable internal components. This additional requirement leads to the need of continuously purging the cavities.

On the basis of that simplified explanation, as given for the mandatory measure of purging the gaps which are facing the HGP, it is the Rim Seal Purge Flow (RSPF) of the first stage of the HPT having a predominant role within the entire sub-system. As the temperature and pressure at the stator exit are still on highest levels, the thermodynamic state of the purge flow itself needs to be conditioned properly to meet that harsh environment. As a consequence, the only practical source for the RSPF in the HPT is to extract it at the compressor outlet section, where it then bypasses the combustor and the first stator.

As mentioned before, the most obvious thermodynamic drawback is, that the RSPF does not fully run through the thermodynamic cycle. While the compression work of the cooling flows, which are injected in the stationary flow guiding structures, can largely be reconverted, the contrary is true for the RSPF upstream of a rotating blade row. On top of that thermodynamic disadvantage, it is the limited potential to adequately condition the seal flow aerodynamically. As the nature of an axial turbine rotor is to de-swirl the main flow, it is the lack of angular momentum of the RSPF being a major drawback to a high portion of recuperation. For this reason, purge flow is often characterized as parasitic. It is the nature of disturbance, which leaves room for optimization.

[16] incompressible, stationary and inviscid, Bernouli

To conclude, the negative thermodynamic cycle effect is superimposed by two addition disadvantages. First, the additional mixing losses and second, the penalties connected to the disturbed rotor passage flow. In general, they all correlate with the mass fraction of injected flow, which leads to the obvious objective to minimize its demand to the lowest possible value. An optimization strategy, though, needs to implement various influencing parameters. The existance of a series of interrelations however makes the search for an optimized seal configuration difficult. Without going into details at this point, first of all, there is the flow guiding geometry, which is primarily effecting the characteristics of the sealing flows.

Now, what are the existing limitations in finding the ultimate strategy of rim sealing in axial gas turbines? It is motivated in a lack of the basic understanding of the underlying phenomenological interdependence of the surrounding components, where each is representing an impressive and highly optimized subsystem of a high pressure turbine. There is the Nozzle Guide Vane (NGV) as the separative element to the upstream combustor section, responsible for the characteristic flow field in the hub side passage endwall region. The stator exit may be dominated by secondary flows and thermal inhomogeneities, both incorporating fluctuations in different time and length scales. Neglecting changes during the variation of the operating point, the temporal mean at the stator exit is fixed. The downstream rotor, in contrast, is represented by a rotating blade row, which, by its own, calls for an undisturbed and homogeneous flow field.

The rim seal itself is located in between the two blade rows. The ejected purge flow characteristic is consequently facing the discrepancy of the stator exit and rotor inlet flow features. At the same time, the purge flow is emerging with its individual pattern, which might have its origin in the internal flow path, where it is mainly dominated by the feeding system and its interaction with the stationary and rotating walls inside the wheel-spaces.

Historically, the optimization of the HPT was dominated by the design of efficient vanes and blades, where the individual thermal management strategy of the profiles was incorporated. Due to the low aspect ratios typically found in high pressure turbine section, the relevant portion of secondary losses then lead to integrated optimization strategies, where the consideration of the passage endwalls and their individual demand for cooling was getting more important. Early approaches, where RSPF was implemented into the design of the turbine geometry, were mainly initiated in linear cascades, neglecting or strongly simplifying the effects of the rotating surrounding.

Driven by the increase in available computing power, the possibility to fully model an entire turbine stage with the seals included, started to become state of the art in turbine research and development. However, the majority of the published work from the last two decades, especially from the application-oriented engine design community, used steady state computations with a mixing plane located somewhere in between stator and rotor. Certainly, the purge flow is globally balanced correctly. However, investigations also showed, that the assignment of the cavity to the stationary or the rotating domain, occasionally had a significant effect on the prediction of the hub

side rotor passage flow field. Such kind of observations are maybe the most obvious motivation, why a trustworthy rating of the rim seal performance in axial turbines is definitely limited, when based on steady state calculations. A similar argumentation is true for the respective experimental counterparts.
Having highlighted the need for fully integrated rim seal investigations, the question of bottlenecks in the optimization strategy arises. It is represented by the massive increase of effort, necessary to realize representative test environments. On the numerical side, there is no way around of using unsteady computations capable of reproducing the dominating spatio-temporal interactions in the stator-rotor interface together with a reasonable part of the respective rim seal configuration. As a consequence, the mesh topologies of such implicit domains are hard to idealize, which inevitably increases the numerical costs. High computing time for a single variant however lowers their value for automated optimization strategies, where often hundreds or thousands of variants need to be simulated.
Finally, the required peripheral resources such as the storage capacity and memory for the systematic data processing, evaluation and archiving is on a different level, when compared to steady state calculations. Looking at the experimental side, the equipment for unsteady, spatio-temporal measurements is of a different scale of compexity, when compared to conventional, steady state measuring systems. For an efficient and robust handling of the experimental data, the argumentation concerning the evaluation strategy is similar to the one, as given for the computational approach.

1.4 Rotating Unsteadiness in the Rim Seal Region

Despite all of the challenges discussed so far, the trend today is definitely towards fully integrated and unsteady optimization strategies for the design of next generation purge flow systems. In the context of this ongoing progress, the detection of a relatively new phenomenon has even intensified the interest of researchers and developers familiar on this specific topic. This is the objective evidence of large scale rotating instabilities, which are induced in the rim seal region of axial turbines. Beginning in the early years of this century, for a whole range of tested configurations, until then unknown pressure fluctuations were proven to be created in the mixing zone of purge and main flow. They are found to be unrelated to the frequencies induced neither by the rotating disc nor the stator-rotor interaction. However, unrelated is only referred to the pattern of rotation, not to the formation itself.
For a distinct investigation of such rotating cavity structures, the requirements for potential experimental and numerical test environments are once more increased. First of all, the configuration needs to allow the formation of the instabilities. Second, circumferential periodicity, often utilized in unsteady numerical approaches [17], is inappropriate, as they can suppress the correct formation of the rotating pattern.

[17] often, unsteady computations in turbo-machinery are solved on sector models representing the correct vane to blade count ratio

Third, the data evaluation procedures, whether predicted or measured, need to allow the deviation of spatio-temporal correlations, which is a contrast to the investigation of unsteady, but harmonic phenomena in turbo-machinery, where the statistics in one dimension, thus in time or in space, are often adequate for a meaningful assessment.

For an optimization strategy, where the potential impact of non-harmonic fluctuations in the rim seal region is to be considered, automated approaches are difficult to be established with today's prediction capabilities. There are still shortcomings in both, the nomination of relevant parameters and their respective sensitivities. Although approaches are available for the sub-components, the definition of reasonable objective functions for an integrated stage-seal optimization is challenging. To give an example; a stator, which is optimized for minimum loss production [18] , may produce instabilities in the seal, which then lead to a net decrease, when evaluating the entire stage. First, it is essential, that the optimizer is generally capable to predict the formation of the instabilities and second, to derive adequate objectives for the overall optimization process. With the argumentation given so far, the first point can only be satisfied with numerically and experimentally cost-intensive investigations, the second will only be effective when the phenomenological interrelationship in the mechanisms is clear.

With respect to the increasing capabilities of algorithms, which are based on Machine Learning (ML) [19] , the evolution of promising purge flow systems could also be greatly automated. Again, the tremendous effort to generate appropriate data for training is problematic.

To sum up, the detection of the large-scale non-harmonic fluctuations, caused by purged stator-rotor cavities, has increased the demand for detailed and integrated stage-seal investigations. As valid for the entire HGP, it is the demand for solving a combination of aerodynamic *and* thermal issues, when evaluating promising technical solutions. Strategies, capable of simultaneously addressing detailed heat transfer phenomena [20] and full annulus unsteady turbine stage aerodynamics, are more the exception than the rule in publicly available literature. Well established methods are ready to use for the participating subsystems, though. On the one hand, full circle unsteady predictions [21] of multiple stages are successfully integrated into optimization procedures, yet still limited for a validation of selected variants . On the other hand, the knowledge base of heat transfer phenomena with increasingly complex aero-thermal boundaries is continuously growing. In the context of progressive rim seal designs, one key step now is seen in the development of the practical combination of existing strategies.

The present work aims to supplement to the phenomenological understanding of the

[18] the optimizer is searching for a stator passage geometry resulting in e.g. minimum overall pressure loss or a specific distribution of the secondary kinetic energy in the exit flow

[19] self-learning optimization approaches, in general the potential application of Artificial Inteligence (AI) in turbo-machinery R&D, is perfectly suitable to many sub-disciplines and the implementation of appropriate approaches into the design strategy is addressed by industrial and academic developers

[20] in the present case this is the rotor endwall heat load

[21] and well selected experimental representatives

spatio-temporal characteristic of rim seal purge flow, with a focus to their impact on the rotor hub side endwall aero-thermal load. A second emphasis is to document a data evaluation strategy, as developed for the efficient processing of the spatio-temporal results.

1.4.1 State of the Art

Note: This section is a revised version, as published in Ostrowski and Schiffer [51].
The hub side endwall region of the first high pressure rotor has always been of critical importance for the design of safe and reliable high pressure turbine sections. The blade root is simultaneously stressed by high centrifugal forces and thermal loads. Due to the rotation and the interaction with stationary flow structures, the rotor passage flow by nature is dominated by periodic fluctuations. In the hub side region, this transient but basically periodic character is superposed by the interaction with the rim seal purge flow, an important share of the high pressure secondary air system. It is intended to prohibit the ingestion of hot main flow into the inner cavities and wheel-spaces.
Besides the negative effect on the thermal cycle efficiency, the interaction between main and purge flow locally produces losses, finally lowering the efficiency of the stage or the individual blade row. Therefore, an optimization of the rim seal configuration is of high interest to the turbine designer. The final character of the seal flow is a combination of the internal and external boundary conditions on both, the stationary and rotating frame of reference. The spatio temporal flow patterns in the vicinity of the seal are three dimensional and highly transient. To further investigate the complex mechanisms, researchers have built up rotating test facilities accompanied by transient three-dimensional (3D) computational models. Due to restrictions in transient measurement techniques, as well as limited computational capacity, many setups historically were strong simplifications of the real turbine.
Within the last two decades, purge flow investigations then became more sophisticated in terms of their spatio-temporal resolution. Among other findings, they lead to the discovery of large scale rotating structures in the rim seal. They were found to be unrelated to the blade passing and disc frequencies. An early study, where such comparably low frequencies in the rim seal of an axial test turbine are identified, is the combined experimental and numerical study, conducted by Cao et al. [10]. Both, unsteady wall pressure measurements in the cavity and the computaion, show pressure fluctuations, which are rotating slightly below the rotor speed. Similar detections of large scale rotating cavity structures are presented in Jakoby et al. [39], Boudet et al. [7] and Julien et al. [42]. All of those studies highlight the importance to carefully choose the circumferential sector size to enable the structures to be generated in unsteady computational setups.
For the integrated design and optimization of turbine stages, unsteady multi-sector computations however were all but state of the art in that time. With increasing computing capacity, unsteady 360° setups became possible to a wider variety of applications.

However, detailed features, such as rim seal cavities, were often part of a mandatory idealization, then not fully accounted for in computations. A similar development can be observed in the field of experimental setups. Unsteady measurement techniques continuously found their applications in rotating test facilities. Those, however, had often a focus on either the main flow path or the cavity and wheel spaces.

Nevertheless, the trend is towards fully integrated investigations accounting for realistic external and internal boundary conditions of the purge flow. In doing so, the improvements are forced from both sides of the aforementioned segmented environments. Rotating disc spaces are supplemented by the external flow guiding geometries, first of all the vanes and blades. Sangan et al. [57] is referenced exemplarily for a whole series of experimental investigations conducted at University of Bath. The experimental facility was continuously developed over the years. A good overview can be found in the review of Scobie et al. [61]. The basic findings, regarding the different mechanisms of ingress, mainly the differentiation between external and internal induced ingress, were continuously refined. More recently, combined experimental and numerical studies with a focus on the unsteady ingress mechanisms were conducted, see Horwood et al. [31], Hualca et al. [32] and Roy et al. [56].

The other way around, rotating test turbine investigations were expanded to allow the consideration of more realistic and well instrumented rim seals. The focus is on an extended understanding of the interaction between main and seal flow, including the aero-thermal effect to the adjacent passage. A numerical study on a generic high-pressure turbine stage is the work by Chilla et al. [12]. Besides the detailed investigation of the spatio-temporal distribution of the purge flow, its effect on the adiabatic wall temperature distribution on the rotor hub side endwall is investigated. A non-axisymmetric redesign of the seal geometry was subsequently presented in Chilla et al. [13]. Camci et al. [9] have also recently published a combined experimental and numerical study identifying cavity modes in an axial turbine research facility.

To experimentally determine possible large scale modes in the cavity of the Oxford Rotor Facility, Beard et al. [6] present a modified and instrumented version of the rig, where an array of radially and circumferentially distributed unsteady wall pressure transducers are installed. In this work, a procedure for the detailed quantification of the lobe system inside the cavity is presented. Findings were confirmed and extended in the numerical studies presented in Gao et al. [22] and Palermo et al. [52]. In their review, Chew et al. [11] have summarized the wide field of research activities and findings in the field of rim seal investigations.

While focusing on the influence of rim seal purge flow to the secondary flow patterns in the rotor passage, the extensive experimental study of Schüpbach et al. [60] is another early evidence of rotor unrelated frequencies, as found in the rim seal region of axial turbines. Frequency analysis of the fast response aerodynamic probe data showed characteristic elevations at around half the blade passing frequency, when focusing to the hub region. Jenny et al. [40] presented a detailed investigation of the purge flow effect to the radial migration and unsteadiness of the rotor hub passage vortex.

The rig was then modified to allow a more precise quantification of hub cavity modes. Schädler et al. [59] could provide clear evidence of a strong interaction of rotating cavity structures to the purge flow characteristic. They conclude, that the large scale rotating structures need to be considered in the design process of next generation sealing features. In Schädler et al. [59] a study on a non-axisymmetric Purge Control Feature (PCF) is presented. The work of Iranidokht et al. [37] presents a detailed analysis on how geometry and operating conditions can influence the nature of cavity modes. A dense array of wall mounted, unsteady pressure transducers is installed to a two-stage test turbine. A detailed view on the amplitudes of the cavity modes again highlights the possibility, that cavity modes may dominate the transient rotor passage flow, when looking to the hub side endwall region. Iranidokht et al. [38] further investigated their impact on the stage performance.

The literature, as referenced so far, is focusing on the aerodynamic understanding of the purge flow mechanisms. As introduced in the beginning, the thermal loads in the blade root region are of critical interest for the high pressure turbine. Experimental heat transfer investigations in rotating passages however are complex. To enable a distinct investigation of the effect of purge flow to thermal quantities, a high resolution of the thermal quantities is desirable. The experimental approach of Lazzi Gazzini et al. [48] marks one solution to quantify simultaneously the heat transfer coefficient and the adiabatic wall temperatures in rotating test environments. In Lazzi Gazzini et al. [47] the method is then first applied to experimentally investigate the purge flow effect to the rotor endwall heat transfer. The method is adopted by Hänni et al. [25] to a contoured rotor endwall. The authors are able to characterize the heat transfer patterns and found good agreement to steady state predictions.

1.5 Thesis aims

The aim of this thesis is to contribute to the understanding of the spatio-temporal characterization of rim seal purge flow. Aero-thermal measurement techniques are applied to the purge flow region of the Large Scale Turbine Rig (LSTR), a large scale low-Mach turbine test facility operated by the Institute of Gas Turbines and Aerospace Propulsion (GLR). Large-scale rotating flow structures are detected and quantified with unsteady pressure sensors inside the cavity as well as in the stator-rotor interface. An unsteady, three-dimensional numerical model of the test turbine is derived, discretized and solved for, using the commercially available Computational Fluid Dynamics (CFD) package ANSYS-CFX.

In combining the experimental and numerical results, it is shown, that the influence of the cavity structures may have an immense impact on the rim seal purge flow characteristic. Results are in accordance with similar investigations from the previous two decades and serve as another proof to act with caution, when designing a rim seal region with stationary or oversimplified setups, on both, the numerical and experimental side.

As conclusions are drawn on both, the predicted and experimentally determined results, robust and valid data processing methods are essential for assuring equivalence when interpreting reduced or deviated quantities of a mechanism, which highly depends on time and space. Compared to the number of experimentally investigated geometrical and operational variations, as embedded in the wider research framework, the conducted unsteady computations are limited to a single stage-seal geometry. However, for this configuration, results are available for three different purge flow mass fractions. For this reason, all possible conclusions, as drawn in the scope of this work, are limited to the variation of this single operational parameter.

1.6 Research Framework

Methods, investigations and results presentation, as given in this thesis, can mainly be separated into two consecutive periods. First, and by far the greater portion of the physical and financial resources, focused on the design and realization of the experimental aero-thermal investigations. The instrumentation and data acquisition in the rotating frame of reference of the LSTR, as essential for the endwall heat transfer measurements, required a major rebuilt of the rotor assembly group. This work package was embedded into the framework of the AG Turbo, a public-private network of universities, research centers and globally relevant turbo-industry, based or operating in Germany. The actual project is titled COOREFLEX-turbo [22] 3.1.2, *Aerothermal Combustor Turbine Interaction: Rotor Platform* [23], grant number 03ET7071O, had a funding period 08/2015 to 12/2019 and was half financed by industry. The project definition and proposal was prepared together with Alstom, but General Electric acquired Alstoms power and grid businesses November 2, 2015. As a consequence, the communication to the industrial partner had some critical discontinuities regarding the exchange of geometries and the alignment of objective targets in general. Furthermore, accompanying computations, as originally projected by the industrial partner, were finally canceled. However, the major and most challenging deliverable, namely the determination of spatially highly resolved heat transfer quantities on the rotating endwall, was fulfilled within the scope of the project. To sum up, it is hard to believe that the metrological advancements, as achieved at the LSTR within the last decade, would have been possible without the AG Turbo. For a wider placement of the project work, synergies with other projects and a summary of the achievements are published in the final report Ostrowski and Schiffer [49] (German).

Experimentally determined heat transfer quantities on the rotating endwall of a purged test turbine stage may show unique features. However, they are of little value without a detailed understanding of the aerodynamic boundaries. This fact is closely coupled

[22] The COOREFLEX-turbo joint project itself was embedded into the 6th German energy research program funded by the Ministry for Economic Affairs and Energy.

[23] official German Title: Aerothermische Interaktion zwischen Brennkammer und Turbine: Rotorplattform

to the scientific motivation, see Section 1.3. When the project started, steady state flow field measurements in planes up- and downstream of the rotor, were well established at the rig. Concerning the investigation of rotor-relative flow quantities, most hardware was introduced in the era of COOREFLEX, where competences were subdivided between the 3.1.1 [24] and 3.1.2 projects. Hot wire probes and unsteady casing pressure measurements were established in 3.1.1, whereas unsteady pressure probes and fast response pressure transducers in the rim seal are affiliated with the 3.1.2. The strategy of subdivision turned out to be advantageous for the outcome of the present work, as the detection, characterization and interpretation of the rotating rim seal fluctuations are mainly based on unsteady pressure information.
As mentioned before, computations were not explicitly anchored in the project proposal for 3.1.2. With the first evidence of the existence of the rotating large scale cavity structures, their contribution to the near wall flow field was hard to be interpreted without having access to time-resolved three dimensional computational results. Despite the progress of the experimental research project itself, a computational representation was seen to be inevitable for a scientifically sound interpretation. Fortunately, the institute had access to the Lichtenberg high-performance computers. Together with the pre-existing numerical experience of the GLR on running numerically costly flow simulations on the super-computer, the way was open to apply for some computing time on the Lichtenberg. The fact, that the LSTR had been subject of a number of numerical studies before, was beneficial. The focus on the unsteady rim seal phenomena however still required some general extensions, which were mainly motivated to save numerical elements in the stator [25], which then allowed a larger portion of the internal rim seal cavity to be added to the model. However, even more important was the basic necessity to enable the formation of realistic rotating large scale patterns at all.
As valid for the prediction of most rotating non-harmonious instabilities in turbo machinery, the ultimate answer would have been an entire representation of the annulus. In the present case, the computing time for a 360° setup would have been computationally to expensive. A tradeoff finally led to a 60° sector model.
Having access to the unsteady compuational results, the foundation for the second main work package was available. The validation strategy mainly focused on the qualitative character of spatio-temporal structures in the rim seal region. As the unsteady predictions showed good consistency, their utilization for a detailed assessment of the aero-thermal impact of large scale rotating rim seal structures was valued applicable, opening the unique possibility to merge the aero-thermal experimental study with its numerical counter part. Finally, it is worth to highlight, that the unmistakable charm of this work was the implicit consideration of the tempo-spatial characterization of the turbine aerodynamics adjoined by the question of its thermal impact.

[24] Similar subject but with a focus on the aero-thermal phenomena in the blade tip region, official German title: Brennkammer-Turbine-Interaktion: Kühleffektivität und Aerodynamik im Blattspitzenbereich
[25] the stage, as installed and investigated in the LSTR is equipped with a whole bunch of cooling features on the vane and its endwalls. However, all cooling flows were switched off for the present study

2 Fundamentals

2.1 Cycle Performance and Turbine Cooling

As introduced in Section 1.2, the thermodynamic principal of the ideal gas turbine is represented by the air-standard reversible JBC. From now on, this configuration is denoted as the Reversible Uncooled Cycle (RU), for which the thermal cycle efficiency is a function of the overall pressure ratio only. Applying the corresponding isentropic temperature ratio $\tau = \pi^{(\gamma-1)/\gamma}$, the efficiency is given by $(\eta_{\mathrm{th}})_{\mathrm{RU}} = 1 - (1/\tau)$, where in addition to Eq. (1.1), RU is introduced as subscript to allow a clear distinction to the cycle variations, as being discussed in the following.
For the RU, the maximum temperature is the determining factor for the corresponding specific work, which is given by $(\bar{w}_{out})_{\mathrm{RU}} = (\theta/\tau - 1)(\tau - 1)$. These two relations can actually not be simpler, and at the same time, better representatives for one of the core issues in gas turbine R&D. Their derivation can be taken from any textbook on the subject of technical thermodynamics or gas turbine theory, and the indication of a specific resource is seen to be dispensable.
Complexity however increases quickly, when lowering the level of idealization. In doing so, there is a wide variety of frameworks available on this topic, then often termed as *Real Cycle Analysis* or *Model Based Performance Analysis*. Approaches strongly vary in complexity and, specifically, in how the integrated sub-components are represented. The different approaches are commonly integrated into a performance prediction tool and, independently of their individual origin, commercial or academic, the software packages have significant meaning for the actual gas turbine development engineer. With reference to Kurzke and Halliwell [44],

> A performance prediction program generally synthesizes the overall engine performance from the performance of its compressors, turbines, burners, nozzles, ducts, secondary air system and other elements.

The performance prediction is basically built up top to bottom, representing the main gas path in a one-dimensional manner. The individual components are represented by *black boxes*, and each engine manufacturer has their own libraries of component models.
Citing the introductory comments in (Gülen [23], Section 3.3), the term "“real"” in gas turbine performance predictions is brought back down to earth:

> Multiple side streams of cooling air, exiting the main flow path and then reentering it, make matters even worse. As such, no reference is made to a "“real"” Brayton cycle in this book. The "“reality"” resides in the actual hardware.

To bear in mind, this statement is from a textbook, in which the author impressively presents the application of cycle analysis and well-arranged incorporated formulations

of the first and second law of thermodynamics to predict the performance of real gas turbines. At the end, he still does not leave out the term *Real Cycle Analysis*, and with reference to Chapter 8, the consequences not only from irreversibilities and real gas properties is highlighted, but also the "“real"' effect of turbine cooling on the cycle itself. The presented framework enables an integrated consideration of cooling flows, leading the derivation of the corresponding overall cycle efficiency and specific work. Global cooling effectiveness and technology parameters are necessary to be either estimated in advance or by calibration. In general, the method is based on the assumption, that each individual cooling flow has either the potential to contribute to the work extraction in the stage, or it does not. The advantage of such a clear distinction of chargeable and non-chargeable cooling flow fractions is obvious and the implementation into powerful modeling tools can lead to impressively accurate performance predictions.

As true for most one-dimensional representations of highly complex systems, the challenge lies in the correct approximation of the implemented parameters. Moreover, the less parameters are involved in the model, its sensitivity to the individual one is often increased. For the consideration of cooling in a global parametric cycle analysis, the development of an appropriate toolbox is a key towards meaningful overall results, still with sufficient room for interpretation and optimization.

In the following, the attention is gradually turned away from the objective of a global Real Cycle Analysis. The issues, coming along with the parametric characterization of a cooled turbine section, are introduced incrementally. However, the implicit meaning of turbine cooling to the overall thermodynamic cycle will remain relevant. To conclude, it is the derivation of few but relevant parameters, required to adequately characterize the effect of turbine cooling [1]. In accordance to the real machine, coupling of turbine cooling to the main flow path is realized by an appropriate Secondary Air System (SAS) model. In such, the individual cooling flow fractions are represented by a set of parametrized components. Due to its interconnecting character, the setup of the SAS model may significantly influence the main components. For more specific information on the practical implementation of SAS in performance prediction tools, the reader is again referred to Kurzke and Halliwell [44]. An interesting modeling approach, targeting a systematic off-design optimization by modulation of the SAS, is presented in the dissertation of Woelki [68].

To summarize, the design of an efficient, safe and reliable SAS is a challenging engineering task by its own. It is mentioned again, that the purge and cooling flows, as used to cool the HPT, are only a sub-portion of the overall SAS. Its significance to the entire gas turbine design strategy is once more highlighted. Cooling air is not suddenly apparent at the turbine interface. It should be much more considered as something precious and its origin can be considered two-sided; first, there is the engineering with its interdepartmental and intrinsic character. Second, the origination can be considered from a thermodynamical view. Taking this picture, the nature of a specific

[1] in the discussion given so far, the term cooling incorporates the so called secondary cooling flows and thus the rim seal purge flow

cooling flow is somehow integrated into a closed cycle of delivery and consumption. It is the second method of approach, what is the focus of the upcoming discussion.

2.1.1 The Air Standard Cycle with Cooling

This section targets to introduce to a framework for the consideration of cooling flows, incorporated into a parametrized model of a turbine section. As stated in the general discussion on performance predictions, the ultimate goal is to correctly implement a cooled turbine into the one-dimensional representation of the entire machine. The complex interaction of cooling and secondary air with the main flow should be implicated into the corresponding section of the expansion path.
The grade of detail is chosen to be representative enough for the investigations, as presented in this thesis, but not more. Likewise to the investigated test setup, it is not necessary to account for any real gas effects. As a consequence, all working fluids are represented by the same perfect gas, having a common value for the specific heat, independent of temperature and pressure and the heat addition is represented by a simple heater. The subsequently presented approach is mainly based on Horlock [29]. Some more general information on the assumptions as well as the nomenclature, are taken from Horlock [30].
It is the beauty of the so called "'air standard"' cycle, allowing the formulation of a very compact set of expressions to consider cooling in a gas turbine. The generality of the framework will later allow the adaptation to the purge flow situation, as investigated in this work.
At this point, the reader could question the sense of presenting a global approach, while the focus of this work is mainly on the phenomenological understanding of a mechanism, which is primarily local or even point-wise. It is the large quantity of theoretical studies, which is available on the subject of turbine cooling implementation into cycle calculations. Due to the relatively small share of purge flows, when compared to those related to the overall cooling demand of the main path, they are often treated rudimentary.

Reversible Cooled Cycle (RC)

To begin with, Fig. 2.1a shows the T-s chart for the simple case of a reversible and closed air-standard cycle with single step cooling. In this configuration, an externally heated mass flow is mixed with extra compressor delivery air before entering the expansion process. It is the most simple thermodynamic representative of cooling the first stage stator only. The cooling air mass flow ψ is defined as a fraction of the main flow at turbine inlet [2]. Both flows are virtually separated after the compression, the

[2] choosing the turbine inlet mass flow as the reference in the definition of the cooling fraction ($\psi = m_C/m_3$) is used throughout this work. Where possible, formulations are normalized by the turbine inlet mass flow, as it is done in the analytical considerations of this section.

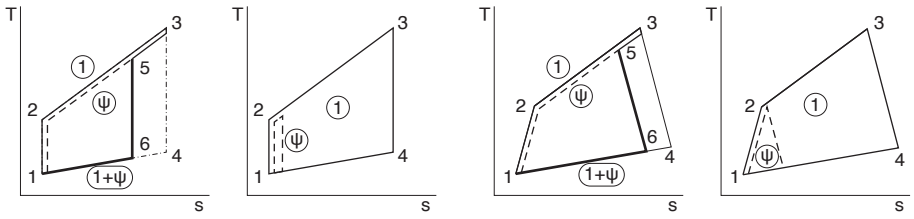

(a) Reversible cycle with cooling **(b)** Irreversible cycle with cooling

Figure 2.1: T-s diagrams for the one-dimensional consideration of cooling flows for the cycle performance definition

ψ is then bypassing the heater. Mixing of the pressurized, cold fraction and the hot unit mass flow then takes place at constant pressure $p_5 = p_3 = p_2$ before entering the turbine. The temperature of this new thermodynamic state 5 is known from the steady state energy equation

$$(1 + \psi)T_5 = T_3 + \psi T_2 \tag{2.1}$$

With this new turbine inlet temperature, the specific work of the expansion can be calculated straight forward as $w_\mathrm{t} = (1 + \psi)c_\mathrm{p}T_5[1 - (1/\tau)]$.
The corresponding compressor work is given as $w_\mathrm{c} = (1+\psi)c_\mathrm{p}T_1(\tau - 1)]$ and together with the heat added to the unit mass flow, $q_{23} = c_\mathrm{p}(T_3 - T_2)$, the thermal efficiency of the RC is given as

$$(\eta_\mathrm{th})_\mathrm{RC} = \frac{w_\mathrm{t} - w_\mathrm{c}}{q_{23}} = \frac{[(\theta'/\tau) - 1](\tau - 1)}{[(\theta' - 1) - (\tau - 1)]} \tag{2.2}$$

where the new temperature ratio $\theta' = T_5/T_1$ is taking the actual cooling mass fraction into account. Surprisingly, the expression can be simplified ending up to be the same as for the air standard uncooled cycle RU, which was introduced to be also independent from the temperature level at state 3

$$(\eta_\mathrm{th})_\mathrm{RC} = 1 - (1/\tau) \rightarrow (\eta_\mathrm{th})_\mathrm{RC} = (\eta_\mathrm{th})_\mathrm{RU} \tag{2.3}$$

This very basic example highlights, that an ideal cooling of a first stator row will not effect the thermal cycle efficiency negatively. Following further the line of thought of the authors, the result is against expectation, as the mixing process in state 5 is per definition irreversible. The answer can be given on the basis of the second law of thermodynamics. Without going into detail, it can be shown that the additional irreversibility of the adiabatic constant pressure mixing is compensated by a lower irreversibility associated to the heat rejection, which takes place from state 6 to 1 for the cooled cycle, instead of 4 to 1.

The cycle efficiency is only one side of the coin. Similar to the uncooled ideal cycle, the specific work is indeed depending on the temperature, at which the expansion starts. As a consequence, the introduction of cooling will lower the specific work, if the maximum cycle temperature T_3 is unaltered. The cooling fraction ψ is still accounted for in the mixing temperature θ' and the normalized specific work of the cooled cycle can be equivalently written as

$$(\bar{w})_{\mathrm{RC}} = \frac{w_{\mathrm{RC}}}{c_{\mathrm{p}} T_1} = [(\theta'/\tau) - 1]\,(\tau - 1) \tag{2.4}$$

With the consideration of cooling in a reversible cycle, the basic justification for a highly cooled first vane is obvious. The thermal efficiency of the gas turbine is not per se decreased by cooling. Room is left for the positive effect of enabling a higher TET, which is possible with an efficient and locally restricted application of cooling. To remember, the mass averaged adiabatic mixing temperature T_5, as can be interpreted as the effective RIT, is decoupled from the temperature resistance of the stator by film cooling.
A hint on the limitations in cooling however is also obvious from the RU-cycle. For the cooled turbine, the relation between optimum TET for a given pressure ratio keeps valid. Equation (1.3) can be rewritten for a case, where the isentropic temperature ratio τ of the compressor is given. The simple expression $\theta'_{opt} = \tau^2$ can hardly better represent the fact, that less cooling will increase θ'.

Irreversible Uncooled Cycle (IU)

So far, the simplicity of the reversible cooled cycle was suitable for introducing the paradox, that ideal cooling has no influence to the thermal efficiency. The grade of idealization is now decreased stepwise, and the introduction of component efficiencies is necessary. Again, the step from the reversible air standard to its irreversible counterpart is covered in standard text books on turbo machinery. To keep the formulation manageable and again allow a clear view on the effect of cooling, the framework is continued to be taken from Horlock [29], where the isentropic efficiencies for compressor and turbine are defined η_{c} and η_{t}. Staying consistent with the nomenclature, the uncooled but now irreversible cycle is indicated as IU and equals the path 1-2-3-4-1 in Fig. 2.1b. The corresponding thermal efficiency can be written as:

$$(\eta_{\mathrm{th}})_{\mathrm{IU}} = \frac{(\alpha - \tau)(\tau - 1)}{\tau(\beta - \tau)} \tag{2.5}$$

where the isentropic efficiencies and the maximum temperature ratio are included in the definition of the two variables $\alpha = \eta_{\mathrm{c}}\eta_{\mathrm{t}}\theta$ and $\beta = 1 + \eta_{\mathrm{c}}(\theta - 1)$. Without giving any statement on the quantitative consequences of irreversibility in compression and expansion, the most important massage is the appended dependency on θ by itself.

Irreversible Cooled Cycle (IC)

In accordance to the reversible cycle, the consideration of a cooling fraction ψ is included. The pressure of a total rate of $(1+\psi)$ is raised in the compressor to reach state 2. It is again the same assumption of an adiabatic mixing of ψ at T_2 and unit mass flow at T_3 before entering the expansion, taking place again from T_5 to T_6.
It is obvious, that the necessary work for the compression of ψ cannot be fully recovered, as it was the case in the reversible cooling cycle. As sketched in the T-s-diagram to the right, the cycle can again be subdivided into two individual cycles. The first has unit mass flow and follows the path 1-2-3-4-1 from the uncooled cycle. The second cycle is representing ψ, taking the path 1-2-9-1. For this configuration, the referenced framework presents a degraded uncooled cycle efficiency:

$$(\eta_{\mathrm{th}})_{\mathrm{IC}} = (\eta_{\mathrm{th}})_{\mathrm{IU}} - \psi\epsilon\frac{\tau-1}{\beta-\tau} \tag{2.6}$$

where $\epsilon = [1-(\eta_{\mathrm{c}}\eta_{\mathrm{t}}/\tau)-\eta_{\mathrm{t}}+(\eta_{\mathrm{t}}/\tau)]$.
Equation (2.6) highlights the important fact, that for the cooled irreversible cycle, the efficiency will drop with an increased amount of cooling fraction. The second term is representing the efficiency deficit coming along with the cooling, and its formulation is well chosen. Obviously, the deficit vanishes for $\psi = 0$ or for $\eta_{\mathrm{c}} = \eta_{\mathrm{t}} = 1$.

2.1.2 Linking Cycle Performance and Cooled Turbine Expansion

The theory on the efficiency deficit of an irreversible cooled cycle holds only, when the isentropic efficiency of the expansion is unaffected by the introduction of cooling. This assumption however does not aline with the expectation. It is disregarding the fact, that the introduction of cooling to a turbine stage will usually come together with additional losses. For a more realistic cycle evaluation, this interdependency is however the key to success and the development of suitable models goes back to the 1950s, where a formal framework for cooled cycle analysis was first introduced by Rohsenow [55]. In difference to the basic principle, as presented so far, the approach is based on a continuously cooled turbine, where the effect of heat transfer between the main gas path and the cooled components is accounted for. The theory uses Reynolds' analogy to connect the heat transfer to the passage flow, which is characterized by loss coefficients. The fundamental difference, which comes along with any continuous cooling approach, is leaving the assumption of an adiabatic expansion.
Obviously, the expansion process is now a combination of both, heat transfer and losses, leading to the curious possibility of isentropic expansion [3]. Without going into detail, the benefit of an analytical framework for continuous cooling is its self-containment. However, the consideration of, for instance, individual cooling technologies, is hardly given. As a consequence, the practical use for the turbine designer is limited. In fact, a

[3] isentropic but not reversible adiabatic

self-contained analytical framework requires an explicit definition of the cooling flow distribution with respect to the expansion line.

With a view to the applicability in a performance prediction program, a sequential approach of individual cooling flows is more feasible to bridge between the very simple single step cooling and a continuous approach. A multi-step (but discrete) cooling will allow to distinguish between an individual cooling technology and the aero-thermal consequence for the respective component, to which it is applied. However, also with a sequential approach, the influence of cooling to the turbine efficiency will still call to approximate the relationship. At the end, it is the specific way of evaluating this correlation, which makes any approach of linking turbine cooling to the cycle-performance so comprehensive. When included into a cycle performance evaluation, great care must be taken to a clear and exact efficiency definition associated to a single cooled turbine section.

There are innumerable methods available to link cooling to turbine efficiency and cycle performance. Most approaches developed by academia are based on a strict and fundamental aero-thermal framework. They widely vary in the underlying assumptions, their complexity and applicability to the actual cooling technology. The benefit of being publicly available is often canceled out by the unknown accuracy and sensitivity, when applied to a real gas turbine. According to Kurzke and Halliwell [44], industrially relevant strategies are not less ambiguous and even the exact definition of a cooled turbine efficiency may vary from one manufacturer to another. It is mainly the definition of the actual control volume, the approximation of the state of cooling flow at the interfaces together with other specifications, which need to be fixed in internal technical regulations. It is therefore not surprising, that the calculation, especially the combination of secondary air flow properties with those of the primary flow, which are often supported by an extensive research program at most manufacturers, Kurzke and Halliwell [44].

The model of the irreversible and cooled air-standard cycle notably illustrates the general importance for a sound cycle performance prediction, when cooling is involved. The approach can be developed further for a multi-step cooling arrangement, in which infinitesimal amounts of air are abstracted at an infinite number of points along the compressor. As presented in Horlock [29], this allows the approximation of a continuously defined expansion line, which is fully described by a modified polytropic turbine efficiency. The derivation of the multi-step cooling however again is strongly constrained by the assumptions for the infinitesimal cooling flow fractions. The presented formulation ends up to be of the form of classical continuous cooling approaches, as presented by Rohsenow [55] or El-Masri [17], showing the same drawbacks, as discussed earlier.

The very basic theory behind the continuous cooling approach however holds for multi-step cooling. It is the general assumption, that any fractional cooling can be thought as an elementary thermodynamic process, made up a mixing process at constant pressure followed by an adiabatic expansion with an adjusted turbine isentropic efficiency. The

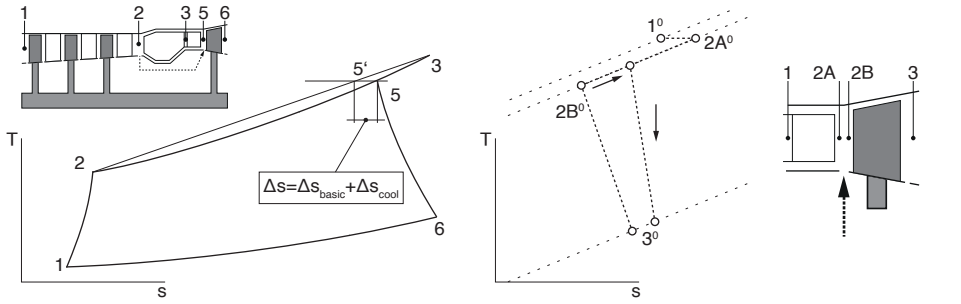

(a) Cycle representation with cooling **(b)** Stage representation with cooling

Figure 2.2: The connection between cycle and stage representation incorporating the mixing process between cooling and main flow

individual frameworks finally illustrate the derivation of combined polytropic turbine efficiencies, enabling the straight forward consideration of cooling into the overall cycle calculation.

The presented theory on addressing cooling to the thermodynamic cycle is based on the fundamental hypothesis of constant pressure mixing, without to scrutinize its validity. It is state 5 in the T-s diagram, as being retroactively responsible for the quality of the entire approximation of the expansion. With a bit of a distance to the analytical framework, the problem will now be on a meaningful and application oriented specification of state 5. The discussion on the applicability of single and multi-step cooling will be linked to the actual flow physics in a cooled high pressure turbine stage, as will be the focus of Section 2.2.

To summarize the overall cycle discussion, one final look though is given to an overall T-s-sketch of a gas turbine cycle with cooling. For better visualization and to simplify, the isobars were so far sketched as straight lines. In doing so, state 5, as being the result of the adiabatic mixing of main and secondary flow at constant pressure, was automatically positioned linearly between states 2 and 3, not violating the assumptions at all. For a closer look though, the isobaric heat addition of the main flow is now sketched, taking the exponential relationship between T and s into account. The target is to sensitize the reader for the fundamental meaning of entropy levels connected to the turbine expansion path.

On the basis of the second law of thermodynamics, mixing of two flows with different temperatures, will always come along with an increased entropy level. As illustrated in Fig. 2.2, the adiabatic mixing at constant pressure can be clearly depicted in a T-s diagram. The approach, as presented in the following, is based on Young and Wilcock [70], adapted to the air standard cycle from the previous section. The temperature of state 5 can be calculated straight forward using the first law of thermodynamics.

Together with the assumption of a common pressure for states 2 and 3, point 5 is known [4]. For the reversible cooled cycle, any losses associated to the ideal constant pressure mixing were *regained* by a lower heat rejection from 6 to 1 and there was no need for an exact loss quantification.
To guide towards a more accurate distinction of losses, the minimum entropy production due to mixing can be deviated with the second law of thermodynamics, while the temperature after mixing is still the result of the energy equation. The new state $5'$ is then given by

$$T_{5'} = (T_3 + \psi T_2)/(1 + \psi) \tag{2.7}$$

$$s_{5'} = (s_3 + \psi s_2)/(1 + \psi) \tag{2.8}$$

The entropy creation, namely the difference $s_5 - s_{5'}$, can be evaluated straight forward, however only for the present assumption of constant pressure mixing. Highlighting the fact, that thermal mixing is an unavoidable increase of entropy and by definition independent from other loss mechanisms coming along with the introduction of cooling, its exact consideration in the definition of cooled turbine efficiency will influence its final value. As will be discussed in more detail in the next section, it is the specification of the ideal expansion process, against which the actual work is rated in the sound definition of a turbine efficiency.
As depicted in the sketch, the *thermal mixing* represents only a portion of the entropy increase towards state 6. The quantification of the remaining entropy production, as being responsible for the increase from s_5 to s_6, is the main objective of any detailed cooling loss model. Undoubtedly, cooling will only be partially accountable and the *rest* will be present also in an imaginable uncooled expansion. As further introduced by Young and Wilcock [70], an appropriate framework should first of all address cooling separately for each blade row. In doing so, a combination of heat transfer theory and empirical data can be used to attribute losses to the respective aero-thermal phenomena. Such an additive treatment of entropy production can lead to a generic expression of the form

$$\Delta s = \Delta s_{basic} + \Delta s_{cool} \tag{2.9}$$

To finally guide over to a detailed discussion of turbine stage performance, influenced by cooling, a potential expansion process of a first high pressure turbine stage is exemplary brought into focus. So far, all cycle considerations were done without any differentiation between total and static states. When now turning towards the actual flow physics in a turbine stage, it is well known that a proper distinction gets mandatory. It is basically a detailed look to the upper right section of the overall T-s diagram, allowing now to distinguish between the individual thermodynamic states within a single stage.

[4] the expansion from 5 to 6 in the air standard cycle from Section 2.1.1 was only possible with an approximated isentropic efficiency representing the cooled turbine

The respective path in the T-s diagram, as depicted in the right sketch of Fig. 2.2, is representing a stage, where a cooling fraction is mixed with the main flow between the stator and rotor blade rows. This configuration, indeed still a gross simplification, is generally suitable to cover a rim seal purge flow. At this point, it is most important to notice, that the concept of constant pressure mixing can be applied to any specific intermediate step of an expansion line, as far as the supply pressure of the cooling is equal to the corresponding main flow pressure.

The main flow is entering the stage at state 3 and the loss production, associated to the stator, is exclusively caused by a total pressure loss, while maintaining the total temperature, as the process is assumed to be adiabatic. The mixing then leads to a reduction in total temperature and the state at the rotor inlet is fixed by the postulated constant pressure. The work, which is then extracted in the rotor, can again be treated adiabatic, incorporating the entropy production caused by the combination of the imaginary uncooled turbine. Losses are amplified by the terms associated to the extra portion of the cooling itself, however reduced by the aforementioned unavoidable *thermal mixing*.

2.2 Turbine Stage Performance and Cooling

The attention will now be turned from the cycle towards a single turbine stage. The thermodynamic state of the cooling flow, if needed, will therefore be decoupled from the cycle. Some general strategies on the description of a cooled turbine section were given in the previous section, though always with the potential to be integrated into cycle or performance calculations. That constraint however is now given up and the scope is expanded towards a more detailed consideration of the actual flow phenomena within the stage.

As true for many technically relevant aero-thermal processes, a whole range of tools and approaches are available to quantify the influence of cooling to the turbine performance. They range from one-dimensional (1D), continuous or stage by stage estimates of the necessary amount of cooling air towards 3D, multistage CFD setups. With reference to the previous section, the implementation into parametric cycle analysis however is limited for such higher order approaches. As shown in the cycle analysis, the aero-thermal boundary conditions of main and cooling flow in the turbine section are coupled to the compressor and combustor. A coupling of three dimensional computational predictions of compressor, turbine and the corresponding part of the SAS is limited by computing power and the application is debatable in general, as the choice of suitable interfaces will oftentimes allow similar conclusions.

Now, what is a possible approach to overcome the discrepancy between the need for overall cycle performance predictions on one side and, on the other, the missing knowledge about how the turbine section will react on changes in the cooling strategy? As mentioned before, the industry has in-house developed tools for turbine performance predictions, often developed and calibrated over years. They can include both,

empirically determined correlations and models, which are based on the actual flow physics. Based on mass and energy balances, they provide the approximation of representative thermodynamic states in front and after each individual blade row. Applying the point-wise addition of the cooling flows, the expansion lines with work extraction can then be treated similarly to an uncooled equivalent with an individually adjusted turbine efficiency. It is highlighted, that an uncooled turbine has the outstanding advantage of being adiabatic. All point-wise approaches however require an explicit allocation of the cooling flow addition. With respect to a stage, the actual allocation implicates the very important fact of the cooling flow to have the potential to do work or not.
In Gülen [23] and other American literature on that topic, the terms *chargeable* and *non-chargeable* are commonly used for a clear distinction between these two . All non-chargeable flows are added upstream of the rotor blade row. They all participate in the expansion. In reverse, chargeable cooling is added downstream of the respective rotor to then allow the definition of the thermodynamic inlet to the next stage.
There is no doubt that cooling flows ejected in the first stator should be judged as non-chargeable [5]. They are accelerated when mixed with the stator main flow.
A more complex question is how to treat rotor and disc cooling flows. A common argumentation to group them to be chargeable arises from their lack of momentum. Their nature is often assigned to be parasitic. For the rotor blade cooling, this sounds reasonable, as already the circumferential acceleration on their way towards the blade, consumes shaft power instead of adding any positive share. As some of the rotor cooling is injected in the leading edge region, their angular momentum is partially retrieved. On how to best consider disc cooling and purge flow, opinions differ. For pre-design studies, their influence on the turbine expansion path is often neglected. The concept of choice is then again an energetic mixing downstream of the rotor, which is necessary to fulfill the mass and energy balances.

2.2.1 The Uncooled Axial Turbine Stage

The basic working principal of an uncooled stage is presented on the example of an axial flow turbine stage. This approach comes together with some important simplifications, but is the most suitable to introduce to the most important parameters as well as the nomenclature, as will be used from now on in this work. Concerning a clear notation, there are unfortunately several standards used throughout the international turbine community, all with their own justification and mostly with a historical background.
For the characterization of a stage, their is at first the labeling of the general positions and the notation of the velocities and their components. While it is common practice to distinguish the three main stations by numbering, their order is not generalized. Basic statements on turbo machinery theory called for consistency, independent of

[5] Exceptions can make sense! Due to a lack of momentum, the platform cooling within the stator passage is often assigned to be chargeable.

the considered component. This leads to the first of the two widely used standard numberings, where always the work extraction takes place between station 1 and 2. For a turbine, where the stator is being located upstream of the rotor, this means a numbering of 0-1-2. The zero however can easily create confusion with respect to a clear definition of thermodynamic quantities, where the total state is often indicated by a super- or sub-scripted zero. [6] With this background, the second standard numbering is chosen. For the turbine stage, the stator inlet is then indicated with 1. The stator outflow and the rotor inlet are not distinguished and both are labeled with 2, followed by state 3 representing the state at rotor outlet.

The notation of the velocities and its components is as follows. The absolute velocity is c, its rotor relative counterpart is v and the blade row velocity is u. In fluid dynamics, velocity is mostly meaningless without the definition of a direction. For turbo-machinery, the direction is appropriately defined in a cylindrical coordinate system with components in the axial, radial and circumferential direction. A cylindrical vector field can be clearly visualized, analyzed and processed in meridional and cascade sections, where the annular channel is cut in an axial-radial direction or it is virtually unfolded into the axial-circumferential direction. The local velocity vector is therefore fully described with its axial, circumferential and radial component and again, there are various nomenclatures found in the literature. Throughout this work, the three components will be indicated by the subscripts r, ϕ and z and for radial, circumferential and axial, respectively.

It is necessary, to introduce the definition of the flow angles in the absolute and rotor relative frame of reference. In this work, all angles are referenced to the corresponding axial component. The sign of the angle is fixed by the orientation of the circumferential velocity, which follows the right-hand rule. Radial velocities and the corresponding angles are introduced later, as being irrelevant in the mean diameter treatment.

The velocity triangles at the rotor interfaces, 2 and 3, as sketched in Fig. 2.3a, are the simple result of a Galilean transformation between the stationary and rotating coordinate system. For a cylinder coordinate system, solely the circumferential component is adjusted to the effective rotary speed, leading to the interrelation of absolute and relative velocities to the blade speed

$$\vec{c} = \vec{v} + \vec{u} \quad \text{or} \quad \begin{pmatrix} c_\mathrm{r} \\ c_\phi \\ c_\mathrm{z} \end{pmatrix} = \begin{pmatrix} v_\mathrm{r} \\ v_\phi \\ v_\mathrm{z} \end{pmatrix} + \begin{pmatrix} 0 \\ \Omega r \\ 0 \end{pmatrix} \tag{2.10}$$

with magnitudes being determined as

$$|\vec{c}| = c = \sqrt{c_\mathrm{r}^2 + c_\phi^2 + c_\mathrm{z}^2} \quad |\vec{v}| = v = \sqrt{v_\mathrm{r}^2 + v_\phi^2 + v_\mathrm{z}^2} \quad |\vec{u}| = u = \Omega r \tag{2.11}$$

[6] total states are also widely referred as the stagnation value because of its physical interpretation, and the three most important quantities are total temperature, total pressure and total enthalpy

and the absolute and relative circumferential flow angles, α and β, respectively, as

$$\alpha = \arctan(c_\phi / c_z) \quad \beta = \arctan(v_\phi / v_z) \tag{2.12}$$

With reference to Fig. 2.3a, the general principal of an axial turbine is briefly presented on the basis of the simple mean diameter treatment. Further, the flow velocities are assumed to be circumferentially homogeneous or virtually represented by a well chosen circumferential average. The theory, as presented in the following, is covered in every textbook on turbo-machinery. For the preparation of the following introduction, various literature was used and the reader is referenced to the appropriate chapters, as indicated in the footnote [7].
At the inlet of the stage, state 1, high energetic flow is available to be converted into shaft power. Recalling again Section 2.1.2 , for the first stage of a HPT, this equals the combustor outlet [8]. Due to the absence of any motion, no work extraction is possible in the stator row, which is then of preparatory character. Its basic role is to turn and accelerate the flow towards the circumferential direction. At state 2, the flow will still have the same total energetic state, but now with a higher share of kinetic energy with reduced static pressure. In this condition, the flow is now suitable to be turned a second time, now in the opposite direction. It is the simple fact, that this deflection is now taking place in a rotating blade row, enabling the extraction of mechanical energy. At the rotor exit, the energetic state of the fluid will be lowered exactly by that portion. Keeping in mind the one-dimensionality of the fluid properties, this very simple principle can be quantified on the basis of fewest elementary physical relations. The simplest form to connect the change of the fluid quantity to the shaft power is possible by applying the conservation of angular momentum and conservation of energy. By holding the constant radius assumption valid, it can be shown, that the specific work output can be determined by simply multiplying the blade speed u with the difference of the circumferential absolute velocity between rotor outlet 3 and inlet 2

$$P = \mathrm{T}\Omega = \Omega m(c_{3\phi} r_3 - c_{2\phi} r_2) \rightarrow w = u(c_{3\phi} - c_{2\phi}) \tag{2.13}$$

The equation is fundamental and universal for turbo machinery and also known as Euler's turbine equation. The relation is, for instance, suitable for a pre-design approximation of the maximum possible power output of a single stage, taking rules of thumb for the stage turning magnitude and the cross section of the annulus. Furthermore, Euler's turbine equation incorporates the very basic interrelationship between radius and angular speed, with which most fundamental design strategies in turbo machinery can be easily interpreted. However, the equation yields neither any information on the flow phenomena causing the turning, nor does it incorporate the stator row at all. Finally, it is based on a change of kinetic energy only, and the thermodynamic state of the flow is virtually excluded.

[7] Saravanamuttoo et al. [58] - chap. 7, Bräunling [8] - chap. 8, Rick [54] - chap. 2 and Traupel [65] -

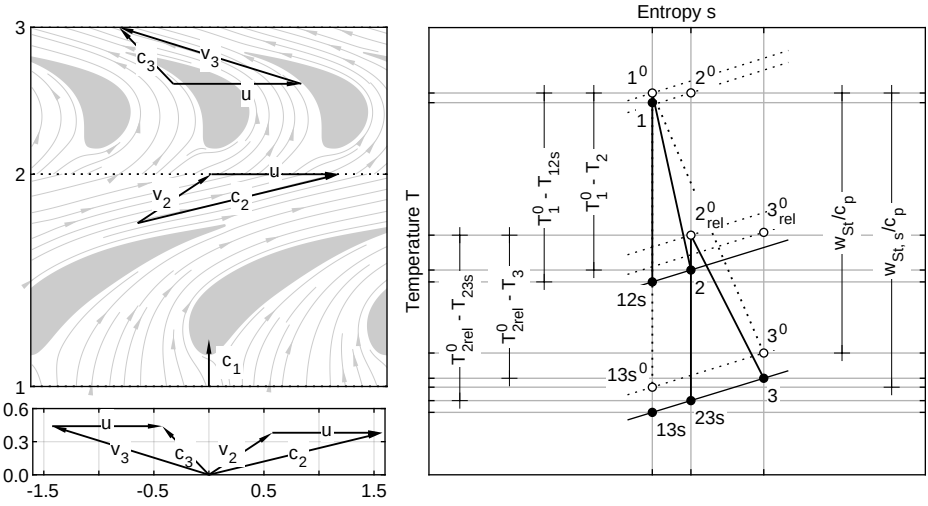

(a) Velocity triangles **(b)** T-s diagram

Figure 2.3: One-dimensional representation of an uncooled turbine stage

To incorporate both, the entire stage and the respective thermodynamic states, the steady flow energy equation is applicable to the depicted axial flow turbine. That approach is then much more driven by the conservation of energy, as provided by the respective subarea of technical thermodynamics. As will be shown in the following, the steady state energy equation can be supplemented by the second law of thermodynamics, to not only quantify the losses separately in the individual blade row, but also to incorporate potential heat transfer to the stage.

To begin with, the turbine specific work output will now be expressed on the basis of the steady flow energy equation, balancing one dimensionally from state 1 to state 3. As the turbine stage is first assumed to be uncooled and adiabatic, no heat transfer takes place and the specific work can directly be calculated as

$$w_{\mathrm{St}} = h_3 - h_1 + \frac{c_3^2 - c_1^2}{2} = h_3^0 - h_1^0 = c_{\mathrm{p}}(T_3^0 - T_1^0) \tag{2.14}$$

With the assumed adiabatic process in the stator, the corresponding total temperature difference from 1 to 2 is zero leading to $T_2^0 = T_1^0$. Thus, also the deviation of the turbine work from the steady state energy equation is possible by considering the rotor

chap. 5

[8] in the cycle performance demonstration, Section 2.1 this is equal to state 3, in the international state nomenclature for aero-engines, this is state 4

blade row only. To evaluate the goodness of the energy conversion in the stage however, also losses in the stator need to be accounted for. The very general concept of efficiency is to compare the output of a process to a well defined optimum. For a turbo machinery component, it is common to take a representative isentropic process as a reference. For the uncooled turbine stage, this is simply the adiabatic and nondissipative expansion. Thermodynamically, this is simply the work of an isentropic expansion between a representative pressure difference. Most commonly, this is the available total pressure difference, leading to the well known expression for the *total-to-total* isentropic turbine stage efficiency

$$\eta_{\mathrm{St,s}} = \frac{w_{\mathrm{St}}}{w_{\mathrm{St,s}}} = \frac{h_3^0 - h_1^0}{h_{13\mathrm{s}}^0 - h_1^0} = \frac{T_3^0 - T_1^0}{T_{13\mathrm{s}}^0 - T_1^0} = \frac{\Delta T_{\mathrm{St}}^0}{\Delta T_{\mathrm{St,s}}^0} \tag{2.15}$$

To visualize the thermodynamic paths in the stage, the process is depicted in the T-s diagram in Fig. 2.3b. As gets clear from the chart, it is the value $(T_3^0 - T_{13\mathrm{s}}^0)$ incorporating the full rate of dissipation, which occurs in the stage.
Concerning this difference, it is the precise understanding and the search for its minimization, depicting a central target of the long lasting engineering work done in the field of turbine R&D. Innumerable early studies on cascades were conducted to build up a precise picture of what is actually *happening* inside the blade rows. A standardized framework on the categorization of turbine stages is available. Such an approach allows an effective comparison of differently scaled and operated components and, as common in natural science [9], non-dimensional groups of parameters are best suited to reduce the number of problem participating variables.
For the investigation of turbine stages, there are three main parameters, that are widely used by turbine designers. The first one is a non-dimensional representative of the stage work and correspondingly often termed as the work coefficient. It is more common, to take the half of the squared blade speed $u^2/2$ as reference, while also u^2 or $2u^2$ is used in literature. The first one corresponds to the specific kinetic energy of the blade and has therefore a proper physical interpretation in terms of energy. Divided by the specific heat capacity, the expression can also be interpreted as a normalized total temperature drop over the stage, then normalized with the dynamic portion of the total temperature with respect to the blade, and it is then denoted as the temperature drop coefficient Ψ

$$\Psi = \frac{h_3^0 - h_1^0}{u^2/2} = \frac{2c_{\mathrm{p}}\Delta T_{\mathrm{St}}^0}{u^2} \tag{2.16}$$

In a gas turbine stage, acceleration usually takes place in both stator and rotor blade rows. It is common to take the static enthalpy difference in the rotor and relate it to a reference enthalpy difference of the entire stage. The parameter is termed as the degree of reaction Λ and again, there are different definitions regarding the reference.

[9] technical thermodynamics and flow mechanics are considered to be included

Some definitions use the total stage enthalpy difference, where others refer to the static one. Furthermore, it is arguable, if one should take the actual or isentropic values at the stage exit. Throughout this work, the degree of reaction is based on the true, non-isentropic values and the total enthalpy difference is taken as the reference. This is advantageous, as the parameter can now be derived only on thermodynamic states up- and down stream of the rotor

$$\Lambda = \frac{h_3 - h_2}{h_3^0 - h_2^0} = \frac{\Delta T_\mathrm{R}}{\Delta T_\mathrm{R}^0} \tag{2.17}$$

The energetic treatment of the axial turbine stage, as presented so far, can be assumed to be fully one dimensional and the interconnection between thermodynamic state and flow field was possible with the velocity magnitudes only. Apparently, the thermodynamic states in the stage need to be linked somehow to the basic geometry of the blades. Again, the following approach is widely available in textbooks and will only be briefly summarized.
It is the decomposition of the respective velocity vectors enabling an explicit connection of the geometry to both, the temperature drop coefficient Ψ and the stage reaction Λ. Assuming an unchanged axial velocity at all three states ($c_{\mathrm{z}1} = c_{\mathrm{z}2} = c_{\mathrm{z}3} = c_\mathrm{z}$) and representing the vane and blade geometry in terms of angles between the axial and circumferential component, the Euler turbine equation, Eq. (2.13), can be rewritten incorporating the actual flow angles up- and downstream of the rotor

$$w_\mathrm{St} = u c_\mathrm{z}(\tan\alpha_2 + \tan\alpha_3) = u c_\mathrm{z}(\tan\beta_2 + \tan\beta_3) \tag{2.18}$$

With the flow coefficient being defined as the ratio of axial flow and blade velocity, $\Phi = c_\mathrm{z}/u$, the temperature drop coefficient and the stage reaction can be rearranged to give

$$\Psi = 2\Phi(\tan\beta_2 + \tan\beta_3) \quad \text{and} \quad \Lambda = \frac{\Phi}{2}(\tan\beta_3 - \tan\beta_2) \tag{2.19}$$

The isentropic stage efficiency, as defined in Eq. (2.15), incorporates the losses for the overall stage. It does not yet allow to distinguish between the stator and rotor row. For a detailed stage investigation, losses can be defined for each of the rows separately and the target is to deviate the shares of the respective entropy production.
The definition of losses in a blade row are formulated in a wide variety and in literature, there is not the one definition available. However, they are always a meaningful evaluation of the difference between an ideal and real process, now over an individual row.
As sketched in the T-s diagram in Fig. 2.3b, the entropy first increases within the stator from s_1 to s_2 to be followed by a further increase within the rotor to s_3. Aerodynamically, both processes correspond to an acceleration [10] and they can simply be represented by

[10] this is true for all practically realized axial gas turbine stages, where stage reaction is commonly somewhere in the range of 0.5, in any case not 0 nor 1

a flow through two subsequent diverging nozzles, both with friction. The approach to quantify the goodness of an acceleration device one-dimensionally is simply to oppose the true gain in velocity to the one theoretically possible in the absence of friction. With another look to the T-s diagram, the comparison can be based on pressure, enthalpy or entropy [11].

In contrary to many textbooks, it is not the pressure based loss coefficient, which will be highlighted first, but an enthalpy/entropy based formulation. This is motivated by their suitability for the formulation of the non-adiabatic stage, as will be of interest in the further course of this work.

The detrimental increase in enthalpy, which is ascribed to friction in the stator row, is given by the difference $h_2 - h_{12s}$ and the increase in the rotor is $h_3 - h_{23s}$. With a similar approach, as presented for the entire stage, the definition of a blade row efficiency is possible. There are two formulations used commonly, differing only in taking either the total or static enthalpy as the inlet condition, as presented by Young and Horlock [69]. Beginning with the static enthalpy as reference, the so called static-to-static efficiency can be defined individually for both, the stator and rotor row as

$$\text{Stator: } \eta_{\mathrm{S}_{SS}} = \frac{T_1 - T_2}{T_1 - T_{12s}} \qquad \text{Rotor: } \eta_{\mathrm{R}_{SS}} = \frac{T_2 - T_3}{T_2 - T_{23s}} \tag{2.20}$$

Taking the total inlet state as the reference, the expressions will slightly change to the total-to-static blade row efficiencies

$$\text{Stator: } \eta_{\mathrm{S}_{TS}} = \frac{T_1^0 - T_2}{T_1^0 - T_{12s}} \qquad \text{Rotor: } \eta_{\mathrm{R}_{TS}} = \frac{T_{2\mathrm{rel}}^0 - T_3}{T_{2\mathrm{rel}}^0 - T_{23s}} \tag{2.21}$$

In these efficiency formulations, the enthalpy increase by friction is not available by direct reading. However, it can be easily converted on the basis of another well known expression for the performance rating of a blade row. It is termed as the enthalpy loss coefficient, in which the enthalpy increase is normalized with the ideally achievable kinetic energy at the exit

$$\text{Stator: } \zeta_{\mathrm{S}} = \frac{T_2 - T_{12s}}{T_1^0 - T_{12s}} \qquad \text{Rotor: } \zeta_{\mathrm{R}} = \frac{T_3 - T_{23s}}{T_{2\mathrm{rel}}^0 - T_{23s}} \tag{2.22}$$

Choosing the isentropic achievable kinetic energy at the inlet as reference, the total-to-total efficiency and the respective enthalpy loss coefficient are related straight forward as $\eta_{\mathrm{S}_{TS}} = 1 - \zeta_{\mathrm{S}}$ and $\eta_{\mathrm{R}_{TS}} = 1 - \zeta_{\mathrm{R}}$. In difference to the blade row enthalpy loss coefficients, as presented above, it is also common to take the true exit kinetic energy as a reference, leading to expressions of the form $\eta = \Delta h/(c^2/2)$, see Denton [15] and Saravanamuttoo et al. [58]. The motivation might lay in the similarity to the stagnation

[11] choosing an entropy based process as the frictionless optimum is not meaningful, as the respective entropy difference will be always zero

pressure loss coefficient, which is defined as the total pressure loss normalized with the dynamic head at the respective exit plane

$$\text{Stator: } Y_{\mathrm{S}} = \frac{p_1^0 - p_2^0}{p_2^0 - p_2} \quad \text{Rotor: } Y_{\mathrm{R}} = \frac{p_{2\mathrm{rel}}^0 - p_{3\mathrm{rel}}^0}{p_{3\mathrm{rel}}^0 - p_3} \tag{2.23}$$

As Denton [15] emphasizes in the beginning of his work on the general nature of loss mechanisms in turbo-machines

> The reason, that this definition of loss coefficient (here Eq. (2.23)) is so common is that it is easy to calculate it from cascade test data and not because it is the most convenient to use in design.

So far, all formulations were defined for stator and rotor synonymously. Thereby, all total quantities were implicitly referenced in the corresponding frame of reference; stationary for the vane versus rotating for the blade. The equivalence however is only given, when the assumption of zero work keeps valid while doing the transformation into the rotating frame of reference. Considering the entire passage flow of an axial turbine rotor, the assumption is generally violated, when there is any wall segment in a relative movement to the virtually stationary system. For shroud-less rotor blades, as commonly used in modern high pressure turbine designs, the entire casing does such a virtual movement resulting in a certain amount of kinetic energy possibly imposed by friction.

In detailed loss investigations, especially when focused on the tip region, the constant total enthalpy assumption can lead to misinterpretations. Depending on the exact interaction within the passage, the introduced energy can either increase dissipation leading to a comparable level of acceleration or it can even lead to an apparent benefit in relative magnitude of the exit velocity. The work of the stage, and thus the isentropic stage efficiency, will always reflect the global performance, which is based on the total states in the stationary system. To recap, neither of the efficiencies or loss coefficients, as given for the rotor, are suitable for a reasonable consideration of a potential change in the total enthalpy from inlet to exit of a rotating blade row. Choosing the isentropic process as the reference, as done in the formulations so far, at least the potential change in the total enthalpy is not part of the reference process.

As the previous discussion on a meaningful loss quantification has shown to be not always uncoupled of the respective frame of reference, the question is how to best get rid of any possible interdependency. The best variable, and this is again the idea of many detailed loss investigations in turbo-machinery, is to focus on the rate of entropy production itself. It is the natural behavior of entropy, that its local value is independent of whether it is viewed in a rotating or stationary blade row. Taking the definition of entropy for a perfect gas, the actual value can be evaluated straight forward from the local temperature and pressure, either taking both quantities as total or static values

$$s - s_{\mathrm{ref}} = c_{\mathrm{p}} \ln(T/T_{\mathrm{ref}}) - R \ln(p/p_{\mathrm{ref}}) \tag{2.24}$$

It is this distinct expression, with which every of the individually induced entropy increments can be coupled to the respective enthalpy or pressure losses. Equation (2.24) is the integrated form of the *fundamental thermodynamic relation*, see e.g. Stephan et al. [64], expressed in terms of enthalpy. For a perfect gas, this leads to

$$T\mathrm{d}s = c_\mathrm{p}\mathrm{d}T - v\mathrm{d}p \tag{2.25}$$

For a process with a small portion of temperature increase due to friction, compared to the overall temperature difference, Eq. (2.25) can be approximated by discretization. For the stator row, the rise in temperature, as resulting from the dissipation within the blade row, can then be simply expressed by

$$T_2 - T_{12s} \approx \frac{T_2}{c_\mathrm{p}}(s_2 - s_1) \tag{2.26}$$

As obvious from that expression, it is the local linearization of an isobaric process, with the slope being the local temperature [12]. The relationship may now be employed for the definition of an entropy loss coefficient. The approach is similar to the introduced enthalpy loss coefficients, and for stator and rotor this leads to

$$\text{Stator: } \zeta_{\mathrm{S,s}} = \frac{(T_\mathrm{S}/c_\mathrm{p})(\Delta s_\mathrm{S})}{T_1^0 - T_{12s}} \qquad \text{Rotor: } \zeta_{\mathrm{R,s}} = \frac{(T_\mathrm{R}/c_\mathrm{p})(\Delta s_\mathrm{R})}{T_{2\mathrm{rel}}^0 - T_{23s}} \tag{2.27}$$

It is now time, to come back to a formulation of a stage efficiency. With the framework and assumptions presented so far, the isentropic efficiency in Eq. (2.15) can be rewritten in terms of the individual entropy increases of the two adjacent blade rows. In contrast to the efficiency formulation based on the total temperatures, they can be split back into the static temperature and the respective dynamic portion. With the assumption of constant specific heat capacity, the relation between total and static temperature will always be $T^0 = T + c^2/(2c_\mathrm{p})$ and the total temperature difference over the stage is

$$\frac{w_\mathrm{St}}{c_\mathrm{p}} = T_3^0 - T_1^0 = T_3 + \frac{c_3^2}{2c_\mathrm{p}} - T_1 - \frac{c_1^2}{2c_\mathrm{p}} \tag{2.28}$$

The total temperature difference of the corresponding isentropic expansion is increased by $(T_3^0 - T_{13\mathrm{s}}^0)$, which is equivalent to the corresponding static temperature difference $(T_3 - T_{13\mathrm{s}})$, as the kinetic portion c_3^2/c_p does not change. This is, with reference to the T-s-diagram in Fig. 2.3b, the sum of $(T_3 - T_{23s})$ and $(T_{23s} - T_{13\mathrm{s}})$. The first summand is equivalently defined by the rotor enthalpy loss coefficient, see Eq. (2.27). To quantify the second expression, the stator loss coefficient cannot be taken directly, as this one is based on the stator exit pressure level. Now, the entropy loss coefficient, as defined in Eq. (2.27), can be the *missing link*, as it is advantageously defined on the basis of entropy. The induced losses can virtually be scaled to the respective pressure

[12] in a T-s diagram, the slope is the local temperature normalized by the specific heat capacity, so T/c_p

level by applying an appropriate temperature as the local *slope*. There are two possible approximations of the entropy created in the stator, namely

$$(s_2 - s_1) \approx \frac{c_\mathrm{p}}{T_2}(T_2 - T_{12s}) \quad \text{and} \quad (s_2 - s_1) \approx \frac{c_\mathrm{p}}{T_3}(T_{23s} - T_{13\mathrm{s}}) \tag{2.29}$$

Equating the two entropy differences, the stator loss can be scaled to the rotor exit pressure, where it is then applicable for the quantification of the stage efficiency. The total temperature increase induced by dissipation within the entire stage is then

$$(T_3 - T_{13\mathrm{s}}) = (T_3 - T_{23s}) + \frac{T_3}{T_2}(T_2 - T_{12s}) \tag{2.30}$$

which is the all-dominant part of the isentropic stage efficiency. The fact, that the stator losses are scaled with the temperature ratio (T_3/T_2) is taking the so called reheat factor into account. It states, that losses created at high temperatures will have a minor negative effect on the overall isentropic efficiency. For the investigated stage, that effect has a negligible effect, as the temperature and pressure ratios are low. This circumstance also motivates the focus on isentropic efficiencies only, leaving out any considerations of polytropic efficiencies. For detailed stage investigations however, the strategy of quantifying the loss subdivision should make use of the factorized loss quantification.

2.2.2 The Cooled Axial Turbine Stage

The development of approaches for the evaluation of cooled turbine stages goes back to the 1950s, where formulations were based on robust and analytical thermodynamics. In that time, meaningful frameworks were available for the calculation of steady one-dimensional gas flows. Equations were framed for many technically relevant situations. They can still be seen as the basis for the potential brake down of complex flow configurations. To just name two known relevant examples, there is the compressible flow through a constantly heated pipe and the adiabatic, but friction involving channel flow. An early, but still often referenced textbook is the magnum opus by Shapiro [62], which contains the full span of technical relevant principles of fluid dynamics and thermodynamics, both in a theoretical and applicable formulation.

Review of Continuously Cooled Turbine Models

In the context of such kind of analytical investigation and the application to a cooled gas turbine, the work of Hawthorne [27] is taken as an example. The presented model of a cooled turbine is fully one-dimensional and allows the quantification of heat rejection, separately in the stator and rotor, combining friction respectively loss coefficients to their effect on the heat transfer. It finally allows the investigation of cooling and is applied to various types of axial turbines. Where the stator and rotor passages are

represented by conical tubes, the basic interrelationship of heat transfer and friction is presented in a closed analytical formulation, where the exact gas properties are calculated on the aero-thermal interaction at the fluid solid interface. In the definition of the cooled turbine efficiency, the ideal work is always assumed to be the outcome of an adiabatic and reversible expansion, which seems to be advantages for consistency but ignores any potential use of the heat extracted. In Part 2, Hawthorne [28] develops the continuous cooling approach for multistage turbines, where the reduction in the reheat potential is shown to have a significant effect on the overall turbine efficiency. Hawthorne's model is applied to cycle calculation in Rohsenow [55], where the very distinct influence of the cooling-loss factor was shown to have a considerable negative effect on the performance of cooled turbines. The intuitive certainty, that the reduction of stage efficiency induced by cooling can cancel out the positive effect of higher cycle temperatures, is highlighted in the study.

Hawthorne's work is an excellent source for a possible, closed and analytically based method to expand uncooled stage theory, as presented in the previous section, by cooling. The work however is limited to heat transfer only, while the injection of a cooling mass flow into the referenced control volume is not covered. The main principal of enabling heat to be transferred within a turbine expansion line, even without any injection and mixing, is though of great value also for a practical oriented treatment of turbine cooling and several considerations in Hawthorne [27] are certainly universal and timelessly important.

Almost 30 years after Hawthorne has presented his closed formulation to account for continuous heat rejection in a turbine, El-Masri [18] published his model of the expansion in cooled turbines, now with cooling flow ejection. He presents closed-form solutions for three cooling technologies, two representing air cooled technologies, and the third describing internally water-cooled expansion. They all have in common, that the work extraction is modeled as a continuous process rather than occurring in discrete, consecutive stages. For all three cooled expansions, functions are consistently established to describe the relative heat to work loading. The formulation is then evaluated with the first law of thermodynamics and integrated over the control volume, which is virtually nothing more then the temperature range, in which cooling is applied. As a result, the local mass fraction and the corresponding work extracted, can be quantified.

Besides the characteristic of the extractable work over temperature, the framework further allows the evaluation of the pressure-temperature relation, which is the corresponding T-s line of the expansion. To do so, the locally generated entropy needs to be approximated. Entropy is assumed to be additive and the shares are either cooling related or unrelated. It is this second law based balancing over an individual control volume, making it so applicable to a whole range of approaches. The balance equation for an element is

$$ms + dms_{\mathrm{C}} + dS_{\mathrm{gen}} = (m + dm)(s + ds) \tag{2.31}$$

with dS_{gen} being the total amount of generated entropy within the control volume. El-

Masri now accounts for three different mechanisms allowing the formation of entropy. First, there is $dS_{\mathrm{gen},fric}$ due to friction and aerodynamic losses, which is unrelated to cooling and somehow a source of loss. Second, there is the potential loss by throttling the cooling air from its supply pressure p_{C} to the local main flow pressure. The third part, $dS_{\mathrm{gen},mix}$, finally combines the irreversibility connected to the heat transfer from main flow to cooling, heat transfer bringing the mixture to a common temperature and a loss in stagnation pressure induced by the acceleration of the coolant to the main flow velocity. It is this last fraction generating the highest uncertainties, when cooling induced losses are predicted. In the case of El-Masri's model, for all three entropy generation mechanisms, relatively simple analytical approaches are chosen to allow the integration. To do so, the cooling related loss terms are all expressed in terms of the local mass fraction, which is known from the energy based balance from the first part. The calculated T-s characteristic is one outcome of the formulation, the second though allows a quantified analysis of the respective shares of entropy production. The exact theory on the loss terms and references to accompanying studies are given in the publication or will be presented in this work, when necessary.
As another well-known approach for a continuous expansion line including cooling, the respective section in Traupel [65], a widespread German classic textbook on turbomachinery, is briefly introduced. It is based on a linear approach to describe the fraction of cooling air injected within the turbine section. Losses are then accounted for in a reduced polytropic efficiency. The local reduction is depending on the respective ratio of mass fraction to pressure ratio $d\mu/d\pi$, where the normalized cooling fraction μ will begin to participate on the work extraction in the moment of injection. The reduced polytropic efficiency for the stage is defined as

$$\eta_{pr} = \eta_p - K\pi\frac{d\mu}{d\pi} \tag{2.32}$$

Traupel then formulates a closed solution for an ideal polytropic efficiency, which represents a process, where first an ideal mixing of the full amount of cooling is followed by an expansion to the turbine exit temperature, extracting the same amount of work as the initial continuous mixing has allowed. The important statement on that approach is, that every cooled turbine can be thermodynamically represented with by a reduced efficiency, in which the mixing first takes place in an ideal process. If such an overall representation of a cooled stage is appropriate, strongly depends on the purpose of investigation.
As often true for closed, analytical and steady solutions of technically complex flow situations, approaches with continuous injection have their specific field of application. Depending on the parametrization, models can lead to distinct conclusions on global characteristics, such as sensitivities or maximization procedures. Looking at the three introduced models (Hawthorne [27], El-Masri [18], Traupel [65]), the formulation of the problem is always set up for answering the two most important questions. First, how is the specific work reduction related to the amount of cooling, when the turbine

is operated within the same pressure ratio and second, if an elevation of maximum gas temperature is possible at all.

Segmented Modeling of a Cooled Turbine Stage

The concept, which will be used in this work, first of all needs to allow for the point-wise injection of cooling air. A strategy for a continuous injection of cooling flow within the passage however is not necessary. As highlighted above, it is far from being unusual to consider continuous or multi-step cooling as virtually being point-wise. Reasons for such simplifications were discussed in Section 2.1, where the coupling between cooling and cycle is highlighted.
This section is thought to be a counterpart to the previous one, where the theory of an uncooled axial stage was introduced. Losses were separately accounted for the stator and rotor, defined in terms of entropy with Δs_{S} and Δs_{R}, respectively. It was shown, that the dissipation in the stator can be scaled to a respective increase in total temperature at the stage outlet temperature level, compare Equation 2.30.
With a similar strategy, the consideration of cooling can be rearranged. First, the stage is considered as a whole, now with two inlets, the turbine inflow at state 1 and the cooling at state C. They both exit the stage at state 3. To allow a proper thermodynamic description of the individual and mixed states, in contrast to the uncooled stage [13] , it is now relevant to account for the respective mass flows, where necessary. Where Eq. (2.14) rates the power of the uncooled stage per unit mass flow, the actual power is now enlarged by the expansion of an individual cooling flow.

$$P_{\mathrm{St}} = m_1 c_{\mathrm{p}}(T_3^0 - T_1^0) + m_{\mathrm{C}} c_{\mathrm{p}}(T_3^0 - T_{\mathrm{C}}^0) \tag{2.33}$$

$$\widetilde{P}_{\mathrm{St}} = \frac{P_{\mathrm{St}}}{c_{\mathrm{p}} m_1} = (T_3^0 - T_1^0) + \psi(T_3^0 - T_{\mathrm{C}}^0) \tag{2.34}$$

Following the argumentation in Young and Horlock [69], it is the variety of definitions available to define the ideal process, making the cooled stage efficiency so miscellaneous. The first popular approach is to ideally expand the main and cooling flows separately, each from its individual inlet total state to the total exit pressure. Taking this approach, the result is commonly termed after Hartsel [26], with the ideal power defined as

$$P_{\mathrm{St,s,H}} = m_1 c_{\mathrm{p}}(T_{13\mathrm{s}}^0 - T_1^0) + m_{\mathrm{C}} c_{\mathrm{p}}(T_{\mathrm{C3s}}^0 - T_{\mathrm{C}}^0) \tag{2.35}$$

$$\widetilde{P}_{\mathrm{St,s,H}} = \frac{P_{\mathrm{St,s,H}}}{c_{\mathrm{p}} m_1} = (T_{13\mathrm{s}}^0 - T_1^0) + \psi(T_{\mathrm{C3s}}^0 - T_{\mathrm{C}}^0) \tag{2.36}$$

As shown by Young and Horlock [69], an efficiency formulation based on that ideal process can exceed unity, when different but ideal gas properties are assumed for

[13] all quantities could be considered as their specific value, as their was only one mass flow present throughout the stage

main and cooling. The authors therefore present efficiency definitions, in which an ideal mixing conceptually takes place prior to a collective expansion of both, main and cooling flows, which follows the same reasoning as was already highlighted in Section 2.1.2 for the definition of T_5 and $T_{5'}$. While the temperature is again rated by the steady-flow energy equation [14], it is the definition of the pressure after mixing, for which an appropriate model is sought for.

Thermodynamically, the mixing process is assumed to be adiabatic. The quantification of the pressure level after mixing is then proposed to be based on any of the three following assumptions; First, the pressure after mixing is set to be the inlet pressure of the main flow. The second assumes fully reversible mixing and the third specifies a limitation of entropy generation, accounting for the individual stagnation pressure levels of both, the main flow and cooling.

The framework, especially the two latter approaches, in which the stagnation pressure of the coolant flow is accounted for, is thermodynamically more consistent, compared to Hartsel's approach. It is based on the fact, that even an ideal mixing of two gases at different temperatures and pressures always comes along with an unavoidable entropy generation. This portion, first of all, has nothing to do with an increased aerodynamic loss, as they arise by flow perturbation connected to the cooling injection itself.

To introduce the concept, the entropy creation for the ideal mixing can be split into three fractions

$$\Delta s_{mix} = \Delta s_T + \Delta s_P + \cancel{\Delta s_C} \tag{2.37}$$

where the term Δs_C represents entropy creation due to compositional mixing. As discussed in the reference, the term can be neglected as compositional mixing, if present, will always occur in both, the real and ideal process. Furthermore, in the context of this work, the term is naturally zero, as gas and cooling have the same composition.

For the two remaining portions of entropy, the framework strictly follows second law formulations and the first term, Δs_T, is the entropy ascribed to the thermal equalization. Main and cooling flow change their entropy separately between their individual total inlet temperatures and the state after mixing, having the temperature T_{m}

$$\Delta s_T = \left(\frac{1}{1+\psi}\right) c_{\mathrm{p}} \ln \frac{T^0_{\mathrm{m}}}{T^0_1} + \left(\frac{\psi}{1+\psi}\right) c_{\mathrm{p}} \ln \frac{T^0_{\mathrm{m}}}{T^0_{\mathrm{C}}} \tag{2.38}$$

The second term, indicated as Δs_P, is the entropy created due to the pressure equalization in the adiabatic mixing.

$$\Delta s_P = \left(\frac{1}{1+\psi}\right) R \ln \frac{p^0_1}{p^0_{\mathrm{m}}} + \left(\frac{\psi}{1+\psi}\right) c_{\mathrm{p}} R \ln \frac{p^0_{\mathrm{C}}}{p^0_{\mathrm{m}}} \tag{2.39}$$

[14] simply adapting the indices Eq. (2.7) to the now valid nomenclature, the temperature after mixing is now defined by $(1+\psi)T^0_{\mathrm{m}} = T^0_1 + \psi T^0_{\mathrm{C}}$

Concerning the respective amount of unavoidable entropy creation, the first is fixed by a fully reversible adiabatic mixing process, termed as *Fully Reversible Mixed Efficiency* (FR). In this case, the total amount of entropy generation is set to zero. In doing so, the stagnation pressure is the result of setting $\Delta s_{mix} = 0$, which equals $\Delta s_P = -\Delta s_T$. Solving for the normalized stagnation pressure after mixing, this leads to

$$\frac{p^0_{\mathrm{FR}}}{p^0_1} = \exp\left(\frac{\Delta s_T}{R}\right)\left(\frac{p^0_{\mathrm{C}}}{p^0_1}\right)^{[\psi/(1+\psi)]} \tag{2.40}$$

In the second approach, by the authors termed as the *Weighted Pressure Mixed Efficiency* (WP), the ideal state after mixing is taking only the temperature equalization as unavoidable. The pressure term Eq. (2.39), can then be set to zero and the pressure after mixing is

$$\frac{p^0_{\mathrm{WP}}}{p^0_1} = \left(\frac{p^0_{\mathrm{C}}}{p^0_1}\right)^{[\psi/(1+\psi)]} \tag{2.41}$$

Similarly to the uncooled stage theory, also the cooled stage can be partitioned into the two adjacent rows. The effect of cooling can then be largely considered decoupled from blade rows located upstream of the location of injection. For a 1D investigation of rim seal purge flow, this is a predestined strategy. Even if the theory is most widely applied for the judgment of cooling within the HGP, it can be applied to a purge flow straight forward. It is the basic idea to distinguish unavoidable losses of the mixing process to those coming along with aerodynamic penalties, which could possibly be decreased by appropriate design strategies.
It is now the idea to particularize the presented approach to a purge flow situation, where the injection takes place conceptually point-wise at a location between stator and rotor. The next section is not only important to clarify the 1D thermodynamic representation of this specific situation of an axial turbine stage, but is also relevant to predefine the notation, as will be used in the upcoming chapters.

2.2.3 One-Dimensional Consideration of Rim Seal

Having introduced the basic thermodynamic principals for the general consideration of cooling in an axial turbine stage, it is now applied specifically to a purge flow, which is introduced upstream of the rotor blade row. With reference to the investigated configuration in the test turbine, the purge flow has, in contrast to any real machine, a higher temperature than the main flow. The approach however is applicable to an inverted temperature difference, as the enthalpy and entropy balances stay valid.
To allow the introduction to the basic approach, the stage is now extended by one additional state. With reference to Fig. 2.4, the stator rotor interface, in the uncooled case characterized by state 2, is now divided into two subsequent stations, where 2A is positioned right after the stator passage and 2B at the rotor inlet. The interface of rim seal and main annulus is now located in between these two positions. For the 1D

consideration, the exact geometry is irrelevant. However, the sketch in the figure is already based on the investigated geometry, enhancing the consistency with the two and three dimensional expansion, as will be given later.

As the one-dimensionality can generally be seen as point-wise representatives at the respective axial position, averaging can be virtually performed to be correct at mid-span. This situation is accounted for with the circles drawn into the sketch. For the investigated setup of the modeled turbine, the positions, as indicated, now allow the following distinctions to be made. Both blade rows can be treated adiabatically, being interrupted only point-wise between $2\mathrm{A}$ and $2\mathrm{B}$. This assumption is of fundamental importance, as the row efficiencies and loss coefficients, as defined in Section 2.2.1, can be adopted one to one. With this approach, the influence of the purge flow can be decoupled from losses inside the cavity. To assess the rotor blade row only, the balance equations are deployed simply between $2\mathrm{B}$ and 3, without any difficulty in the definition of the ideal process.

To account for the overall losses including mixing, the formulations from the previous section are still valid and applicable, now taking the efficiency definitions of the previous section. This can mean to investigate the entire stage, balancing the main flow from 1 to 3 and the seal flow from C to 3. Furthermore, a mixed approach is possible, where the stator row is now excluded. In doing so, the main flow is then balanced from $2\mathrm{A}$ to 3 and the purge from, equivalent to the entire stage, from C to 3.

The demonstration of the 1D stage theory with purge flow shows, that the exact underlying definition of efficiencies is crucial. The subdivision into the three sectors though allows the approach to be clearly formulated. This is not only true for the 1D consideration, as presented so far, but enables also losses to be clearly assigned in two-dimensional (2D) and 3D considerations.

2.3 Turbine Aerodynamics

The 1D treatment of the axial turbine stage is now stepwise extended, introducing the spatio-temporal character of the flow in axial turbine stages. The basic interrelation between the expansion characteristic and the turbine geometry, as given in Section 2.2.1, showed that the local share of total and static quantities can always be represented by the respective coordinates in a T-s diagram. No answer however was given to how the individual blade row geometries do introduce the deflection. Remembering the complex, multi-dimensional boundaries for a potential rim seal optimization, the relevant aero-thermal phenomena in the rotor passage has to be depicted in a detailed manner. This section will end up with an introduction to the spatio-temporal characteristic of the 3D flow field in the region of interest. To begin with, the flow field is first considered two-dimensional, where the choice of the temporal consideration is introduced

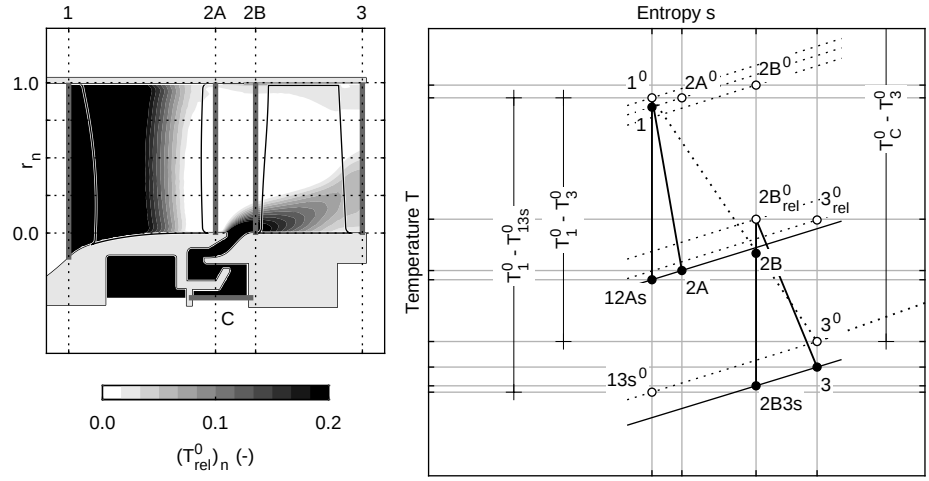

(a) Localization of thermodynamic states of the stage with purge flow

(b) T-s diagram for the stage with purge flow

Figure 2.4: One-dimensional representation of an axial turbine stage with rim seal purge flow injection between stator and rotor. The situation is equivalent to the investigated configuration, where the purge flow has a higher temperature than the main flow. The interface is now represented by three individual states $2\mathrm{A}$, $2\mathrm{B}$ and C. The circumferential view is complemented with the normalized total temperature difference $(T^0_{\mathrm{rel}})_{\mathrm{n}} = (T^0 - T^0_1)/(T^0_{\mathrm{C}} - T^0_1)$.

2.3.1 General Turbine Flow Field Consideration

The velocity triangles, as shown in Fig. 2.3a, were declared to be valid representatives of the flow situation at the respective axial location. As will be introduced now, approaching from the 1D stage theory to any higher order consideration is all but distinct. The working principal of an axial turbine, compare 2.2.1, is first given in a virtually unfolded axial-circumferential coordinate system, in which the flow vector is fully described by the two corresponding components, namely c_ϕ and c_{z}. The *simple mean diameter treatment* neither allowed the consideration of a circumferential distribution of the flow, nor does it account for any radial velocity component [15].
To expand the discussion towards the two missing spatial as well as the temporal dimension, the flow field from now on will be defined in a 3D Eulerian specification, where the unsteady flow field is described as a function of position and time. For the

[15] in fact, a distributed radial velocity is not excluded from the 1D consideration, they are solely zero as a consequence of the planar averaging approach to deduce a *good* 1D or point-wise representative of the annulus flow field

absolute velocity, this is stated as

$$\vec{c} = \vec{c}(\vec{x}, t) \quad \text{or} \quad c_i = c_i(x_j, t) \tag{2.42}$$

On the right hand side, the index notation is introduced. Any unsteadiness in the velocity field, despite of its frequency and magnitude, can be generally considered with the classical Reynolds decomposition, where the local and instantaneous flow vector is described by its arithmetic mean superposed by an unsteady, random part

$$c_i(x_j, t) = \overline{c}_i(x_j, t) + c_i'(x_j, t) \quad \text{with} \quad \overline{c}_i'(x_j, t) = 0 \tag{2.43}$$

The Reynolds averaging is the common approach for equating the time-average flow variables for incompressible flow. For a flow field with variable density or compressible but unsteady, it may be necessary to introduce a density-weighted averaging method, then termed as Favre averaging. As the flow field of the investigated low-Mach stage can be considered incompressible, the Reynolds averaging is assumed to be the valid temporal averaging method.
For a flow situation with fluctuating periodic boundary conditions however, the classical Reynolds decomposition can be expanded by a third term, which quantifies the periodic share. For a rotating blade row, the dominating frequency is obviously the Blade Passing Frequency (BPF). In such an environment, every single stator-rotor relative position can be thought of being an uncoupled configuration by itself, which is frequently repeated. The three dimensional, temporal mean of one specific relative position is then often termed as a phase-locked or ensemble averaged field [16].
To enable the investigation of the randomness with respect to one specific phase, the unsteady flow field is now expressed as a composition of the unrelated time-average flow field $\overline{c}_i(t)$, superimposed by the average and random part of the periodic fluctuation

$$c_i(t) = \overline{c}_i(t) + \tilde{c}_i(t + nT) + c_i(t) \tag{2.44}$$

in which the replications in the *sampling* are defined by the period T and the number repetitions n.
The time-average of the flow field $\overline{c}_i(t)$ is the same as in Eq. (2.43), being the result of a series of unrelated samples. To determine the periodic contribution, sampling can be simply thought to be phase-locked first and then averaged to give the total magnitude indicated as $\langle c_i \rangle$. The fluctuating component can than be separated by the difference of both averages as

$$\tilde{c}_i = \langle c_i \rangle - \overline{c}_i(t) \tag{2.45}$$

Comparing Eq. (2.43) and Eq. (2.44), it is obviously the random part of the classical Reynolds decomposition being separated by its periodic content.

[16] such a flow situations is sometimes also denoted as frozen rotor, where the relative position between stator and rotor are specified in terms of a phase locking angle or the respective time normalized by the period of the blade passing events

For the cylinder coordinate system, compare Section 2.2.1, the unsteady and three dimensional local flow vector, as generally formulated in Eq. (2.42), can be written as

$$\vec{c}(\mathrm{r},\phi,\mathrm{z},t) = c_\mathrm{r}(\mathrm{r},\phi,\mathrm{z},t)\vec{e}_\mathrm{r} + c_\phi(\mathrm{r},\phi,\mathrm{z},t)\vec{e}_\phi + c_\mathrm{z}(\mathrm{r},\phi,\mathrm{z},t)\vec{e}_\mathrm{z} \tag{2.46}$$

For both, a stator or rotor time-averaged flow field consideration, the purpose of investigation first should determine the proper temporal averaging method. It is indispensable to decide, if any interaction between the adjacent rows are of interest or, on the other hand, can be neglected. As obvious from Eq. (2.46), the two different temporal averaging methods can be superposed by spatial averaging in the direction of the three spatial coordinates, individually or in combination. The definition of the spatial coordinate system can then be chosen in accordance to the respective problem. A clear distinction between the different averaging methods is of fundamental importance for any observation in the stator-rotor interface. To introduce the different tempo-spatial averaging approaches, the unsteady CFD-results, as available for the investigated stage, are being taken and exemplarily processed and visualized. While the details on the CFD-setup are presented later in Section 3.2, some basics are briefly summarized here.
Results are sampled 360 times per revolution, equivalent to a 1° spatial resolution in the ϕ-direction. Processing is performed for two full revolutions. To considerably reduce memory requirements, flow variables, available on every grid point of the multi-million numerical mesh, are interpolated to a regular mesh with a circumferential resolution of 1440 per 360°, so one grid point every 0.25°. The corresponding ϕ resolution at mid-span is taken as reference for the step size in the r and z direction.

2D Flow Field Consideration - Unrelated Time-Average

With reference to Fig. 2.5 the influence of the frame of reference, or generally the coordinate system, to the unrelated time-average is presented. In accordance to Eq. (2.43), the arithmetic mean of the flow variables are taken to be the valid temporal averaging approach. To clearly indicate the stationary frame of reference, the r-ϕ_S-z coordinate system is introduced, in which the ϕ coordinate is now indexed with an S. The variable being visualized is the specific static entropy as given in Eq. (2.24), with T and p being the arithmetic mean, where all 720 available time steps are considered. Obviously, the circumferential periodicity is one stator pitch, independent of the axial position. As the rotor is continuously moving with time, the effect of the blades is blurred. However, the picture incorporates every possible unsteady influence of the rotor [17], as can be seen in the overlying streamlines. Such unrelated time-averaged results are perfectly suited to trace and assign stator flow structures, when they convect through a rotating blade row.

[17] definitely, the phrase *every* is relative, as only those structures are included, which are captured within the temporal resolution. Being aware of this limitation, the origin of the artifacts in the area of the rotor is given

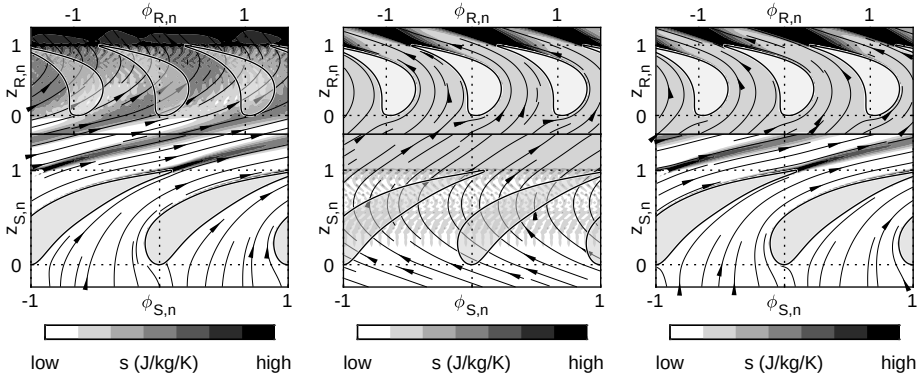

(a) Unrelated time-average in the stationary frame $\phi_{S,n}$

(b) Unrelated time-average in the rotating frame $\phi_{R,n}$

(c) Unrelated time-average mixed $\phi_{S,n}$ and $\phi_{R,n}$

Figure 2.5: Unrelated time-average of specific static entropy at mid-span: Unsteady flow quantities can be either entirely averaged in the stationary or rotating frame - another possibility is to choose the respective frame and depict results in one view.

It is meaningful to normalize ϕ_{S} with the dominating spatial periodicity of one stator pitch, which is indicated from now on with the additional index n. The origin is aligned to the stator leading edge at mid-span, raising from left to right in accordance to the right-hand-rule. To allocate the axial position of the blades, they are depicted though having no circumferential influence to the flow field.

In Fig. 2.5b, the time-average is performed in the rotor relative coordinate system. A corresponding circumferential coordinate is now defined to be rotating with the respective rotor angular speed given by $\phi_{\mathrm{R}} = \phi_{\mathrm{S}} + \Omega t$. In accordance to the stationary frame of reference, the angular coordinate is also normalized, now with the pitch of the rotor.

A major benefit of temporally resolved turbo-machinery data is the free choice of the frame of reference, irrelevant of the initial system. A clear assignment of a specific observation is then mostly possible with a check up in either of the frames. The tracking of the origin of flow structures, discovered in the stationary flow filed, can be meaningful to be done in the rotating frame. As depicted in Fig. 2.5c, an interface between the frames can be introduced in one single view. In the figure, it is positioned reasonably somewhere in between the two blade rows. Such a picture now enables the visualization of the averaged flow fields in the particular coordinate system. However, and this is most obvious from the plot, every circumferential continuity is being lost by the unrelated temporal averaging. Finally ,the analysis of such 2D results has limited value for the investigation of stator-rotor interaction mechanisms, as any

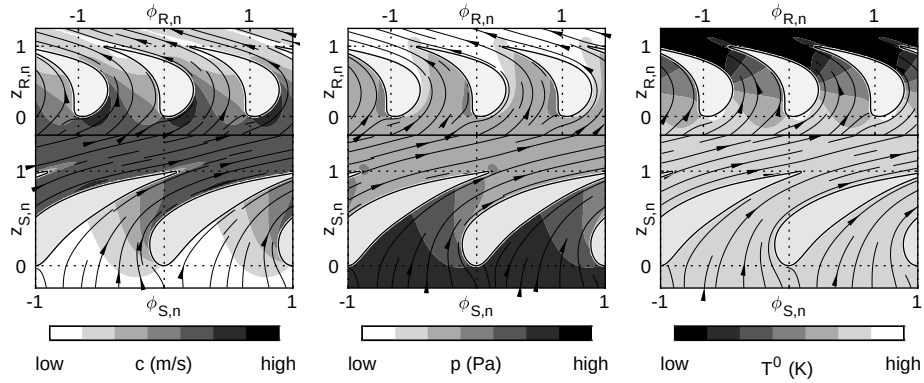

(a) Unrelated time-average of the velocity magnitude

(b) Unrelated time-average of the static pressure

(c) Unrelated time-average of the total temperature

Figure 2.6: Unrelated time-average of the flow field at mid-span: The circumferential coordinate is chosen with respect to the considered blade row.

circumferential flow field distribution is uncoupled from the adjacent blade row. The periodicity in ϕ, as highlighted before, will always follow the dominating flow guiding structures, which are virtually fixed in the respective frame.

Independently of the highlighted drawbacks coming along with the unrelated temporal averaging, fundamentals on the 2D stage aerodynamics are good to be introduced though. To begin with, Fig. 2.6 shows the time-averaged contours of absolute velocity, static pressure and total temperature, again at mid-span. Considering the stator flow field first, the objective is clearly visible. To enable the desired increase of c_ϕ, the flow accelerates within the stator passages. The higher the deflection, the more swirl can be delivered to the subsequent rotor. The characteristic of the acceleration is directly connected to the shape of the stator profile, which follows the basic shape of a nozzle [18]. The increase in absolute velocity, as visible in the contours, comes along with the continuous reduction in static pressure. The total temperature stays at a constant level, as the stator does not fulfill any movement.

Looking to the rotor flow field, a similar characteristic in static pressure decrease is observed. The share of the static pressure decrease between stator and rotor, as introduced with the degree of reaction Λ in Eq. (2.17), is reflected in the static pressure. Looking at the absolute value, the rotor decreases the velocity, where the de-swirl of the flow comes along with the work delivered by the moving blade rows.

The basic 2D flow field characteristic, as briefly introduced here, reflects the aero-

[18] the continuous decrease in cross-sectional area, as being the characteristic feature of a nozzle, is apparent when imagining the local area normal to the flow direction

dynamic design strategy of the stage. For the current work however, no further information on the exact stage geometry is seen to be required, the stage is taken as it is.

2D Flow Field Consideration - Phase-Locked Average

The CFD results at mid-span are now used to introduce to phase-locked time-average. A major benefit, in contrast to the unrelated approach, is the recovery of a circumferential consistency between the stationary and rotating coordinate systems. As introduced in Eq. (2.45), the phase locked averaging is, virtually thought, a continuously repeated investigation of one single flow configuration. Even if that situation incorporates high magnitudes of random and large scale fluctuations, the phase-locked average is supposed to be converged in any case, which is given by the superposition of the time-averaged flow field $\overline{c}_i(t)$ with a local phase locked share $\tilde{c}_i$.
It is now again the specific static entropy, which is regarded as most suitable to introduce to the effect of a variation in the phase-angle. As the investigated configuration is fully adiabatic, the magnitude in entropy is a pure image of the loss distribution, invariant of the coordinate system and the progress of the expansion path. This is reflected by the fact, that entropy is independent of being based on static or total quantities, as the process in between is per definition isentropic, see e.g. Denton [15].
The loss pattern shows a classical 2D characteristic in both blade rows. Compared to the endwall regions, the stator loss pattern is clearly arranged, when convected through the rotor passage and an introduction to the fundamentals of stator-rotor interaction is feasible.
In Fig. 2.7 three different phase-locked averages are depicted. To specify the particular rotor position, the phase-angle is expressed with the corresponding time normalized with the period, $t_\mathrm{n} = t/T$. CFD results are available every full degree. With one rotor pitch having 10°, there are 10 different stator-rotor relative positions available, with every eleventh being a repetition. In the phase-locked figures, the absolute rotor position is indicated by the $\phi_{\mathrm{R,n}}$ coordinates. In addition, the charts are indicating the actual normalized time with the label at the bottom, in which the normalized radius is additionally indicated. As the ϕ_S coordinate will be held fixed from now on, axes labeling is omitted and the space is used for labeling.
In Fig. 2.7a, the origins of ϕ_R and ϕ_S are aligned, which is equivalent to the temporal origin, $t_\mathrm{n} = 0$. The phase-locked stator-rotor interaction can be investigated for every of the aforementioned rotor relative positions. They depict a unique flow field, which is repeated after every rotor-pitch. In the circumferential spatial coordinate however, the periodicity is depending on the blade count ratio between stator and rotor. It turns out, that the necessary blade count for each row is simply defined by dividing its individual total number of blades by the greatest common factor (GCF). For the present stage, blade count is 24 and 36 for the stator and rotor, respectively. Therefore, two and three passages are necessary to reach spatial periodicity.

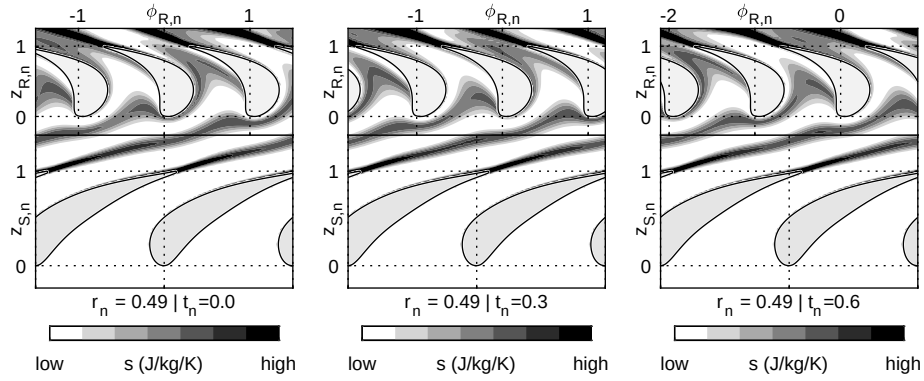

(a) Phase-locked distribution of entropy for $t_\mathrm{n} = 0$

(b) Phase-locked distribution of entropy for $t_\mathrm{n} = 0.3$

(c) Phase-locked distribution of entropy for $t_\mathrm{n} = 0.6$

Figure 2.7: Phase-locked distribution of entropy at mid-span for three different phase-angles: The strong dependance of the characteristic pattern inside the individual rotor passages is clearly noticeable.

Comparing Figs. 2.5c and 2.7a, the dependence of the circumferential periodicity on the averaging method is clearly visible. In the unrelated time-average, it is enough to consider only one passage for each blade rows. As clearly visible from the comparison of the three phase-locked situations in Fig. 2.7, the convection patterns within the three rotor passages differ remarkably, maintaining however the overall periodicity. In all three views, the stator trailing edge wakes are first unaltered in ϕ_S. Further downstream, their characteristic then starts to align to meet the periodicity of the rotor. The corresponding picture is a consequence of the tempo-spatial progress of the convection through the individual rotor passage. As the rotor fulfills its movement, the stator wakes are interacting with the respective rotor relative passage flow.

The rotor blades act as a nozzle. The evolving stationary structures will therefore be accelerated. The exact convection scheme however depends on the individual position of the rotor passage. It is the spatio-temporal characteristic of wakes, vortices and separations leading to the unsteady interaction between two adjacent blade rows. Quantifying the loss share arising from an unsteady wake-blade interaction mechanism, is a challenging task and various experimental and numerical studies are published on this topic. Even if the effect of the time-dependent convection is visible in the phase-locked images in Fig. 2.7, it is not representing the true unsteady wake-blade interaction itself. An uncoupled, individual investigation of a single phase-angle is always an observation of a frozen flow-field consistent to the Eulerian flow specification. The value of investigating phase-locks, especially when considered as concatenated

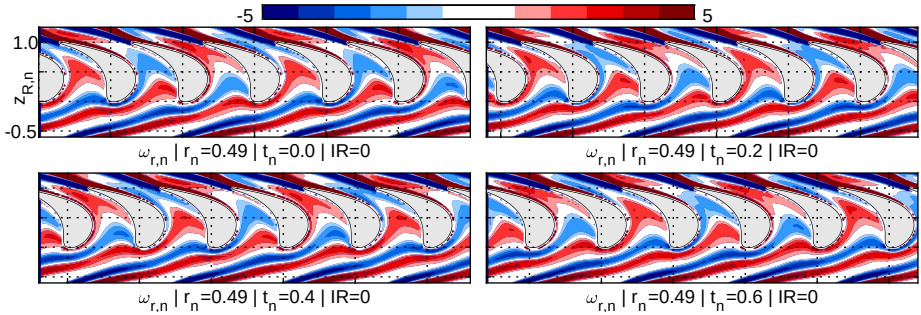

(a) Normalized radial component of the vorticity vector at mid-span - phase-locked time-average

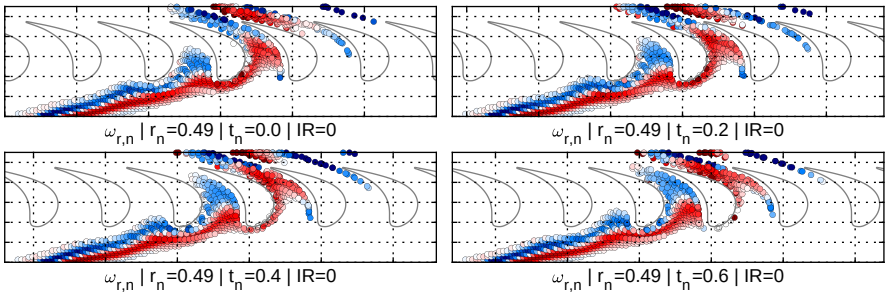

(b) Normalized radial component of the vorticity vector at mid-span - phase-locked time-average initiated at $t_n = 0.0,\ 0.2,\ 0.4$ and 0.6 - Lagrangian specification

Figure 2.8: Phase-locked averages in Eulerian and Lagrangian specification at mid-span

sequences, is however not minored generally.
For a predominantly 2D and periodic flow regime, as regarded here, the additional benefit of switching the method of investigation, is arguable. Due to the planar nature of the flow, every characteristic pattern is linked to the surrounding temporal states [19]. With another look to the three phase-locked situations in Fig. 2.7, the visual correlation of the emerging flow patterns from one frame to the other is clearly given. These observations do however not hold anymore, if the investigated flow field has velocity components normal to the plane, thus loosing the validity of the 2D assumption.

2D Flow Field Consideration - Phase-Locked Average - Lagrangian Specification

To prepare for the 3D flow field investigation, the phase-locked flow data at mid-span is used to introduce to the Lagrangian specification. Figure 2.8a shows the

[19] this statement surely holds only, if potential sources and sinks are identified

distribution of the normalized radial component of the vorticity vector $\omega_{\mathrm{r,n}}$ in the Eularian specification for four different instances $t_{\mathrm{n}} = 0.0,\ 0.2,\ 0.4$ and 0.6. The circumferential range is now enlarged to 6 rotor-pitches to cover the full progress of the corresponding stream traces, as shown in Fig. 2.8b.
Seed-points are positioned in the stator outlet plane on the far left side of the flow domain. The particle-tracing is initiated in every available phase-locked average field, where the spatio-temporal integration of the individual Lagrangian stream-lines is then consecutively fulfilled in the concatenated phase-locked time-series. To finally evaluate a single phase, the stream-traces are filtered to the corresponding time-instances. The fundamental difference between the two flow field specifications are all but visible from the shown data, as they are hiding 90 % of the Lagrangian data. It is the flow-physical consistency of each individual stream line.
In contrast to the Eulerian specification, it is now possible to surely identify the origin of each individual flow pattern. As mentioned before, the benefit is marginal for the 2D flow at mid-span. The possibility of the tempo-spatial tracking of single particles however establishes the segmentation of the expansion path. This is by far not limited to the phase-locked data but can also be applied to a true unsteady time-series, where the position and time of the seed-points can be freely chosen. Furthermore, the integration of the particle traces is not limited in the temporal direction, but can be performed backwards.
To sum up, the value of a robust and computationally efficient tracking algorithm is incomprehensible powerful, when applied to an aero-thermal problem in turbomachinery research. The other way around, the investments to set up and run an integration algorithms may not be underrated. This includes not only a meaningful choice of the seed point distribution but also the post-processing of the stream-traced data. In the scope of this work, the potential of the method is by far not exploited.

Three-Dimensional Flow in Axial Turbines - Introductory Comments

The 2D introduction to the axial turbine aerodynamics is going to be enlarged to a fully 3D consideration. It is seen reasonable to not give a literature review on the general understanding of three dimensional passage flow features, but to focus on the existing flow patterns, as apparent in the actual stage and resolved by the unsteady computations. This is justified with the fact, that the present stage is viewed as an individual item with its unique vortex system, not necessarily reproducing all features published in comparable investigations. Where seen as reasonable though, references are given to commonly referenced work on the general understanding of 3D turbine aerodynamics.
While the stator passage flow field shows general consistency with well known secondary flow structures, the rotor hub-side is strongly effected by the seal geometry, and no exact representative is available in the literature. After this introduction, the stator exit flow field is seen as a given boundary condition, which is generally unaltered,

when the purge flow fraction is changed.

For the visualization of 3D flow characteristics, innumerable approaches and methods are available to the aerodynamicist. However, for the investigation of passage flows in turbo-machinery, the main focus is on the identification and quantification of some specific vortices, in particular those having their origin in the endwall region. Where the flow field at mid span, especially for stages with high aspect ratios, can truly be considered in a 2D manner, this is definitely not possible for the endwall regions.

Due to the high overall Pressure Ratio (PR) of state-of-the-art jet engines, the trend is towards very short blades with low aspect ratios. The share of the span, which might reasonably be considered 2D, consequently decreases. For the first stages of the high pressure turbine, the significance of the endwall induced disturbances, especially the involved losses, therefore pose a dominant challenge in the further development of efficient stage geometries. In R&D, the specific design target is summarized as *secondary* or *endwall loss reduction*, where both terms are used synonymously. For blades and vanes with hub or tip clearances, there is a third fraction predominantly introducing losses, then summarized as *leakage losses*.

As Denton [15] introductorily highlights, a clear distinction between the three loss mechanisms is hardly possible. One simply think about the loss production of an unshrouded high pressure turbine, where the flow field in the tip region will be disturbed by a combination of endwall induced secondary flow patterns and the tip leakage itself. Latter is part of the experimental investigations of the stage as considered in this work, compare Section 1.6 and the dissertation of Wilhelm [67]. In the course of this work, tip leakage will be excluded from the investigations and findings. As true for the entire stator, the effect of the rim seal purge flow is proven to predominantly influence the aero-thermal characteristics in the lower 50 % of the channel.

The basic understanding of typical secondary flow patterns are mainly based on experimental investigations in axial cascades and they go back to the very beginning of gas turbine research. Referencing two of L. S. Langstons publications, the historical development in turbine secondary flow research is well documented from the early 1950s to the early 2000s, see Langston et al. [46] and Langston [45].

Breaking down the phenomena to its essentials, it is the blade leading edge, which depicts an obstacle to the upcoming velocity boundary layer causing a sudden disturbance to the main flow. The pressure gradient within the boundary layer consequently leads to the roll-up of a characteristic vortex. It is formed at the transition between leading-edge and endwall, where the flow locally stagnates. This vortex, commonly denoted as the horseshoe vortex (HV), is then convected downstream by the surrounding flow. Depending on which side of the blade is considered, its further development varies significantly. The HV separates into two legs, denoted as the pressure side leg of the horseshoe vortex (HVp) and the suction side leg of the horseshoe vortex (HVs). They rotate in opposite directions and show clearly different progressions inside the passage, which is mainly induced by the overall circumferential pressure gradient between the pressure and suction side. It is again the nature of the upstream boundary

layer, which leads, irrespectively of the HV, to a cross flow from the pressure to the suction side. The cross flow can be lead back to the lack of momentum inside the boundary layer leading to a higher stream line curvature, see again e.g. Langston [45]. The HVp interacts with the overall cross-flow, where the strength and appearance is generally amplified. This vortex is then commonly denoted as the passage vortex (PV), which is the dominant vortical structure in the rear section of an axial turbine passage.

Vortex Identification

To identify a particular vortex or a combination of such, a clear mathematical formulation is indispensable. Purely based on the velocity vector field, a distinct definition of a vortex is not possible. To proceed, the vortex detection approach, as applied in this work, is now introduced and results are exemplary shown for the investigated stator. Even if a purely visual judgment of a velocity field itself often provides good indications for the potential existence of vortex structures, they are usually inaccurate and depend on the subjectivity of the observer. They are neither applicable for large series of data nor automatable.
In the preparation of this work, different vortex identification approaches have been applied. Certainly, there is space for a further optimization e.g. in choosing iso-values or the general visualization. Different references were used in the selection of the procedure. The basic theory of describing a fluid in motion is taken from Spurk and Aksel [63]. Here, mainly the Eulerian decomposition of the velocity gradient, the deviation of its eigenvalues from the characteristic polynomial together with the invariants are of interest. Once implemented into the evaluation procedure, the method is taken as it is and the focus lies mainly on the application to the investigated 3D flow field of the stage. Highlighting the goal of the present study to contribute to the understanding of the interaction of large scale secondary flow features, this approach is seen to be reasonable.
The vortex detection algorithm, as applied in this work, is covered by the simultaneous analysis of multiple vector field operations, of which only one is classified to be a true evidence of a vortex. This is the second invariant of the velocity gradient, often termed as the Q-criterion. With reference to Jeong and Hussain [41], the Q-criterion formulates the local balance between shear strain rate and vorticity magnitude, where positive values of Q can be used to identify a vortex [20].
Alongside with Q, the vorticity vector $\vec{\omega}$ is considered, where its magnitude $|\vec{\omega}|$ quantifies the local strength of rotation. Providing appropriate values, iso-surfaces can lead to connatural structures when viewed next to Q. Not only the magnitude of the vorticity vector, but also its individual components can sometimes be unbeatable to resolve both, distribution of sense of rotation of vortical structures.

[20] the theory comes along with a second requirement stating that the identified vortex region has to have low pressure, while the definition of a threshold for low pressure is hard to specify, as the discussion in Jeong and Hussain [41] highlights

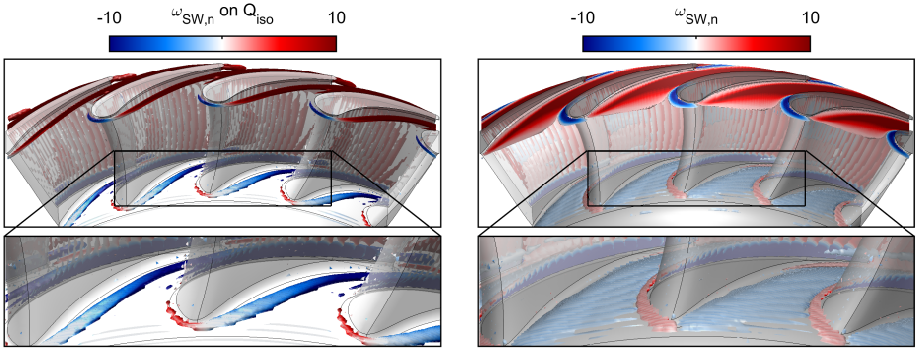

(a) Normalized stream-wise vorticity $\omega_{\mathrm{SW,n}}$ on iso-surfaces of $Q = 1 \times 10^5$

(b) Iso-surfaces of normalized stream-wise vorticity with $\omega_{\mathrm{SW,n}} = [-1,\ 1]$

Figure 2.9: Three-dimensional view on the secondary flow pattern in the stator passage: images are based on the unrelated time-averaged CFD.

In addition, the stream-wise representative of the vorticity vector is formulated, denoted with ω_{SW}. Its exact formulation differs in literature. The general idea is however always based on the allocation of a representative main flow, to which the orientation of the individual vorticity components is referenced. The overall target is to only quantify the share of vorticity perpendicular to the reference. Accompanying the Q-criterion, the established method shows good accordance with the expectations and the identified structures appear to be consistent, visualizable and adequate concerning the computing power [21].

Stator - 3D - Unrelated Time-Average

As introduced so far, the combination of the Q-criterion together with a component of the vorticity $\vec{\omega}$ is used to simultaneously identify the distribution and sense of rotation of the potential vortical structures in the investigated turbine stage. The approach is now applied to the unrelated time-averaged CFD results within the stator passage.
Figures 2.9a and 2.10a shows iso-surfaces for $Q = 10E4$, colored with the corresponding values of the normalized stream-wise vorticity $\omega_{\mathrm{SW,n}}$. As is of primary importance for the present work, the further progress of the vortex structure is discussed for the hub side region only.
The formation of a HV is generally identified. Consistent with the expectation, the pressure side leg rotates counter-clockwise along the suction side. In the Q-iso-surfaces,

[21] this last point is especially true, when comparing Q with the λ_2-criterion necessitating the calculation of the eigenvalues instead of the invariants

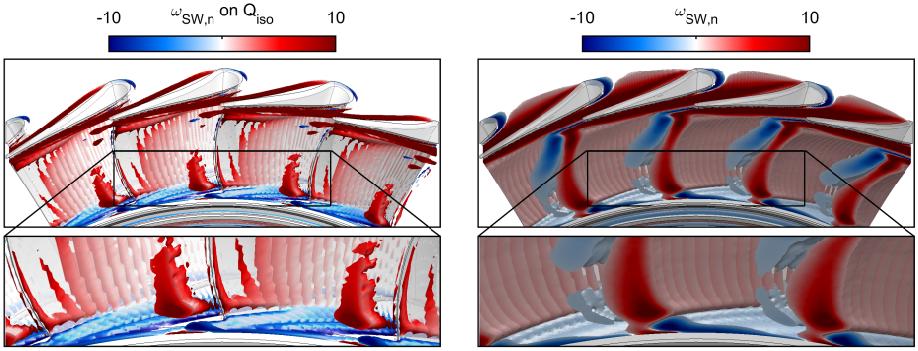

(a) Normalized stream-wise vorticity $\omega_{\mathrm{SW,n}}$ on iso-surfaces of $Q = 1 \times 10^5$

(b) Iso-surfaces of normalized stream-wise vorticity with $\omega_{\mathrm{SW,n}} = [-1,\ 1]$

Figure 2.10: Three-dimensional view on the secondary flow pattern in the stator passage: images are based on the unrelated time-averaged CFD

its counterpart diminishes short after entering the passage. Considering the corresponding position in Fig. 2.9b, $\omega_{\mathrm{SW,n}}$ however preserves the region with the clock-wise rotation and stays visible further downstream. While the 3D view of the passage is suitable for global orientation and a general allocation of the vortex system, data is also presented in corresponding sectional views, where both, a high resolution and clipping enable a detailed look to the flow quantities.

With reference to Fig. 2.11, the hub side region is shown in both, radial and axial sectional views. The progress and interaction of the secondary flow, as identified in the 3D consideration, is now traceable throughout the entire passage. In Fig. 2.11a, $\omega_{\mathrm{SW,n}}$ is depicted for three near wall ϕ_{S}-z planes at normalized radii of $\mathrm{r_n} = 0,\ 0.03$ and 0.06, where the z coordinate is again normalized with the axial chord length of the stator at mid-span. The picture is completed by looking at 12 equally spaced ϕ_{S}-r planes ranging from $\mathrm{z_{S,n}} = -0.24$ to 1.13.

Caused by the near-wall cross-flow, at $\mathrm{r_n} = 0.03$ the entire passage shows high negative values in the stream-wise vorticity. The dominance of the HVp is clearly identified and agrees well with the overall near-wall flow situation. In both radial and axial planes, the evolution of the HVs is now indicated. It stays close to the endwall up to $\mathrm{z_n} = 0.51$, where it begins to be displaced and pushed outwards by the counter rotating large structure, which can now be identified as the PV. At the exit of the passage, the HVs seems to be dissolved, while the trailing edge region is now dominated by another clockwise rotating region, which is apparent over the entire span, compare Fig. 2.10b. The structure is identified as a trailing edge shed vortex (TESV), which is induced by the overall pressure gradient and the associated opposite radial velocities evolving from

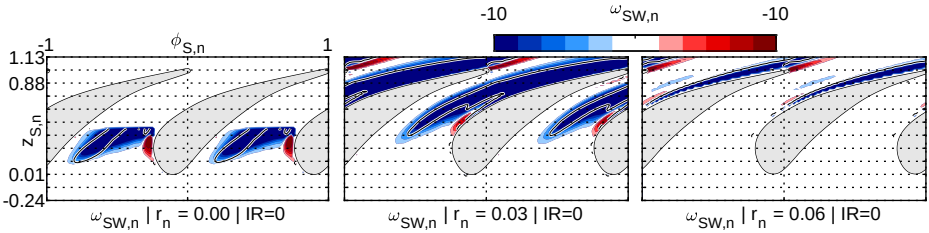

(a) Normalized stream-wise vorticity in three $\phi_{S,n}$-z_n-planes close to the stator hub-side endwall

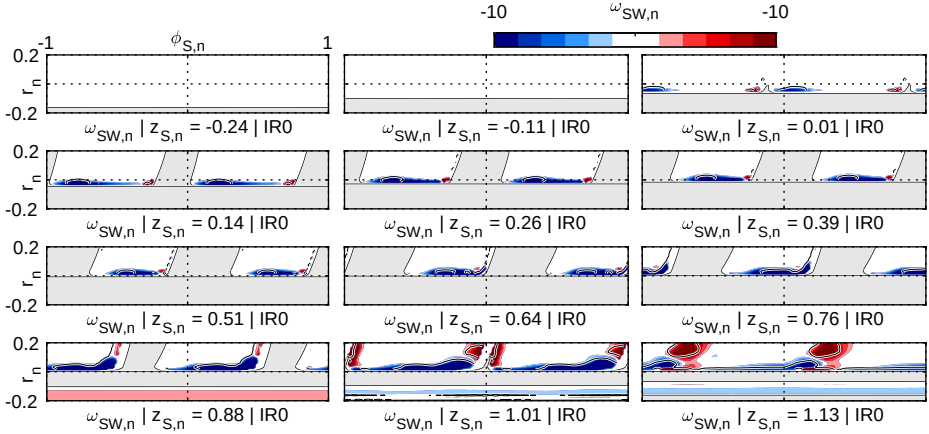

(b) Normalized stream-wise vorticity - stator hub-side - $\phi_{S,n}$-r_n planes - unrelated time-average

Figure 2.11: Secondary flow pattern in the stator hub-side region: the near-wall flow field is dominated by a counter-rotating shear layer, in which the pressure side of the horse-shoe vortex is convected towards the suction-side

the suction and pressure side of the profile. With reference to the last axial position in Fig. 2.11b, PV and TESV begin to interact, where the TESV appears to be divided into an upper and a lower part.

The vorticity distribution at the stator exit, as introduced so far, is from now on considered as the main annulus aerodynamic boundary condition for the purge flow region. As will be shown for the respective rate of rim seal injection, the position of the vortical structures at the stator exit will depend on time, however only marginal when altering the mass fraction of the purge flow.

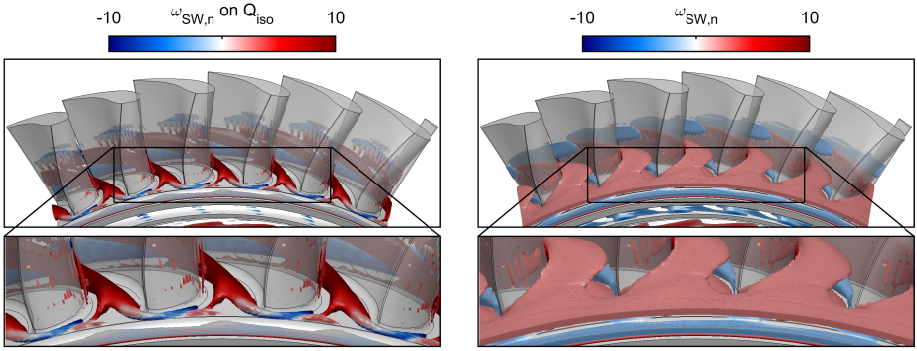

(a) Normalized stream-wise vorticity $\omega_{\mathrm{SW,n}}$ on iso-surfaces of $Q = 1 \times 10^5$

(b) Iso-surfaces of normalized stream-wise vorticity with $\omega_{\mathrm{SW,n}} = [-2,\ 2]$

Figure 2.12: Three-dimensional front view of the secondary flow pattern in the rotor passage: images are based on the unrelated time-averaged CFD.

Rotor - 3D - Unrelated Time-Average

The 3D rotor flow field is now introduced similarly to the stator. The unrelated time-average of the hub side vortex pattern is depicted in Fig. 2.12, where again iso-surfaces for Q are colored with the normalized stream-wise vorticity. To focus on the hub side secondary flow pattern, data is reduced to the lower 60 % span. With a close view to the leading edge region, a HV is generated at the assumed stagnation point. Short after, the pressure side leg, HVp, is dominating the near-wall flow field whereas the HVs, initially visible close to the fillet, is quickly dissolved or not detected by the Q-criterion. Looking at the 3D distribution of $\omega_{\mathrm{SW,n}}$ in Fig. 2.12b and the sectional views in Fig. 2.14 however show, that the counter-rotating flow is apparent up to $\mathrm{z_n} = 0.24$, where it then unifies with the passage vortex.

In addition to the two legs of the HV, there is a third rotating structure detected. It is located close to the suction side, however being *ahead* of the HVs. It has a positive sense of rotation and quickly unifies with the HVp. Its origin is unclear though. As will be shown in the phase-locked consideration, it appears to emerge from the rim seal.

Further downstream, the PV convects towards the suction side, where it begins to occupy the transition between endwall and blade. The region close to the pressure side, now disposable, is filled up with fluid having a negative vorticity. These two counter-rotating vortices are emerging side by side further downstream (from approx $\mathrm{z_{R,n}} = 0.41$ to 0.92). Short after the trailing edge, the passage vortex is then located away from the endwall, while being displaced by the counter-rotating flow. Simultaneously, a large region with negative vorticity is formed at mid-span, which is identified as a TESV with the same motivation as given for the stator exit flow. Between the passage

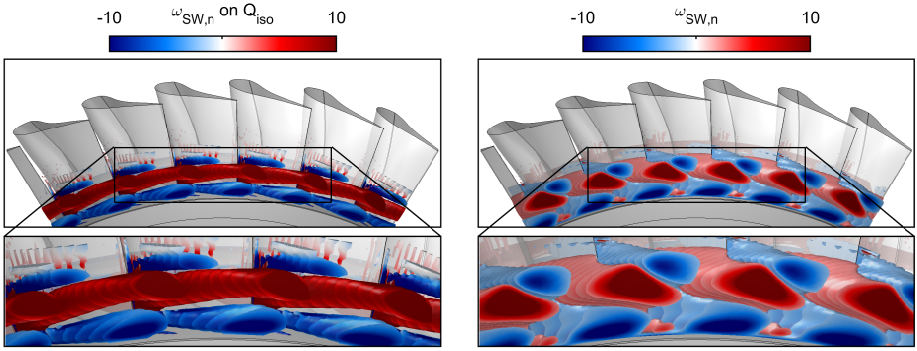

(a) Normalized stream-wise vorticity $\omega_{\mathrm{SW,n}}$ on iso-surfaces of $Q = 1 \times 10^5$

(b) Iso-surfaces of normalized stream-wise vorticity with $\omega_{\mathrm{SW,n}} = [-2,\ 2]$

Figure 2.13: Three-dimensional rear view of the secondary flow pattern in the rotor passage: images are based on the unrelated time-averaged CFD

outlet and the last observed sectional view at $\mathrm{z_{R,n}} = 1.25$, the passage vortex is finally located radially in between a region with negative vorticity, which indicates a strong interaction between TESV, PV and the counter-rotating flow being identified earlier. The 3D distribution of the stream-wise vorticity in Fig. 2.12b moreover discovers a dominating layer with positive vorticity, which is constantly located above the aforementioned rotating flow structures. Looking at the respective planar views in Fig. 2.14, its radial position is constantly around $\mathrm{r_n} = 0.2$. Approaching towards the leading edge, the band is separated and convected into the individual rotor passages. As the passage vortex is constantly moving outwards radially. Having both a positive sense of rotation, they finally coincide at around $\mathrm{z_{R,n}} = 0.58$. Further downstream, they are not distinguishable anymore and they appear to be merged.

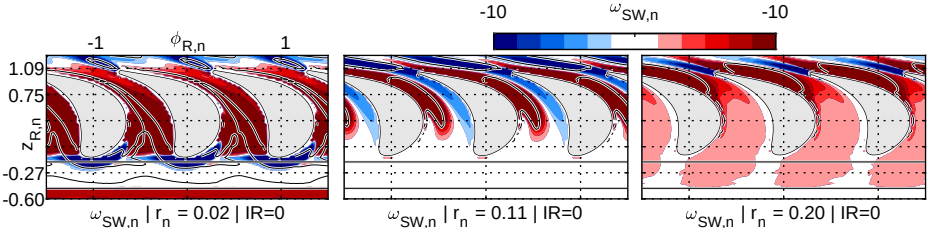

(a) Normalized stream-wise vorticity - rotor hub-side - $\phi_{\mathrm{R,n}}$-$\mathrm{z_n}$ planes - unrelated time-average

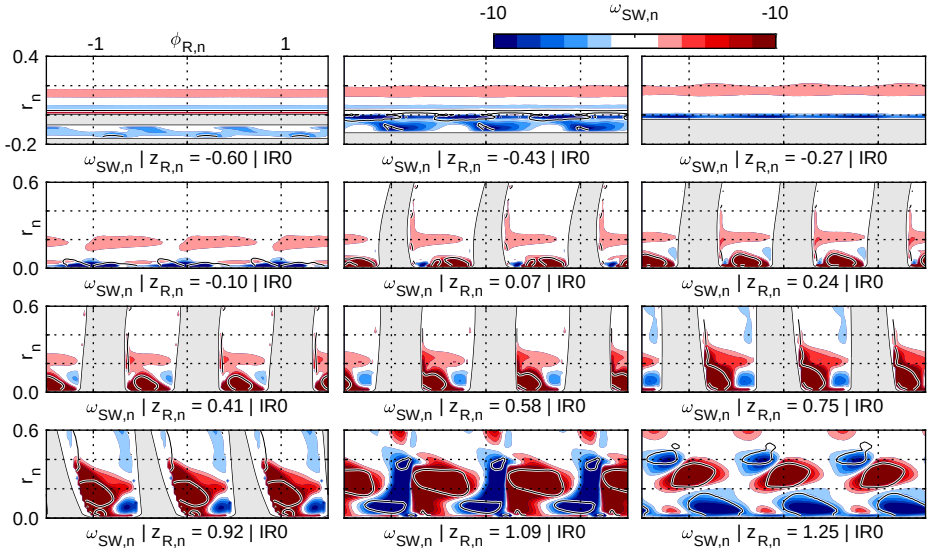

(b) Normalized stream-wise vorticity - rotor hub-side - $\phi_{\mathrm{R,n}}$-$\mathrm{r_n}$ planes - unrelated time-average

Figure 2.14: Secondary flow pattern in the rotor hub-side region - unrelated time-average

2.4 The Issue with Unrelated Time-Averaged Data

Even if not detected as coherent vortices by the Q-criterion, the contiguous layers of vorticity, as apparent upstream of the leading edge, must have their origin in discrete vortical structures. The fact, that the circumferential link is lost in the unrelated time-averaged data, is however not as obvious, as it was at mid-span. To recall, even if the circumferential connectivity is indeed lost, the flow patterns are not disappeared, they are only hidden. The unrelated time-averaged 3D flow field data at the rotor hub, as shown so far, have little value for any detailed flow field characterization.

The question is, how severe the negligence of a circumferential continuity is. As highlighted more than once, the effort for a true, unsteady consideration is incomparably higher than for a corresponding steady approach. A comparison between mid-span and hub-side region is now used to at least cover qualitatively a reasonable argumentation.

For those regions of the flow field with a primarily 2D character in the ϕ-z plane, the effect of a circumferential averaging will have little or no effect to the gradients in the radial direction, as they simply do not exist at any of the sides of a virtual interface. When changing the frame of reference, all consecutive interaction with a flow guiding structure, in the case of the considered stator-rotor interaction this is the convection into the rotor passage, will only be influenced by the artificially enforced evenness in one coordinate, here ϕ. It is therefore adequate to consider and, if possible, to rate the strength and distribution in this single direction. With reference to the three different phase-locked entropy distributions in Fig. 2.7, the cumulated area of the stationary loss patterns only represents a small fraction of the overall interface. To estimate, what a small fraction or a comparably low gradient is, the considered range can be aligned to the limits of the entire stage, as done in Fig. 2.5. When the entire stage is considered in the stationary frame, Fig. 2.5a, the circumferential gradients at the rotor leading edge are almost homogenized. At mid-span, this statement holds for the primary flow variables, as depicted in Fig. 2.6.

The entropy distribution closer to the hub at $\mathrm{r_n} = 0.11$ is shown in Fig. 2.15c. In both frames, the circumferential gradients in the leading edge region of the rotor are now all but homogeneous. If the interface is activated, the effect of the artificial erasure of the circumferential continuity is clearly visible. With the rim seal being located at the interface, the effect of missing either the stationary or the rotating boundary layer is obvious.

The argumentation highlights the necessity to consider the spatio-temporal dependency of the flow field, when the purge flow region is considered. A meaningful characterization is impossible, when only unrelated time-averaged data is available. Based on the unsteady CFD results, the next step is to use the phase-locked averaged data to retrieve the circumferential continuity between the two frames of reference, which is presented in the results section. It is shown, that the evenly distributed elevations in the stream-wise vorticity can be clearly assigned to the lower part of the TESV at the stator exit. Furthermore, the unknown origin of the counter-rotating flow,

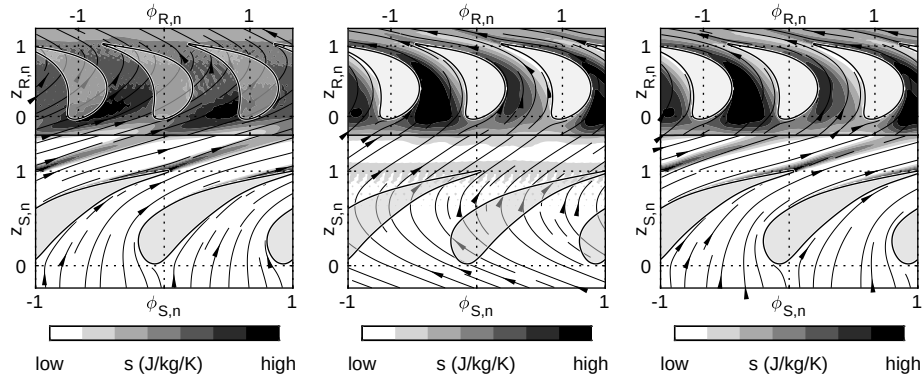

(a) Unrelated time-average in the stationary frame $\phi_{\mathrm{S,n}}$

(b) Unrelated time-average in the rotating frame $\phi_{\mathrm{R,n}}$

(c) Unrelated time-average mixed $\phi_{\mathrm{S,n}}$ and $\phi_{\mathrm{R,n}}$

Figure 2.15: Unrelated time-average of specific static entropy in the hub-side endwall region at $10\,\%$ - The circumferential character at the interface shows high gradients

identified next to the rotor PV, is formed by the interaction of the stator PV with a vortical structure emerging from inside the seal.

3 Methodology

3.1 Experimental Setup

The investigated cavity flow structures are observed in the low-Mach, large scale turbine rig LSTR operated by GLR at Technical University (TU) Darmstadt. Figure 3.1 depicts a flow chart of the facility including a sketch of the turbine section. The first 1.5-stages of a scaled-up model of a high pressure turbine is embedded into a quasi-closed loop main flow duct environment. The primary blower is speed controlled to achieve the desired mass-flow rate as continuously surveyed with a Venturi nozzle. Turbine inlet temperature is controlled via a water-air cooler. A system of blow-off valves allows to adjust the overall pressure level independently of the daily atmospheric condition. A secondary air distribution chamber is fed by an individual radial blower and has its own temperature control system. Behind the distributor, the facility allows to supply several secondary air mass flows, individually controlled with an automatic valve system. The turbine shaft power is delivered to an electric generator, which continuously controls the speed of rotation. A hollow shaft allows signal, pressure and electric energy transfer between the rotor assembly group and a telemetry and slip-ring unit located outside the measurement section. Further details on the data acquisition system in the rotating frame are documented in Allmann [3] and Bargon [5].

The overall stage dimensions are depicted in the 2D sectional view in Fig. 3.1. The radius at mid-span is close to 500 mm. With the hub and casing radius being 434.25 mm and 568.5 mm respectively, the blade height h is in the range of 133 mm, where the exact value depends on the targeted tip clearance.

The rim seal sub cavity is supplied by three tubes evenly distributed over the circumference. They are fed by one of the aforementioned individually controlled secondary supply lines, which is split into three before entering the internal supply unit located in the center of the flow straightener. The feeding plugs are located close to the center of the cavity. Deflector plates are supposed to homogenize and support an even flow distribution within the cavity. To allow a precise control of the purge flow temperature, for each of the three supply lines, through flow heaters are located directly before entering the cavity. A fast response control loop is installed, where the heating power is adjusted to meet the target temperature in the upper part of the cavity.

As enlarged in Fig. 3.1, the sealing geometry has an internal radial gap combined with a diagonal curved chute. For a non-dimensional characterization of seal geometries, a common way is to define the ratio of a characteristic seal clearance and the corresponding radius. For the investigated geometry, the minimum radial distance of 5 mm is taken. Together with the mean radius of 405 mm, the non-dimensional parameter is $s_c/b = 12.4 \times 10^{-3}$.

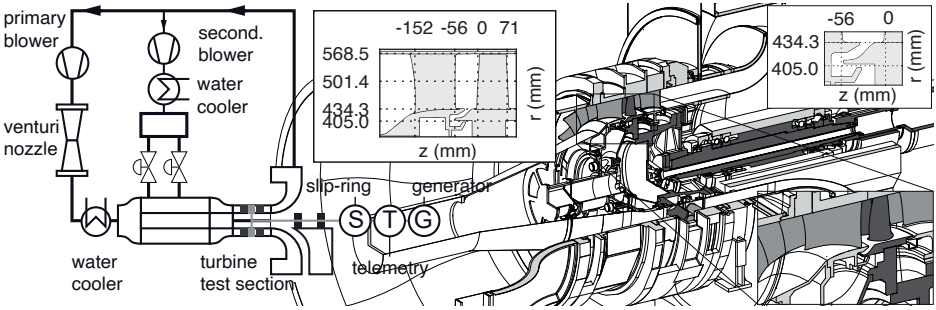

Figure 3.1: Overview on the test turbine facility Large Scale Turbine Rig with details on the investigated rim seal geometry

3.1.1 Operating Point and Turbine Design Parameters

The nominal rotational speed n for the investigations is $1000\,\mathrm{min}^{-1}$, which is equal to an angular speed of $\Omega = 104.7\,\mathrm{rad\,s}^{-1}$ or a circumferential hub velocity of approximately $43\,\mathrm{m\,s}^{-1}$. Based on this angular speed, a corresponding rotational Reynolds number can be defined for the seal, which leads to $\mathrm{Re}_\Omega = \rho\,\Omega\,b^2/\mu = 1.004 \times 10^6$. To meet the stage design flow coefficient, the main rotor inlet mass flow $m_{2\mathrm{B}}$ is held constant at $10.33\,\mathrm{kg\,s}^{-1}$, irrespectively of the appropriate purge flow rate. As a consequence, the stator mass flow is aligned to the differing purge flow rate. This approach appears arguable, as an investigation with constant stator mass flow would be meaningful as well. This is especially true, if considering the fact, that the first NGV is often choked in the design point.

As this thesis is mainly focused on the rotor passage flow, targeting a constant flow coefficient without altering neither the pressure level nor the rotor angular speed is preferred here. The rim seal purge flow mass fraction, defined as the ratio of stator outlet and rim seal purge mass flow rates, is varied in the range of 0 % to 2 %. Stator exit Mach numbers are in the range of 0.24 (absolute velocity $85\,\mathrm{m\,s}^{-1}$) leading to a Reynolds number $\mathrm{Re}_\mathrm{S} = 4.875 \times 10^5$ with respect to the axial chord length (at midspan).

In general, the rig is operated at cold conditions and target temperatures are chosen with respect to both, the cooling capacity of the water-to-air coolers and the maximum allowable material temperature of the employed materials. As will be discussed in the heat transfer section, the applied measurement concept depends on a precise temperature difference between main and secondary flow. As a third precondition, a fast and reliant achievement of thermal equilibrium is considered when choosing the target flow temperatures. For this study, a temperature difference of 10 K between rim seal and main flow is chosen, with 313.15 K and 323.15 K for main and secondary air, respectively.

Variable	Description	Value	Unit
r_h	hub radius	434	mm
r_c	casing radius	568.5	mm
h_R	blade height	132	mm
n	rotational speed	1000	1/min
$m_{2\mathrm{B}}$	rotor inlet mass flow ($m_{2\mathrm{A}} + m_\mathrm{C}$)	10.33	kg/s
Re	Reynolds number stator exit	4.875×10^5	-
Φ	flow coefficient	0.46	-
p_1^0	turbine inlet total pressure	1.1×10^5	Pa
T_1^0	turbine inlet total temperature	313.15	K
BC	blade count S1,R,S2	24, 36, 32	-
Ψ	temperature drop coefficient	-3.8	-
b	seal radius	0.405	m
s_c	seal clearance	5	mm
Re_Ω	rotational Reynolds number	1.004×10^6	-
ψ_C	purge flow fraction ($m_{2\mathrm{A}}/m_\mathrm{C}$)	0, 1, 2	%
$T_{t,cav}$	cavity inlet total temperature	323.15	K

Table 3.1: Operating conditions and geometrical properties of the test turbine

All relevant design parameters are summarized in Table 3.1. Further details on the rig operation, its stability and overall measurement accuracy can be found in Eitenmüller et al. [16]. A full description on the investigated stage, with focus on the aero-thermal impact of different turbine inlet conditions to the blade tip region, is covered in Wilhelm [67].

3.1.2 Aerodynamic Instrumentation

Within the measurement section, a wide variety of aerodynamic instrumentation is installed. To allow a distinct determination of the overall turbine performance, a number of stationary pressure and temperature measuring points are permanently located in various measurement planes of the test section. With reference to Fig. 3.2, stagnation pressure and temperature Kiel-rakes are installed in measurement planes MP01 and MP05 accompanied with static wall pressure tabs circumferentially distributed on the outer casing in all relevant measurement planes MP00S to MP05. The outlet is furthermore equipped with circumferentially distributed wall pressure tabs at the hub endwall to allow a permanent control at the outlet.
The rim seal cavity itself is instrumented with a number of temperature sensors and pressure tabs in two representative radial positions. First, the sub cavity is equipped with in total eight static wall pressure tabs and four type K thermocouples protruding away from the stator endwall.

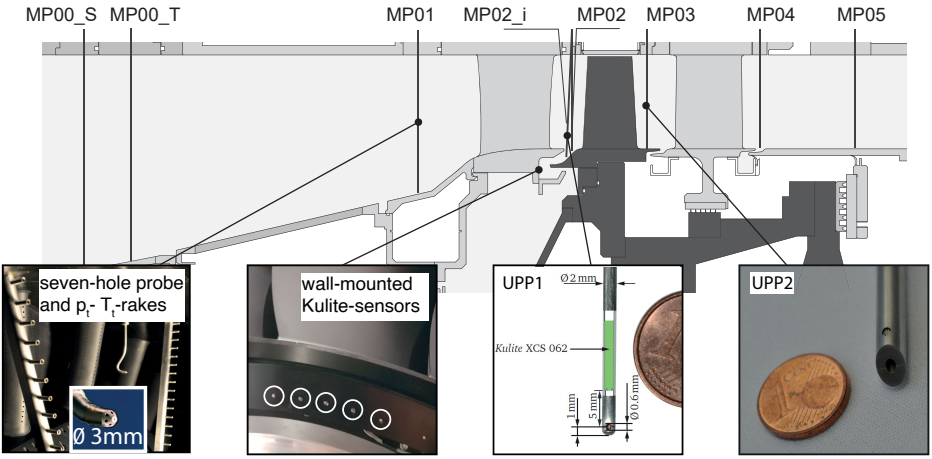

Figure 3.2: Measurement planes and aerodynamic instrumentation

Time-averaged, two-dimensional flow vector information is determined via a traversable multi-hole probe system. The rig environment thereby follows a combined concept, in which the relative radial position is altered via individual probe towers. The circumferential movement within the flow field however is realized by a rotation of the stationary flow guiding structure. In total, three rings can be rotated individually relative to the stationary casing. One ring located far upstream of the stator inlet (MP00_T) and two rings holding the fist and second stator vane rows. Silicone O-ring gaskets are placed in every junction for sealing. The turbine inlet velocity field is measured with a Seven Hole Probe (7HP) capable of resolving high flow angels and calibrated for the expected absolute velocities in MP01. In MP02 and MP03, cobra-type Five Hole Probe (5HP) are used to resolve the time-averaged flow field. A detailed description of the design philosophy of the rig is given in [43].

To investigate the rotor relative flow field up- and downstream of the blade row, two Unsteady Pressure Probe (UPP) are applied. For the rotor inlet plane, a probe containing one commercially available Kulite-sensor is used. The sensor is located in a capillary tube with an outer diameter of 2 mm. A hemispherical plug at the end of the tube contains an orthogonal hole with a diameter of 0.6 mm. This design guarantees a spot-wise measurement with an adequate frequency bandwidth, compare Fig. 3.2. In the following, this probe is denoted as Unsteady Pressure Probe with One Sensor (UPP1). Within the campaign, the UPP1 was continuously operated as a virtual three hole probe allowing the deviation of most important flow quantities [1]. To allow the

[1] the limitation to one sensor does not allow a reliable deviation of the radial angle, while the velocity amplitude and both, the total and static pressure are

investigation within the mixing zone of purge and main flow, an inclined measurement plane (MP02i) is established, where the access is realized via an access plug in MP02. Detailed design specifications, the static and dynamic calibration method and a summary of the conducted measurement campaign is documented in Filius [19].
The rotor relative exit flow field is surveyed with an in-house built virtual four-hole probe. The probe is now equipped with two unsteady pressure sensors, therefore now denoted as Unsteady Pressure Probe with Two Sensor (UPP2). Details of its geometries, the static, dynamic and aerodynamic calibration as well as the evaluation procedure are documented in and Polidar [53].
It is highlighted that for the present study, the aerodynamic calibration was not applied at all and the digitized signal is simply transferred to pressure with the static calibration. Due to the consecutive character of the virtual hole method, the post processing is based on phase-locked averages. Therefore, all flow quantities based on the virtual mode are not suitable to resolve the large scale cavity structures. Thus, throughout this work, both probes should better be considered as unsteady total pressure probes. The orientation towards the main flow direction is thereby based on previous 5HP measurements.
To experimentally resolve the pressure information within the cavity in time and space, in total five sensors are installed in the stationary part of the rim seal cavity. They are evenly distributed over one stator pitch. For the results presented in this work, they are simultaneously logged with the unsteady probe measurements. This allows to correlate the rotating structures inside the cavity to their propagation into the main flow field.

3.1.3 Heat Transfer Instrumentation

To experimentally investigate the influence of the injected purge flow to the aerothermal condition on the rotor hub side endwall, the rotor is equipped with a high resolution heat transfer measurement system. With reference to Fig. 3.3, the approach is based on the acquisition of wall temperature maps. A fast infrared imaging system determines the distribution of radiation intensity of an instrumented rotor endwall segment. The setup allows the quantification of spatially highly resolved heat flux information over a thin insulation layer coated to the flow facing surface of interest. A regression based method is then used to derive the adiabatic wall temperatures and the local heat transfer coefficients on the basis of a series of thermal boundary conditions. Implemented feedback controlled electric heaters are used to set a series of steady state thermal boundary conditions. The instrumented thermocouples and the electric power are transferred between stationary and rotating frame of reference via the telemetry and slip ring unit, as was introduced in the beginning of this section. As presented in [50], the data processing algorithm and therefore the calculation of the heat flux distribution is carried out frame by frame. Besides evaluating the results from the regression based on a full measurement series, each individual thermal boundary

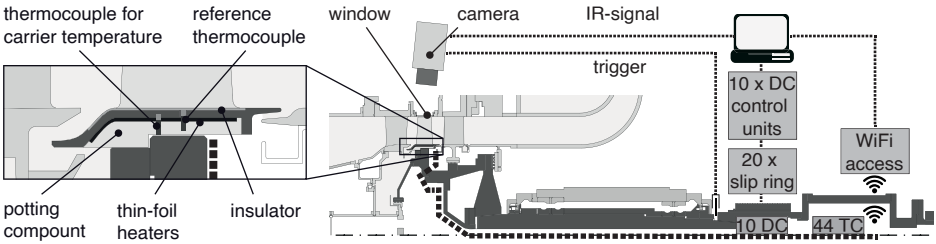

Figure 3.3: Experimental heat transfer setup

condition incorporates an instant picture of the temperature distribution at the rotor hub side endwall. As only one single rotor endwall segment is instrumented and the maximum frame rate of the camera prohibits multiple subsequent snap-shots of one rotor bypassing event, infrared images are only available every second full revolution. It is highlighted, that this comparatively low acquisition frequency is of different order than the unsteady pressure information as recorded with the Kulite-sensors.
For the results presented in this work, the focus however lies on the evaluation of instantaneous surface temperatures. Therefore, the regression based phase-locked heat transfer quantities are not of major interest. This is again based on the consecutive character of the method, where the single supporting points for the regression are ensemble averages. As will be discussed in the results section, the sequence with thin film heaters fully switched off are analyzed towards fluctuations. For the in-situ temperature and spacial calibration however, the complete data reduction procedure is applied. For detailed information on the measurement principal, the algorithm and the determination of relative and absolute uncertainties, the reader is again referred to Ostrowski and Schiffer [50]. Overall findings from the full thermal measurement campaign, where not only the sealing mass fraction was altered, but also the turbine inlet flow field as well as the purge flow pre-swirl are documented in Fischer [20].

3.2 Numerical Setup

For all three experimentally investigated purge flow mass fractions, time-resolving computations are conducted using the unsteady Reynolds averaged Navier-Stokes (URANS) solver implemented in ANSYS CFX 18.2. The domain is based on a 3D extraction from the actual Computer Aided Design (CAD)-model, where each blade row is represented by a single passage with the blades being positioned in the center. The absolute origin of the coordinate system is equal to the one committed for the experimental data. Here, a clear definition of the circumferential stator orientation is of great importance, as a correct alignment reduces the error rate coming along with the then necessary rotational adjustment of the numerical and physical coordinate systems. More details on the experimental coordinate system are given in Wilhelm

[67, Sec. 4.1.3].
The axial dimensions of the three domains are adapting suitable positions of the available measurement plains. Referencing Section 3.1.2, measurements upstream of the stator are generally possible at three axial positions, namely MP00_S, MP00_T and MP01. The two far upstream planes are close to the nozzle exit [2] , leading to a high level of homogeneity in both, the flow variables and the expected turbulence level. In addition, the exact evolution of the boundary layer characteristic towards the stator passage is part of the numerical solution. Depending on the quality of the boundary layer treatment, this can have a positive effect to the overall goodness of the prediction. However, this approach comes along with the increased overall numerical costs. Furthermore, the reference plane to characterize the inflow to the stage has always been in MP01, while the other two planes are assigned to the combustor simulator inlet. Eventually, all 2D multi-hole probe measurements, as conducted within the experimental campaign, are available in MP01, MP02 and MP03. To summarize, for the present work, the only practical option for locating the inlet plane is MP01. The approach for the deviation of the inlet boundary conditions is followed up in Section 3.3.
To locate the interfaces up- and downstream of the rotor, the choice can only fall on MP02 and MP03, where some details on the exact shape of the rotor inlet will be given in the next section. With respect to the position of the numerical outlet, it is common practice to always try to avoid high gradients in the corresponding flow regime. The stability suffers strongly on any potential back flow. For a turbine stage, the axial position must not lie too close to the last existing trailing edge, as all secondary flow structures should be mixed out to an acceptable level. For the investigated stage, this basic rule excludes MP04, while MP05 fulfills the requirements. The resulting range of the entire domain is depicted in Fig. 3.4. Having motivated the axial expansion so far, the radial one is not of minor interest. This is especially true, when focusing on a third opening to the domain, here represented by adding the purge flow to the model. Choosing the numerical extent of the wheel space and seal geometry can have major impact to the predicted flow patterns in the interaction of main and seal flow, as highlighted in the literature review, Section 1.4.1. To take this fact into account, a large portion of the sub-cavity is added to the domain. As indicated in the sketch, the radial extent of the domain is therefore approximately doubled in the respective area. This distinct expansion however comes along with a considerable increase of the computational costs. To counteract, the domain is defeatured, where reasonable.
As mentioned in Section 1.6, the test turbine geometry was designed to allow investigations with a focus on cooling features within the first stator section, see e.g. Werschnik et al. [66]. For the present numerical investigations, namely two features are removed to focus on the time-resolved calculations of the rim seal purge flow effect. First, the discrete pattern of cooling holes upstream of the stator hub side endwall is removed. Second, all cooling holes and the trailing edge slots of the stator profile

[2] to avoid confusion, here the nozzle between the flow straightener and the combustor simulator is meant, not the NGV

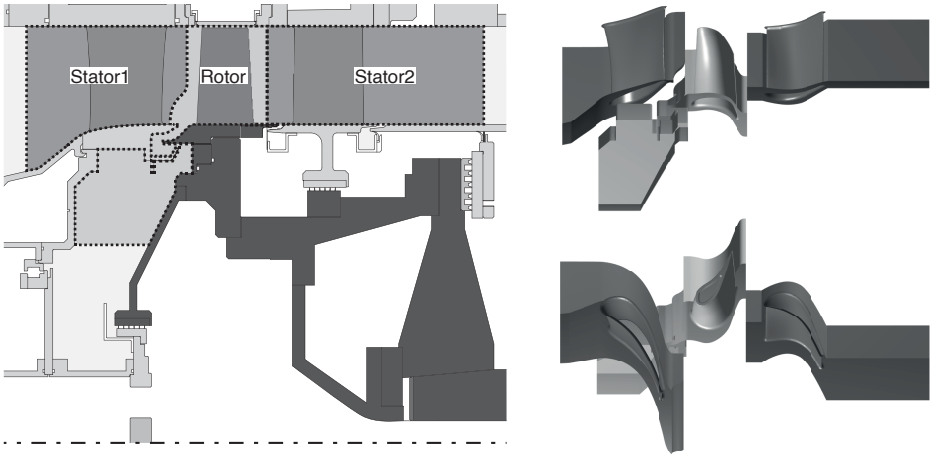

Figure 3.4: Numerical setup: A large portion of the wheel space is part of the rotor domain to allow large scale rotating structures to develop in the rim seal region.

itself are replaced by solid walls. This approach strongly differs from all numerical and experimental investigations, as previously conducted on this test turbine.

3.2.1 Domain and Mesh Details

In total, a 60° sector model, consisting of four first stator airfoils, six blades and six second stator airfoils, is assembled. As no integral count of 32 second stator airfoils fits into 60°, the number is artificially increased to 36. To facilitate the potential development of the expected cavity structures, the wheel space is largely incorporated into the domain. As illustrated in Fig. 3.4, the wheel space is part of the rotating domain. The interface to the first stator is not planar but shows a bow close to the hub. For steady state calculations, where a mixing plane needs to be located somewhere in the stator-rotor interfaces, this shape showed more stable convergence compared to a setup with a flat interface. However, for the URANS calculations, the shape and exact position of the interface has no influence on the result.
The meshes for all three single blade rows are generated with the commercially available automatic grid generator CENTAUR, following a hybrid mesh topology. Prismatic layers are used in the vicinity of the walls, whereas the open flow regime exists of tetrahedral elements. The mesh, as finally used for the URANS computations, is the result of an iterative mesh density variation. The individual convergence characteristics however are based on steady state calculations with the above mentioned bow-shaped mixing plane and single vane and blade segments. Due to persistent numerical instabilities in the rim seal region, a definite conclusion of the mesh study was unreliable leading

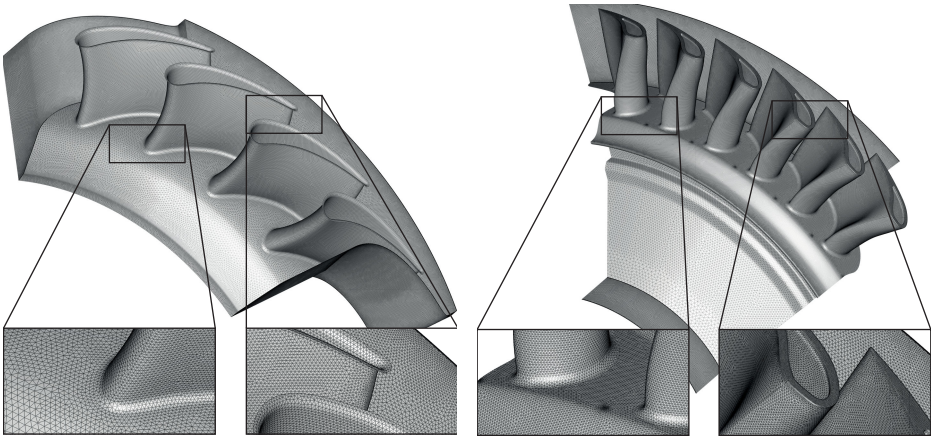

(a) Mesh details for the stator domain **(b)** Mesh details for the rotor domain

Figure 3.5: Detailed views of the unstructured meshes in the stator and rotor domain

to the final nomination of a mesh with a density and topology similar to previous computational investigations of the LSTR.

The 60° meshes for the unsteady computations are assebled by duplicating the single passage topologies. The entire domain contains 84.4 million cells, from which 13.19 are prismatic and within the boundary layers.

3.2.2 Turbulence Model and Temporal Discretization

Similar to selecting the mesh, the choice of the turbulence model, here the Shear Stress Transport (SST) model, is based on the knowledge and experience from previous investigations, as conducted at the GLR and other research in the field of applied turbomachinery investigations. This very brief and noncritical motivation on choosing this very fundamental approach of describing the incredibly complex nature of turbulence, especially when targeting a better understanding of a phenomena primarily driven by the fluctuating interaction of a fast moving blade row, may seem foolish. At this point however, it is again reminded that in this work, the CFD must clearly be seen as an enabler to strongly increase the otherwise limited spatio-temporal resolution of the experiments. As will be presented in detail in Section 3.3, this is mainly backed up by two reasons. First, the computational boundary conditions are directly based on its experimentally investigated counterpart itself. In this sense, naming the computational result a prediction is somehow misleading. Second, the computed flow field inside the domain is validated against a number of local and global quantities and parameters, as being the result of the experimental effort itself.

Time step is chosen to resolve 40 positions per rotor pitch corresponding to 0.25°. In total, three full revolutions, equivalent to 4420 time steps, are solved. The calculations are initialized with a steady state solution. A maximum number of 10 internal loops is prescribed. The transient term is discretized with the Second Order Backward Euler Scheme without a limitation of the Courant Number.
All transient computations are conducted on the Lichtenberg High Performance Computer at TU Darmstadt. In the transient result files the total pressure, total temperature and the velocity vector, all in the stationary frame, were written for every fourth time-step leading to a one degree or 1/10th rotor pitch resolution. The first revolution is unused in post-processing to allow convergence of the large scale fluctuations. Global characteristics of the rotating flow structures are observed to be unchanged for the second and third revolution allowing the assumption that they are fully developed.

3.2.3 Downsampling, Restructuring and Visualization

As mentioned in the previous section, the transient results are evaluated for two full revolutions. The solver is set to write every fourth time-step to the CFX transient file format leading to 720 files containing the six governing flow quantities on almost 85 million elements [3].
For the identification and quantification of convecting and highly time-dependent large scale structures, the development of a routine to enable a fast and efficient processing of the data is inevitable. Furthermore, changing the frame of reference and employing the respective statistics in the 3D region comes along with major difficulties regarding the computing power. To overcome these issues, the Area of Interest (AOI) is interpolated onto a regular and coarse volumetric mesh. Depending on the resolution, such data handling strategies enable a considerable down-sampling. The mesh is structured in a monotonously growing cylindrical coordinate system, which has multiple decisive numerical advantages regarding the deviation of gradients and the overall investigation of the results. The procedure also incorporates a circumferential data restructuring to now match a 60°-sector, centered to the vertical axis. The procedure guaranties the correct allocation within the turbine coordinate system and makes 3D vector field operations highly efficient.
The expansion and resolution of the mesh, as being used throughout the data presented in this work, is the result of an iterative procedure, accounting for both, the validity and the storage demand of the interpolated data. The final mesh is based on a ϕ-wise step-size of 0.25°, leading to 60 and 40 elements per stator and rotor pitch, respectively. The spatial resolution in the r and z direction are based on the corresponding arc length at mid-span. The axial expansion of the volume ranges from the inlet boundary to the rotor exit plane whereas the radial coordinate lasts from

[3] each having a file size of $\approx 365\,\mathrm{MB}$, leading to a memory requirement of $\approx 263\,\mathrm{GB}$, in case the full time-series has to be processed at once

−0.5 to 1 normalized radius. In total, this leads to a regular 101x240x166 r-ϕ-z mesh [4]. The computationally inexpensive and platform independent access to the transient CFD results enables the implementation into any possible evaluation procedure.
The capabilities coming along with the restructured computational data are applied throughout this thesis. All specific evaluation and visualization procedures are initialized with a global load and pre-processing routine. The benefit of such an approach may not be underrated, as it guarantees a consistent data handling. Independent of the actual frame of reference and the respective time-domain, [5] all are handled synonymously by the sub-routine, where, on the basis of the six fundamental flow quantities, all thinkable deviations are performed. The particular operations are explained and referenced at the specific sections of this document, where seen as necessary. In general, the routine applies well known formulations from fluid dynamics assuming a perfect and compressible gas. It also performs vector analysis, where especially the transformation of velocity components, the velocity gradient, the curl and the calculation of the stream-wise vorticity are of primary interest for this work. Furthermore, the consequent application of mass and area averaging for the deviation of the 2D and 1D stage parameters is performed.
All data evaluation and visualization procedures are developed and performed in MATLAB, where the latest executions are conducted in the 2020A version. In many cases, the interpretation of flow field quantities is considerably enhanced, when they are visualized in conjunction with the relevant surrounding structure. To provide a well-ordered access to the relevant turbine geometries, a library of graphical objects is made available to the MATLAB work-space. Based on the CAD-model of the stage, 3D surfaces and edges are derived and exported, using the vendor-neutral file format Initial Graphics Exchange Specification (IGES). Based on the IGES toolbox from the MATLAB file exchange data base, the objects are imported and converted to simple patches and lines. The compactness of such well-defined objects enables high graphical performance while maintaining an adequate grade of detail. Having direct access to the underlying coordinates, a manipulation is straight forward. For instance, the visualization of the annulus based geometries of a turbine stage in the virtually unfolded ϕ-z plane can be achieved with one line of code, where the coordination transformation is executed.
In addition to the self-generated graphical objects, the available connectivity matrix together with the coordinates and quantities of the computational surface meshes are easy to load in interpret as patch-objects. A major drawback of the volumetric downsampling is the elimination of the mesh refinement near the walls. To overcome this issue, surface quantities of interest are exported and again, where required, re-sampled to the appropriate and regular cylindrical coordinate system.

[4] This equals to approx. 4 million nodes, which is a reduction of almost 94 %, compared to the approx. 62 million elements of the corresponding original mesh. The matrices of the six flow variables are archived in .csv-files for each operating point and the 720 time-steps.
[5] this can be an unrelated average, a specific phase-locked or an instantaneous field

3.3 Computational Boundary Conditions

As valid for the setup of any digital representative of a physical process, the accuracy and confidence of the result is strongly depending on the quality and plausibility of the predefined conditions on its boundaries. The model may neither be over-determined nor fed with an excess of simplifications or even being under-determined. The application of CFD in the field of turbo-machinery R&D nowadays can be considered as a well developed and ready-to-use tool kit. Commercially available packages for fluid dynamics simulation, in this case Ansys CFX, are delivered with well prepared user's guides. With a look to the structure of such manuals, the outstanding significance of choosing well-considered boundary conditions is obvious. Decades of experience on the successfull conduction of innumerable and highly diversified simulations, application oriented frameworks are available on handling the specific challenge of boundary condition definition.

3.3.1 General Considerations on Experimentally Based Boundary Conditions

As already pointed out for the mesh and turbulence model, the choice of setting up the boundary conditions for the actual CFD is based on such available frameworks and, after declaring early results for plausibility, the approach of deriving and implementing the boundary conditions was fixed and unaltered between the three investigated operating conditions.
For the present CFD domain, the conditions on all flow facing walls is straight forward. They are globally declared as no-slip and adiabatic. Where appropriate, the relative movement is defined by the rotational speed. Furthermore, the apparent circumferential periodicity is straight forward and no further details need to be addressed here.
In the following, the definition and derivation of the flow conditions at the three open boundaries, namely the main inlet upstream of stator 1, the main outlet downstream of stator 2 and the cavity inflow, are presented in more detail. For modeling the flow through the turbine, CFX predominantly recommends three different combinations on the open boundaries. They mainly differ in the expected robustness, where the combination of a predefined velocity or mass flow at the inlet in combination with a static pressure at the outlet is considered to be the most robust. The second combination is a total pressure at the inlet together with velocity / mass flow at the outlet. In both combinations, the system mass flow is not an implicit part of the solution. The third, declared as sensitive, is to provide a total pressure at the inlet and a static pressure at the outlet. In this case, the systems mass flow is an implicit part of the solution. Depending on the accuracy of these two pressures and the expected pressure drop within the system, it is obvious, that the resulting mass flow can potentially be altered strongly by small pressure variations at the boundaries.
However, it should not be jumped to conclusions solely on the basis of this general and hierarchic listing. For the present case, where all named quantities are based

on measurements, the question of numerical robustness may end up lower-ranked in contrast to uncertainties arising from the measurements or their preparation. Certainly, it still depends on their general availability at the respective boundaries.
The main inlet to the domain is chosen with respect to MP01, where for all three operating points a 30° sector of the flow field is available from the 7HP traverses. In the outlet plane, axially aligned with MP05, static pressure tabs are available at hub and casing. The mass flow entering the measurement section is continuously derived from the Venturi nozzle.
With these quantities available, a valid inlet boundary condition can be generated in three ways. First, the mass flow is taken from the Venturi nozzle [6], possibly combined with the 2D distribution of the flow direction from 7HP. Second, the velocity magnitude together with the direction is taken, again from the 7HP and third, again based on the traverse, a total pressure boundary condition can be generated. For the outlet at MP05 either the static pressure or the mass flow is chosen.
If these three possibilities are rated equivalently, the combination of mass flow at inlet and static pressure at exit should be chosen in accordance to the expected robustness. This boundary setup however showed large deviations comparing the predicted velocity magnitude with those from the 7HP and 5HP traverses using results from preliminary, stationary computations. Thereupon, the assumed absolute accuracy of the Venturi nozzle is questioned. As a consequence, the application of a mass flow boundary condition, regardless of being used at the inlet or exit, was not further considered in the present numerical setup.
The next and obvious alternative is to prescribe the velocity distribution from the 7HP. In this case however, issues arose from the limited experimental sample points in the endwall regions. Attempts to interpolate the missing velocities again led to large deviations when validating now with the 5HP measurements in ME02 and ME03. The most probable reason is given in the high sensitivity towards the assumed velocity profiles supporting the interpolation.
The issues with the mass flow and the velocity, as described so far, finally lead to the choice of the combination of inlet total pressure and exit static pressure. This approach still relies on filling up the 7HP-traverse towards the endwalls. The interpolation method, now applied to the total pressure, however showed much less sensitivity. This statement is again based on a series of validated preliminary calculations.

3.3.2 The Deviation of Physically Valid Boundary Conditions from Traverse Measurements

Independent of the finally applied combination of boundary conditions, one fact is crucial but often neglected if a consecutive measurement method is involved; while the CFD, if converged, will always represent one single operating point, the experimental

[6] assuming perfect homogeneity, the mass fraction corresponding to the sector size of the domain is taken

data will however incorporate unavoidable fluctuations. For an intrusive measurement technique such as multi-hole probes, its consecutive repositioning will unavoidably alter the operating point. For a continuously operated test turbine, inevitable fluctuations arising from the re-adjustment and the changing ambient condition will always come on top.
To overcome this issue, a correction procedure is applied to the traverse measurements. It is based on the approximation of a representative operating point, which is determined on the basis of the averaged flow quantities over the full measurement series. The instantaneous operating condition is then identified with a representative reference value, which is ideally unaffected by the individual measurement situation itself. For the present set of probe measurements, a good representative is one single static pressure in MP00T. Compared to the stators, its relative circumferential location is held constant making it invariant to the actual clocking position of the stationary flow field. While its average stands for the hypothetical operating point, the instantaneous value is used to correct for any of the aforementioned fluctuations. The approach is now briefly sketched for the 2D distribution of the total pressure in MP01, as being determined with the 7HP. Its mathematical formulation is simply given by

$$p^0_{1,corr} = \overline{p}_{00T} + p^0_1 - p_{00T} \tag{3.1}$$

Depending on the temporal characteristic and amplitude of the global fluctuations as well as the spatial arrangement of the traverse, the method can compensate for potential physically unlikely gradients in the field. For the deviation of the flow boundary at the inlet, the correction scheme is applied to the traverse and the static casing pressures prior to the interpolation.

4 Results and Discussion

4.1 Validation of the Computational Setup

A great portion of the interpretations and conclusions, as given in this thesis, are based on the CFD results. Such practice however can only be legitimated, if the computed flow field is checked for its validity. To do so, both, the CFD and experimental results are now considered in the different coordinate systems, as introduced in Section 2.3. The focus will first lie on the validation of the overall flow field, as apparent up and downstream of the rotor blade row. Using the traverse measurements in MP02, MP02i and MP03, a combination of both, the 5HP and UPP, are compared to the CFD.

A validation of the averaged flow field in the rotating frame of reference is then only possible on the basis of the UPP. As highlighted in Section 3.1.2, the UPP data is limited to the time-series of the signal, where only the static calibration is applied for the conversion to engineering units. At first, this may seem like a restriction, as the full potential of the virtual hole mode lies in the delivery of the flow vector. The identification and investigation of the rotating and non-related cavity structures, however, would then be moved out of focus. This section will mainly show the capability of the CFD to qualitatively reproduce key characteristics within the flow regime. Where necessary, a brief reference will be given to the corresponding flow structure.

4.1.1 Flow Field Validation - Stationary Frame of Reference

To begin with, the computed unrelated time-averaged flow field is compared to experimental data in the available 5HP traverses. From the wide variety of flow variables available, the pressure loss coefficient Y and the absolute whirl angle α are chosen here. While Y is considered to be a good indicator for the prediction of secondary flow patterns and the herewith connected dissipation, α represents more generally the overall capability to correctly predict the interaction between the turbine geometry and the flow.

Consistent to the dominant circumferential periodicity, $\phi_{\mathrm{S,n}}$ is limited to one stator pitch. The normalized radius ranges from 0 to 0.8. Figure 4.1 shows both, 2D distributions and circumferential averages in the respective planes. For each plane and flow variable, 5HP, CFD and the circumferential averages are shown side by side.

Pressure loss coefficients are calculated according to the formulations in Eq. (2.23). The experimental deviation is consistently based on the multi-hole traverses. Due to their spatial limitations in the endwall regions however, the calculation of the respective averaged total and static pressures do not represent the entire plane and this restriction is correspondingly considered in the CFD results. Furthermore, the correction scheme following Eq. (3.1) is applied to all traverse measurements.

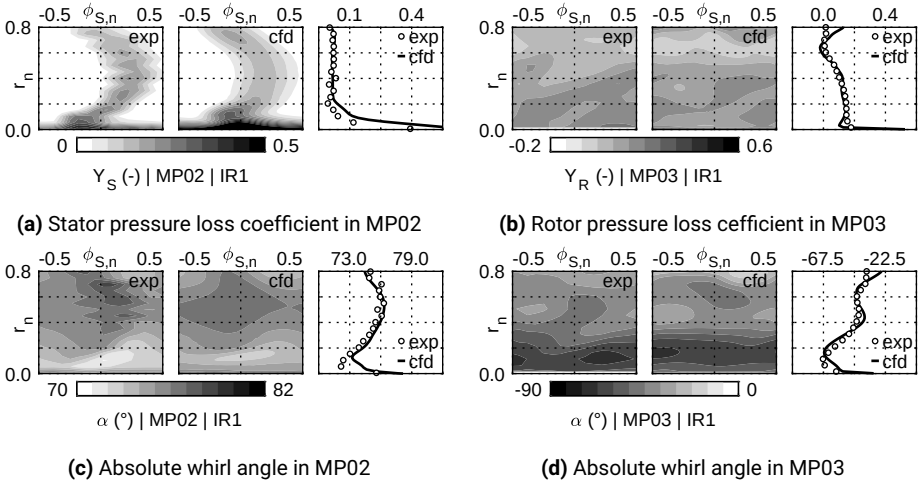

(a) Stator pressure loss coefficient in MP02

(b) Rotor pressure loss cefficient in MP03

(c) Absolute whirl angle in MP02

(d) Absolute whirl angle in MP03

Figure 4.1: CFD-validation in the stationary frame of reference: Experimental data is based on 5HP traverses. For each plane, the pressure loss coefficient Y and the absolute whirl angle α are shown.

Stator Outlet - MP02 - 5HP

With reference to Fig. 4.1a, the overall 2D loss pattern is well reproduced by the CFD. Profile losses are correctly positioned and show good agreement in magnitude. Closer to the hub, the trailing edge shed vortex and the hub passage vortex dominate in both, the 5HP and CFD distribution, where the CFD shows slightly elevated levels. The corresponding pattern in the whirl angle, Fig. 4.1c, also shows general consistency. CFD shows a sudden increase at $r_\mathrm{n} = 0.2$, which is not apparent in the 5HP-data. A final statement for this local deviation is not possible. It is highlighted though, that the location is already strongly affected by the purge flow interaction, which leads to high gradients in the flow field. This is equivalent to a high spatial sensitivity in both, experiment and computation. At $r_\mathrm{n} = 0$, where the circumferential gradients are comparably small, the deviation is cleared out, though. This allows the assumption, that the coarse resolution of the 5HP is missing out some local but dominant flow features at the two previous radial measurement positions.

Rotor Outlet - MP03 - 5HP

In Figs. 4.1b and 4.1d, equivalent views are shown for MP03. According to the stationary frame of reference, the rotor induced circumferential influence is not present in both, the 5HP and CFD. The foundation of the averaging however differs significantly.

While the data from the 5HP are averaged physically due to the high internal pneumatic damping, the CFD is a true mathematical average of the unsteadiness. Without challenging the application of pneumatic probes in highly fluctuating flow regions in general, the practicability should always be questioned. As no reliable assessment of the confidence interval of 5HP measurements in MP03 are available, the following comparison has a strong qualitative character.

In comparison to the observations in the stator exit plane, the 2D gradients in the ϕ-direction are now small. A pure visual comparison of the 2D distributions is therefore hardly possible. A general consistency in the circumferentially averaged quantities however is clearly given. Variance in Y_{R} is primarily present above $r_{\mathrm{n}} = 0.6$, which indicates an overestimation of the pressure losses induced by secondary flow features in the tip region of the blade. This region is not part of the present investigations and therefore assumed acceptable. As the variation of the purge mass flow rate has no effect on the characteristic, a potential error in the numerical model is seen to be systematic. The good agreement in the lower half of the channel is much more important. Both, the increased deflection and the pressure loss magnitude are well captured by the CFD.

A final judgment of the 2D distribution is not possible for a second reason. As introduced in Section 3.2, the blade count of the second stator row is artificially increased from 32 to 36. For the rotor exit plain, this will inevitably influence the flow distribution in the circumferential direction. To summarize, no investigations are conducted on the quantification of the manipulated geometry. There is, however, no indication, that this slight change in the blade count will alter the tempo-spatial characteristic in the rim seal region upstream the rotor.

4.1.2 Unsteady Flow Field Validation

The unrelated time-averaged unsteady pressure traverses, as recorded with UPP1 in MP02i and UPP2 in MP03, are now compared to the corresponding computational data.The measurement grids are limited to the hub side regions and a view to the entire 2D flow field is prohibited. The grids are rather chosen to allow the rim seal purge flow to be investigated in two ways. First, UPP1 in MP02i is capable to experimentally determine the unsteady aerodynamic boundary condition in the rotor inlet area. The measurement points above the stator lip allow the validation of the annulus flow, as it propagates towards the mixing area. The measurement points underneath however allow the investigation of the area of the seal exit. As described in Section 3.1.2, for both probes, the entire set of data is suitable to deduce true flow variables due to the virtual mode operation. In the following however, all data is based solely on the pressure signal of those measurement points, where the probe head is most probably aligned to the mean flow direction.

Unrelated Time-Average - MP02i and MP03

Main purpose of the following comparison is to provide evidence, that the CFD is capable to reproduce the dominating rotor induced pressure fluctuations. Both, the stator-rotor interface and the rotor exit are considered. Confidence is also given to the correct spatial allocation of both, UPP and CFD data sets. Moreover, the comparison is now possible in both coordinate systems, stationary and rotor-relative. With an appropriate data structure, where experimental and computational data is similarly organized, switching between the stator and rotor coordinate systems, $\phi_{\mathrm{S,n}}$ and $\phi_{\mathrm{R,n}}$ respectively, should be straight forward. With the access to a second reliable source of unrelated time-averaged quantities [1]. The evaluation strategy is now presented for the unsteady data in MP02i and MP03. In contrast to the stationary 5HP data, the deviation of a true pressure loss coefficient is not possible due to the lack of total and static pressure averages in the respective measurement plains. To still allow the deviation of meaningful non-dimensional pressure based quantities, an alternative normalized pressure difference is established. The deviation of a representative inlet total pressure average is now based on one of the total pressure rake in MP01. The dynamic head in the respective plane is now replaced by the circumferential velocity of the hub side endwall. While a physical interpretation of the magnitude of this quantity is possible for the stator exit plane, its level at rotor exit incorporates the total pressure drop due to the work delivered by the rotor, making the absolute level difficult to interpret. It is therefore highlighted, that the relative distribution should be considered. In both planes, the local difference then the percentage of a total pressure difference per dynamic head of the rotating endwall.

In Figs. 4.2a and 4.2c, the distribution in MP02i is presented in the respective coordinate systems. The normalized radius is adjusted to the available experimental data, now ranging from -0.2 to 0.4. In the stationary frame of reference, Fig. 4.2a, position and magnitude of the pressure deficit in the main annulus is well captured by the CFD. As the axial position of the plane is right after the end of the stator hub side endwall, the lower region is mainly affected by the rim seal purge flow. Comparing the induced high total pressure deficit agrees surprisingly well. Little spatial deviations in the ϕ direction are considered negligible. Due to the existing high whirl angle in the main flow, a slight misalignment in the axial position of the probe can cause a notable circumferential shift.

The exact same raw data, now averaged in the rotating frame of reference, are shown in Fig. 4.2c. As expected, all stator induced flow patterns are not present anymore. The slight inhomogeneity at $r_{\mathrm{n}} = 0.1/\phi_{\mathrm{R,n}} = 0.7$ however is unusual, as the total pressure is consistently defined in the stationary frame. Eventually, the local elevations must be caused by the upstream effect of the rotor. The potential field alone is no reason as it would just cause a redistribution (with constant total pressure). The elevated total

[1] an experimental source can be a stationary measurement technique such as pneumatic multi-hole probes while stationary CFD results are a possible computational second reference

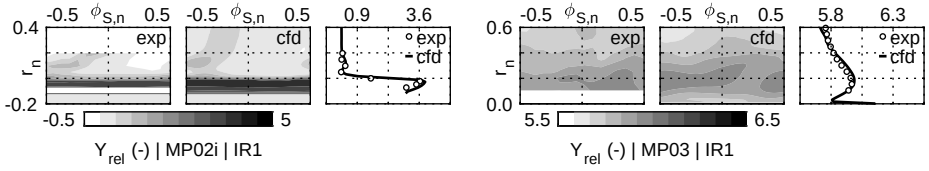

(a) UPP1 and CFD in MP02i: unrelated time-average in the stationary frame of reference

(b) UPP2 and CFD in MP03: unrelated time-average in the stationary frame of reference

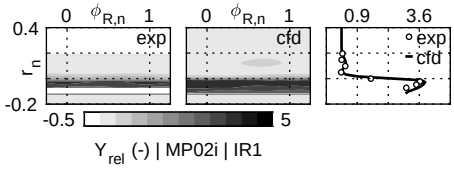

(c) UPP1 and CFD in MP02i: unrelated time-average in the rotating frame of reference

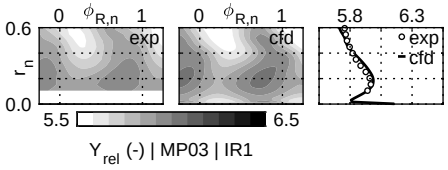

(d) UPP2 and CFD in MP03: unrelated time-average in the rotating frame of reference

Figure 4.2: Two-dimensional validation of unrelated time-averages of the normalized pressure difference in the stationary and rotating frame of reference. Data is based on unsteady pressure probes and CFD

pressure therefore has to be work delivered locally by the leading edge region of the rotor. This phenomenon was recently reported by Gaetani and Persico [21].
Data is now discussed for MP03, compare Figs. 4.2b and 4.2d. With respect to the low gradients in the ϕ-direction, the discussion follows the same arguments, as given in the respective section on the 5HP. However, the now available view of the rotor-relative data allows to verify, if the CFD is capable to predict the circumferential distribution of the rotor induced total pressure characteristic. As can be seen well in Fig. 4.2d, the predicted loss cores in the rotor exit plane are well positioned and distinct. Gradients seem to be slightly higher in the CFD, though. The most obvious motivation is a too little predicted dissipation, which would agree with a commonly discussed issue of Reynolds averaged Navier-Stokes (RANS) models. A second reason could be however lie in the damping effect by the probe structure (stagnation and re-acceleration). The sensor raw signal is solely converted to pressure on the basis of a static calibration. The probes dynamic characteristic is not taken into account at all.

Spatio-Temporal - MP02i and MP03

On the basis of unsteady flow data, when at least available along one spatial coordinate, the spatio-temporal characteristic can be considered in one single 2D chart. Obviously, time and location then are representing the two coordinates. In the present case, where the movement of a blade row is considered, the actual relative position of the

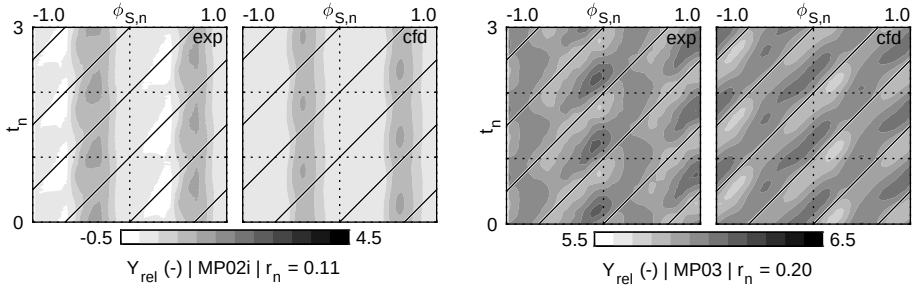

(a) Spatio-temporal validation in MP02i

(b) Spatio-temporal validation in MP03

Figure 4.3: Spatio-temporal validation up- and downstream of the rotating blade row. The space-time characteristic of the relative pressure difference Y_{rel} is shown for $\mathrm{r_n} = 0.11$ in MP02i and $\mathrm{r_n} = 0.20$ in MP03

rotor reasonably depicts the time while the stationary ϕ-coordinate is the location. In contrast to the validation of the unrelated time-averages, as done in the previous section, the spatio-temporal consideration now takes the actual relative position into account.

In Figs. 4.3a and 4.3b, the time-space progression is shown in MP02i and MP03, respectively for one characteristic radial position. Consistent to the presented unrelated time-averages from the previous section, the normalized total pressure difference is depicted. For each individual rotor position, data is now phase-averaged based on the available length of the time-series.

Figure 4.3a presents the results at a normalized radius of $r_{\mathrm{n}} = 0.11$ in MP02i. The abscissa represents the location in the stationary frame of reference and ranges over two full stator pitches. The rotor-relative position is described with its respective normalized time and is limited to three full bypassing events. In conformity to the unrelated time-averages, the first stator dominates in both, the measured and computed progression. The total pressure increase, as generated by the rotating profiles, is primarily visible in the stator wakes and is consistent between UPP1 and CFD.

The situation in the rotor exit plane is depicted in Fig. 4.3b, where now a relative channel height of $r_{\mathrm{n}} = 0.20$ is chosen. The inclined structures are well established, confirming the rotor wake to be dominant. However, stationary features are also distinct. The distribution of stationary and rotating patterns are basically comparable but with significant differences in periodicity. Where the CFD is well periodic with two distinct stationary structures (vertical lines), the UPP2 shows a non-periodic discontinuity between $\phi_{\mathrm{S,n}} = -0.75$ and -0.25 stator pitch. Again, this is probably induced by the second stator, as the measurements are referring to the true situation with 32 vanes.

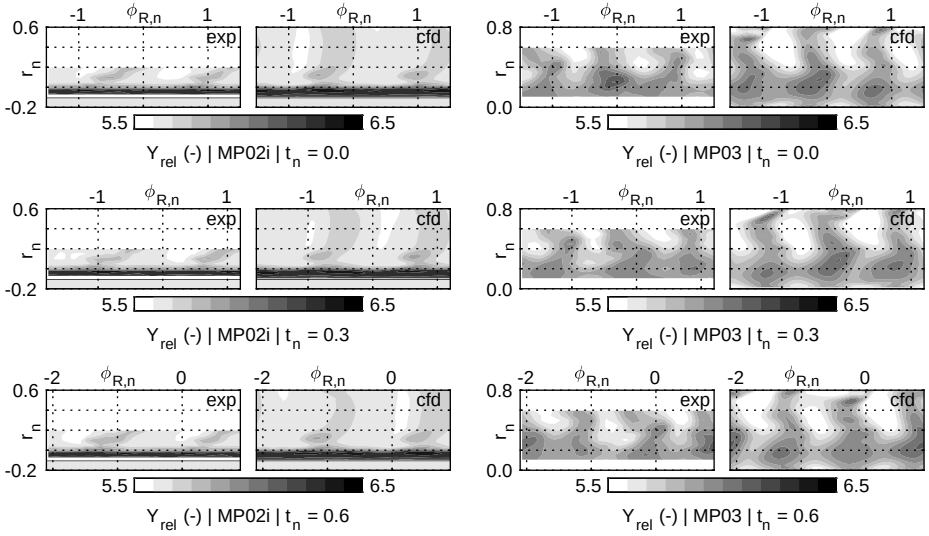

Figure 4.4: Validation of three individual phase-locked situations: The measured phase-locked averages of the normalized pressure difference Y_{rel} are well reproduced by the CFD. The accordance in movement and strength of the pressure loss regions in MP03 is taken as evidence for a correctly computed spatio-temporal interaction inside the rotating blade row.

The validity of the computed spatio-temporal characteristic can further be based on the comparison of individual phase-locked averages. While a purely visually based comparison of such 2D characteristics is of minor value, they are useful for a qualitative judgment of stator-rotor interaction mechanisms. This is especially true, when the individual phase-locked averages are viewed dynamically in repeated sequences. During the development of data processing algorithms for time-resolved flow investigations, the assessment of such phase-locked pictures can be very helpful. This approach of phase-locked visualization is exemplary shown in Fig. 4.4, in which three characteristic phase-locked averages are shown for both investigated planes.

To summarize, the time averaged unsteady CFD is judged valid in the prediction of relevant total pressure characteristics. Certainly, it was not shown, that the trends of the other flow variables are also valid in the time-domain. However, as the identification of the rotating structures is based on the unsteady total pressure signal only, the presented verification of the overall flow field prediction is seen to be adequate at this point.

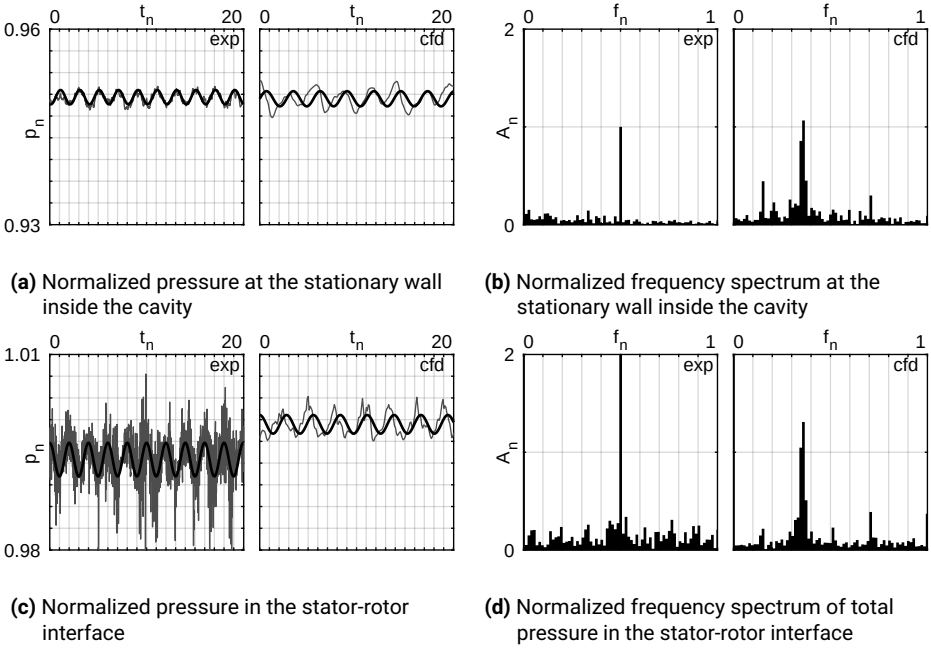

(a) Normalized pressure at the stationary wall inside the cavity

(b) Normalized frequency spectrum at the stationary wall inside the cavity

(c) Normalized pressure in the stator-rotor interface

(d) Normalized frequency spectrum of total pressure in the stator-rotor interface

Figure 4.5: Time-resolved validation based on the true time-series

4.1.3 Time-Series and Detection of Large Scale Rotating Cavity Structures

The experimental and computational unsteady aerodynamic data is now analyzed with a focus on the verification of large scale fluctuations, which are not related to the dominating frequencies. Therefore, the unsteady normalized pressure $p_\mathrm{n} = p/p_1^0$ is evaluated at two distinct locations; first, inside the cavity, taking the position of the wall mounted pressure transducer at $\phi_\mathrm{S,n} = 0$ and second, the unsteady pressure probe in MP02i at $r_\mathrm{n} = 10\,\%$, again at $\phi_\mathrm{S,n} = 0$. The unsteady pressure from inside the cavity is used to prove the existence of a dominating frequency for both, the experimental and computational flow field. In a second step, the analysis of the time-resolved pressure outside the cavity allows to validate the CFD with respect to its ability to correctly predict the unsteady interaction between the rotating pressure fluctuation inside the cavity and the main flow.

In the left chart in Fig. 4.5a, the wall pressure inside the cavity is shown for a period of 20 BPF as the thin gray line at around $p_\mathrm{n} = 0.95$. It is clearly dominated by one specific frequency. The corresponding normalized frequency spectrum in Fig. 4.5b, left, allows it to be identified close to a normalized frequency $f_\mathrm{n} = f/\mathrm{BPF} = 0.5$. When

looking at the pressure signal in the main annulus, the same frequency is dominant, but with much higher noise. The overall higher amplitude is caused by the increased dynamic head in the stator-rotor interface. To visualize the ratio of Cavity Mode (CM) to the particular full signal, the dominating cavity mode with its respective amplitude is again shown as a black line over the raw signal.
The computed unsteady pressure is evaluated and visualized similarly to the experimental data, compare the right charts in the respective figures. The coordinates and the processed length of the time-sequences are equal. Due to the lower temporal resolution of the CFD, the resolution of the frequency spectrum is approximately 20 % compared to the experiment. It is however still five times the BPF, as 10 transient results are available per rotor pitch.
Looking at the time-dependent pressure inside the cavity, obviously the level and unsteady amplitude is well reproduced by the CFD. However, the spectrum differs from the experiment and a dominating frequency band is now identified at around 0.36 BPF. As will be quantified in the next section, this is originated in a different number of rotating lobes and not by the rotational speed of the flow structures. Compared to the experiment, another difference is, that the pressure fluctuations are much less following a clear oscillation with one discrete frequency, which indicates a higher circumferentialö instability inside the cavity. This also gets obvious by comparing the true signal (black) and peak amplitude plot (grey). The characteristic differs from a true sine-function where the pressure gain is smoother than the pressure decrease.
For the signal and frequency spectrum of the total pressure in the annulus, similarly to the experiment, the CFD also predicts an elevated amplitude, when it is compared to the pressure fluctuation inside the cavity. However, the gain is predicted more indistinct. The influence of the rotor is slightly visible whereas the experimental spectrum does not show any increased amplitude at a BPF of 1. To summarize, the computational setup generates rotating pressure fluctuations of similar amplitude but with different characteristic frequencies.

4.1.4 Quantification of Rotating Pressure Fluctuations in the Rim Seal Region

To further investigate the rotational characteristics quantitatively, the signals of all five installed fast response transducers in the cavity are evaluated. Again, a similar procedure is applied to the corresponding data in the CFD results. The applied method is similar to the one presented in Beard et al. [6]. Target of the procedure is to clearly identify the rotational speed and the number of structures rotating within the cavity. The method is based on correlating the pressure information on different circumferential positions. If the structures do not change fundamentally while moving from transducer to the next, each signal will solely be phase-shifted. It is highlighted, that the phase angles could also be directly derived from the individual Fast Fourier Transformation (FFT) and for the presented data this was done to verify the correlation scheme, but has shown not to be as stable as the computation of the cross-correlations.

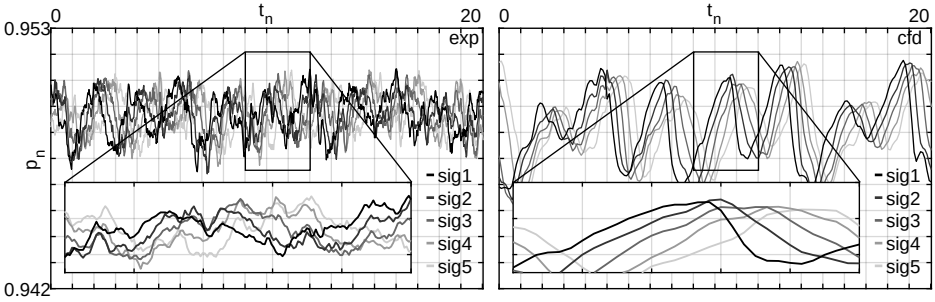

(a) Time series of the normalized pressure at the stationary wall of the seal

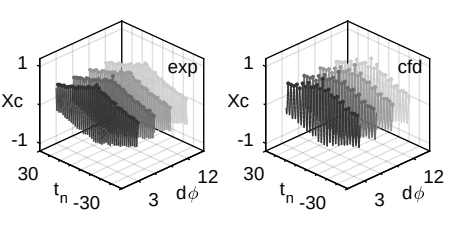

(b) Correlation maps

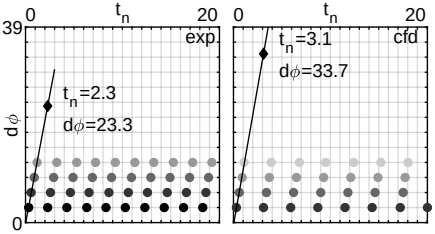

(c) Correlation peaks

Figure 4.6: Validation of the true time-series within the cavity: The procedure allows the characterization of the rotating large scale pressure fluctuations in the rim seal region. The correlation of unsteady pressure information at five different circumferential positions allows the quantification of rotational speed and number of structures.

With reference to the Fig. 4.6a, p_n is now shown for all five sensor positions, again for both, the experiment and computation and the phase-shift is obviously apparent in both charts. The pressure at sensor positions 2 to 5 are cross-correlated to the first one. The results are shown in the 3D correlation maps in Fig. 4.6b, where a $d\phi - t_\mathrm{n} - Xc$ coordinate system is chosen. Determining the local correlation-peaks and applying a scaled reorientation to the $d\phi - t_\mathrm{n}$ plane, the charts in Fig. 4.6c are derived. A linear interpolation over the first four correlation peaks leads to the rotating velocity of the structures and, with simple extrapolation, to the number of lobes over the full-circle. Applying this procedure to the experimental data, the number of rotating structures is close to 18 ($N = 17.8$) revolving slightly above the rotor speed ($\omega_s = 1.04\Omega$). As the rotor counts 36 blades, one structure extends approximately over two blades. The exact same procedure is applied to the computed pressure signal at the corresponding coordinates. As can be seen in Fig. 4.6c, the evaluated number of lobes is very close to 12 ($N = 11.74$), again rotating slightly above the rotor speed ($\omega_s = 1.10\Omega$).

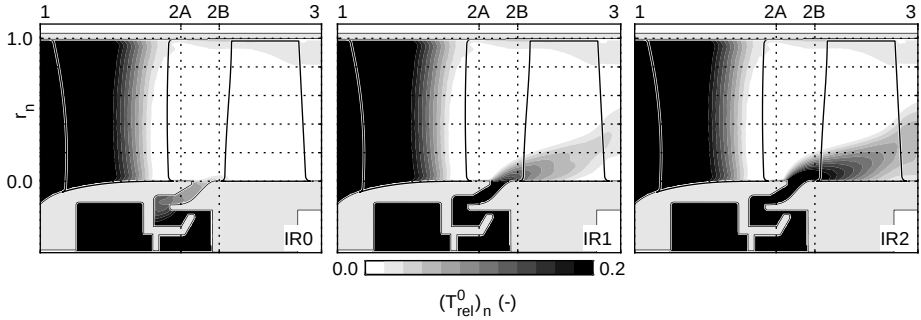

(a) Normalized temperature difference $(T^0_{\mathrm{rel}})_{\mathrm{n}} = (T^0 - T^0_1)/(T^0_{\mathrm{C}} - T^0_1)$

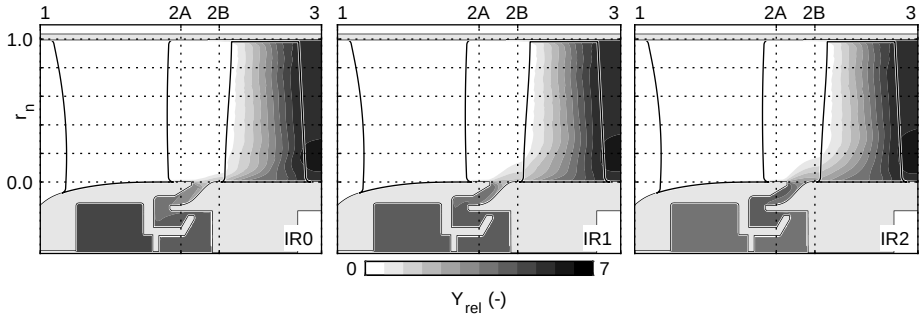

(b) Normalized relative total pressure difference

Figure 4.7: Global influence of the purge mass fraction to the overall stage characteristic showing the circumferential, unrelated time averages of normalized total temperature and pressure difference

4.2 One-Dimensional Stage Characterization

4.2.1 Overall Stage Performance

To introduce the global influence of the varying purge flow mass fraction to the temperature and pressure distribution within the stage, the circumferential average of both, the normalized temperature and pressure differences are depicted in Figs. 4.7a and 4.7b, respectively. The ejection leads to an expected area of increased temperature in the lower half of the rotor passage. For sure, a simple visual comparison of flow quantities has little value. They are however well suited for the overall orientation, especially with respect to the axial positions of the four distinct planes, on which the following 1D stage consideration is based on. Detailed and enlarged views of flow quantities are given at the subsections, where appropriate.

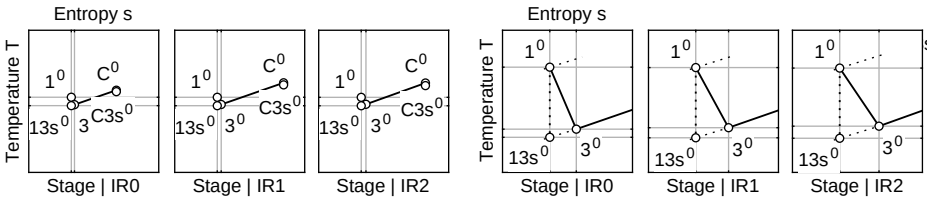

(a) Global stage with cooling

(b) Stage with focus on the main flow

Figure 4.8: Overall view on the one-dimensional T-s characteristic for the three investigated purge flow mass fractions

With the framework, as introduced in Section 2.2.2, the stage is first quantified implicitly, accounting only for the thermodynamic properties at the inlets of main and secondary flow, states 1 and C, as well as the common outlet at the stage exit, state 3. The actual stage work extracted from the fluid is defined by the sum of the enthalpy difference of main and purge flow between their individual inlets and the common outlet, compare Eq. (2.34). To visualize the entire expansion paths, the corresponding T-s diagrams are drawn and shown in Fig. 4.8a. As the total temperature drop over the stage is of similar magnitude compared to the difference between main and purge flow, the entire T-s scope is not suitable for a detailed stage investigation. In the following, the axis intercepts are therefore adjusted to the annulus flow, and where appropriate, to the area of interest. As demonstrated in Fig. 4.8b, the thermodynamic path of the purge flow is then mostly excluded. Recalling the thermodynamic path in a real engine or gas turbine, a configuration with an elevated *cooling* temperature is anyhow highly conceptual. However, non of the assumptions, as taken in the different approaches of judging a cooled turbine stage globally, are violated.

To summarize the trend of the variation in ψ, its effect on the stage parameters is first presented on a global scope. The framework for the consideration of cooling flows from Section 2.2.2 comes along with the key question, of how to quantify the mixing in the ideal expansion. With a view to the T-s diagrams in Fig. 4.8b, the step-wise increase of purge flow elevates both the total temperature T_3^0 and the specific entropy s_3 at the turbine exit. Following the formulations for the cooled turbine, Eq. (2.34), the individual shares of main and purge flow are summed up to quantify the effective power of the stage. As specified in Table 4.1, the normalized total power of the stage $\widetilde{P}_{\mathrm{St}}$ decreases with raising ψ. In agreement to the trend of the total temperature difference $T_1^0 - T_3^0$ in Fig. 4.8b, the power delivered by the main-flow decreases remarkably, while the rest is compensated by the purge flow.

With the definition of the ideally achievable work after Hartsel, the concept of the individual expansion to the exit pressure leads to the particular situation, that the purge flow has virtually no share on the stage work. The true thermodynamic path of

Variable	Description	IR0	IR1	IR2	Unit
ψ	true mass fraction	-0.057	0.922	1.900	%
$\widetilde{P}_{\mathrm{St}}$	stage power	-5.227	-5.217	-5.189	K
$\widetilde{P}_{(1-3)}$	main power	-5.233	-5.076	-4.904	K
$\widetilde{P}_{(\mathrm{C}-3)})$	purge power	0.006	-0.141	-0.285	K
$\widetilde{P}_{(1-13\mathrm{s})}$	id. main power	-5.920	-5.927	-5.924	K
$\widetilde{P}_{(\mathrm{C}-\mathrm{C}3\mathrm{s})}$	id. purge power	0.001	-0.014	-0.035	K
$\widetilde{P}_{\mathrm{St,s,H}}$	id. stage power Hartsel	-5.920	-5.941	-5.959	K
$\widetilde{P}_{\mathrm{St,s,FR}}$	id. stage power FR	-5.923	-5.889	-5.853	K
$\widetilde{P}_{\mathrm{St,s,MP}}$	id. stage power MP	-5.920	-5.929	-5.927	K
$\widetilde{P}_{\mathrm{St,s,WP}}$	id. stage power WP	-5.923	-5.888	-5.851	K
$\eta_{\mathrm{St,s,H}}$	stage efficiency Hartsel	88.30	87.82	87.09	%
$\eta_{\mathrm{St,s,FR}}$	stage efficiency fr	88.25	88.58	88.65	%
$\eta_{\mathrm{St,s,MP}}$	stage efficiency mp	88.29	87.99	87.55	%
$\eta_{\mathrm{St,s,WP}}$	stage efficiency wp	88.25	88.60	88.70	%

Table 4.1: Influence of the purge flow mass fraction to the overall stage performance parameters

the purge flow from C to 3 is not considered at all, as the mixing is neglected entirely. On the other hand, the ideal work of the main flow is overrated, again because of leaving out the mixing. The stage efficiency after Hartsel, $\eta_{\mathrm{St,s,H}}$, is therefore largely based on the ideal expansion of the main-flow, which is close to constant for all three operating conditions.

The reasoning of the necessity for alternative stage efficiencies with the ideal process being based on a preceding virtual mixing is justified without a question. The stage is now evaluated with the three alternative formulations derived in Section 2.2.2. In Fig. 4.9, the thermodynamic states are depicted. The virtual ideal inlet temperature is identical for all three assumptions and the differences in the efficiencies finally arises only based on the entropy after mixing. The difference between FR (fully reversible) and WP (weighted pressure) is marginal, however shown for the sake of completeness. In the following, the discussion of the apparent differences between FR and MP is therefore sufficient.

Due to the total pressure ratio of the inlet states of main and purge flow, the relative arrangement of the ideal inlet states may appear confusing. Where the theory, applied to the cycle analysis, leads to FR being the process with the lowest amount of unavoidable entropy, the present configuration leads to a situation the other way around. Considering the fact, that the total pressure at the main inlet is higher than the one derived for the purge flow, the MP has a thermodynamical state after mixing, which is beneficial compared to a fully reversible. In any case however, the basic idea of

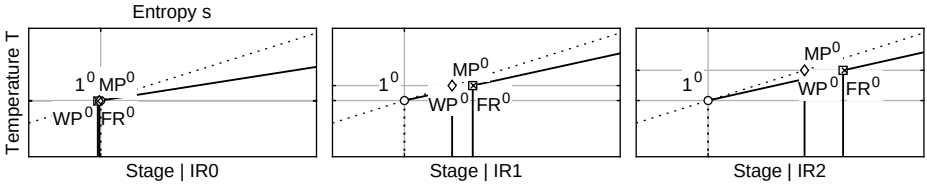

(a) Thermodynamic states at the inlet of the ideal mixing process

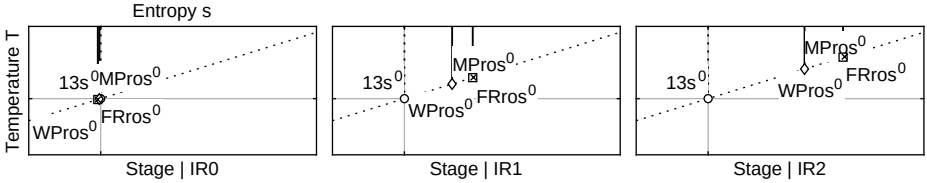

(b) Thermodynamic states at the outlet of the ideal mixing process

Figure 4.9: Ideal reference processes of the alternative efficiency ratings for the investigated purge flow variation

considering losses which are induced by the pressure equalization, if seen as avoidable or not, is evidently a good idea.

In Table 3.1, the consequences to the overall stage efficiencies are brought together. For the case without purge flow, all definitions lead to a comparable efficiency of slightly above 88.2 %. For both cases with injection, the formulation after Hartsel shows the highest sensitivity, which is the result of the unaltered level of ideal stage power. A closer look to the fully reversible definition highlights, that excluding unavoidable entropy production from the reference process, the cooled turbine efficiency may show the opposite trend. For the case of the fully reversible process, the stage efficiency raises from 88.25 % without mixing to 88.65 % for the IR2 configuration. Excluding only the entropy induced by the temperature equalization, the stage efficiency decreases from 88.29 % to 87.55 % though, however still less than predicted with the Hartsel definition.

For a cooling flow variation in the range of 2 %, a difference in stage efficiency of almost 1.6 % may not be disregarded. As referenced in Eq. (2.34), the total amount of cooling flow fractions is more in the range of 20 %, then quickly leading to differences in stage efficiency of several percentage points. With the separate ideal expansion of main and cooling flows, there is not only the risk to misjudge the overall performance of the stage but also disregarding the advantages of a quantified and evaluated mixing process, based on the second law of thermodynamics. The formulation of the method to the entire cooled stage, as introduced so far, is by far not the application of the expanded cooled efficiency definitions. The adaption of the method to a single blade

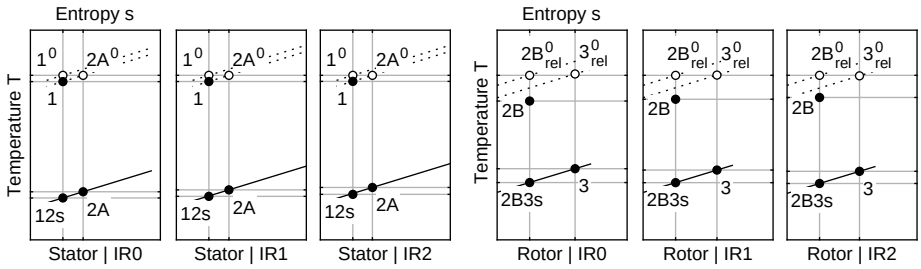

(a) Thermodynamic states of stator in- and outlet

(b) Thermodynamic states of rotor in- and outlet

Figure 4.10: T-s diagrams for the individual rating blade row rating

row will be presented for the rotor. Before however, the stator and rotor rows are considered individually with excluded purge flow ingestion.

4.2.2 Blade Row Performance Excluding the Mixing Zone

The stator and rotor blade rows can be considered individually, where only the goodness of the respective acceleration is rated. This is done on the basis of the formulations for the efficiencies and loss coefficients, as introduced in 2.2.1. First, the stator is balanced between 1 and $2\mathrm{A}$. Figure 4.10a represents the corresponding thermodynamic states in the T-s diagram. Excluding the purge flow area from the enthalpy and pressure balances reflects the actual stator performance, taking into account the global variation in the operating conditions.

Both total-to-static and static-to-static stator efficiencies are hardly influenced by the variation of ψ. Referencing Table 4.2, the ratio between both efficiency definitions stays constant, which is a further indication for a consistent stator performance. The slight decrease in the absolute mass-flow in fact changes the total to static ratio, however only by 0.01 % which is seen to be insignificant. The same argumentation is assumed valid for the slight variations in the enthalpy and pressure loss coefficients.

The rotor performance is now considered on the same line of argumentation, where the relative thermodynamic quantities are balanced from $2\mathrm{B}$ to 3. Both efficiency definitions react remarkably positive to higher ψ. $\eta_{\mathrm{R}_{SS}}$ increases almost by 2 %, which indicates the highest sensitivity of all blade row performance parameters with respect to a change in ψ. The trend is mirrored by the total-to-static efficiency, however with lower absolute changes, which is generally motivated in choosing the total state as reference.

Similar to the stator, the ratio between the two rotor efficiencies is now rated. The increase of the static-to-static efficiency is obviously higher than the corresponding

Variable	Description	IR0	IR1	IR2	Unit
$\eta_{\mathrm{S}_{SS}}$	static to static - stator	94.71	94.66	94.67	%
$\eta_{\mathrm{S}_{TS}}$	total to static - stator	94.98	94.93	94.95	%
$\eta_{\mathrm{S}_{SS}}/\eta_{\mathrm{S}_{TS}}$	efficiency ratio stator	99.72	99.71	99.71	%
ζ_{S}	enthalpy loss coeff - stator	5.02	5.07	5.05	%
Y_{S}	pressure loss coeff - stator	5.46	5.50	5.48	%
$\eta_{\mathrm{R}_{SS}}$	static to static - rotor	83.01	84.89	85.86	%
$\eta_{\mathrm{R}_{TS}}$	total to static - rotor	87.08	88.25	88.75	%
$\eta_{\mathrm{R}_{SS}}/\eta_{\mathrm{R}_{TS}}$	efficiency ratio rotor	95.32	96.18	96.74	%
ζ_{R}	enthalpy loss coeff - rotor	12.76	11.72	11.30	%
Y_{R}	pressure loss coeff - rotor	13.44	13.24	13.50	%

Table 4.2: Influence of the purge flow mass fraction to the individual blade row performance parameters

total-to-static. Solely based on the 1D consideration, a meaningful explanation is not possible. Interestingly, the pressure loss coefficient does not follow the global trend of the other performance parameters. It first decreases from IR0 to IR1 to then raise from IR1 to IR2. For the divergence of the two loss coefficients, there is no final conclusion given here. It is however highlighted, that the pressure loss is referred to the actual exit state, while the enthalpy based formulation is accounting for the ideal expansion beginning at the rotor relative inlet. Therefore, an increase of the total enthalpy, which is possibly induced by the casing endwall, is not accounted for. Evaluating the individual differences of the rotor relative total enthalpy in fact indicate a dependency on the actual ψ. Without purge flow present, a marginal gain is observed. When introducing purge flow, it is then decreased step-wise, being close to zero for IR1 and negative for IR2. As mentioned earlier, the exact underlying mechanism is unknown. To conclude, the rating of a blade row performance solely based on a pressure loss is disadvantageous. It again highlights the importance of considering energy and entropy based loss formulations, where ever possible.

4.2.3 Rotor Performance with Seal

The basic idea of considering cooling flows for the overall stage performance evaluation is now adapted to the rotor, where the section with the rim seal is virtually seen as part of the row. The main-flow is now rated from the stator outlet $2\mathrm{A}$ to 3. Simultaneously, the purge flow is balanced from its inlet C to the rotor exit 3. The inlet states are quoted in the rotating frame of reference. In the following, two blade row efficiencies are defined and evaluated. The first one is equivalent to the definition of Hartsel, where main and purge flow follow an ideal acceleration from their individual total relative states to the common static pressure at the exit. The second formulation, a

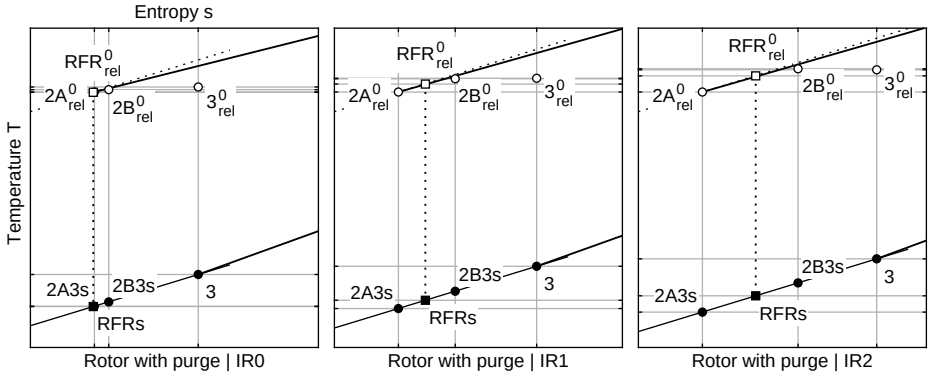

Figure 4.11: Ideal reference processes of the alternative efficiency ratings of the rotor with rim seal

total-to-static blade row representation of $\eta_{\mathrm{St,FR}}$, where a fully reversible mixing is assumed to take place before again an ideal total-to-static difference to the rotor exit is rated.

The corresponding thermodynamics are again drawn to individual T-s charts, depicted in Fig. 4.11. Even if not included in the energy and entropy balances, the state $2\mathrm{B}$ is included to the charts, which allows a good visual comparison to the rotor rating without cooling, as depicted in Fig. 4.10b. As becomes clear from the chart for IR0, the situation without purge flow comes along with a slight increase of both, entropy and relative total temperature, when considering the path from $2\mathrm{A}$ to $2\mathrm{B}$. Following the first law of thermodynamics, the total temperature can only raise by an exchange of work or heat, if the assumption of zero purge flow is true. With reference to the corresponding global T-s diagram, the temperature at the cavity inlet is indeed much higher than the main-flow, compare Fig. 4.8a.

As the computational inlet boundary condition is however only defined as an integral value for zero mass-flow and the boundary is not blocked by an adiabatic wall, it turns out, that the flow inside the sub-cavity is indeed moving, which then allows heat to be added at the cavity inlet. It then partially communicates with the main annulus. A correction scheme for the present case is thinkable, in which a two-dimensional, radial plane is used to estimate the true heat flux.

The main effect for the increase in total temperature however is indeed work, which is delivered by the virtually rotating endwalls of the stationary structure. Between $2\mathrm{A}$ and 3, there are first the short endwall sections of the main annulus. The much larger surface-to-fluid interface however is given by the stationary side of the internal seal geometry. The general aerodynamic equivalent is the rotating annular gap, where a considerable amount of energy can be transferred by the near-wall shear layers. The

Variable	Description	IR0	IR1	IR2	Unit
$\eta_{\mathrm{R,H}}$	row efficiency - Hartsel	85.01	84.33	83.30	%
$\eta_{\mathrm{R,FR}}$	row efficiency - FR	85.03	84.28	83.19	%

Table 4.3: Influence of varying purge flow mass fraction to the combined efficiency rating of seal and rotor blade row

overall entropy increase between $\mathrm{2A}$ and $\mathrm{2B}$ is finally superimposed by losses induced by friction. Considering the corresponding states with purge flow, IR1 and IR2, the effect is confirmed. They both show a further increase in the relative total temperature after purge flow is added in the ideal mixing process, see the respective states RFR and $\mathrm{2B}$.

Compared to the rotor blade row consideration in Section 4.2.2, where the mixing zone is excluded, the total-to-static efficiency drops from 87 % to 85 % for IR0, see Table 4.3. The isentropic references of both definitions are identical. The main flow is now rated from $\mathrm{2A}^0_{\mathrm{rel}}$ to $\mathrm{2A3s}$, instead of $\mathrm{2B}^0_{\mathrm{rel}}$ to $\mathrm{2B3s}$, where the change is comparable small, because $\mathrm{2B}^0_{\mathrm{rel}}$ to $\mathrm{2A}^0_{\mathrm{rel}}$ is close to isobaric. Therefore, the change in blade efficiency has to be related to the quantification of the actual achieved total-to-static difference, which is only changed at its inlet, as the reference is in any case 3. Following the argumentation of the work induced by the shear layers, the question arises, if it should be included into the performance rating of the cooled configuration. This however depends on the research intention and is finally defined by the boundary definition of the problem. For the present case, the radial position of the purge flow inlet to the control volume is positioned short underneath the seal. This approach is motivated by the intention to incorporate the aero-thermal flow physics inside the seal, while excluding disc pumping effects from the sub cavity. It is then the frameworks formulation, which allows the flow mechanical breakdown of the differently involved processes.

With another look to Table 4.3, the efficiencies of IR1 and IR2 are almost unaffected with respect to the efficiency definition. As the total relative pressures at $\mathrm{2A}$ and C are very close, ideal mixing RFR does only show a minor effect when compared to the individual rating of main and purge flow. The main advantage of the alternative rating however holds. Only the explicit formulation of a thermodynamically sound ideal mixing process enables an objective judgment of the aero-thermal performance of a cooled stage or blade row.

To link the capabilities of the 1D framework to the results, the individual thermodynamic relation between states $\mathrm{2A}$, $\mathrm{2B}$ and 3 is now considered enlarged in the T-s diagrams, depicted in Fig. 4.12. In the scope of this work, the discussion is limited to a qualitative character. The relative positions of RFR represents the unavoidable entropy production coming along with the thermal equilibration of main and purge flow. Referencing Eq. (2.9), the margin for a potential optimization of the purge flow

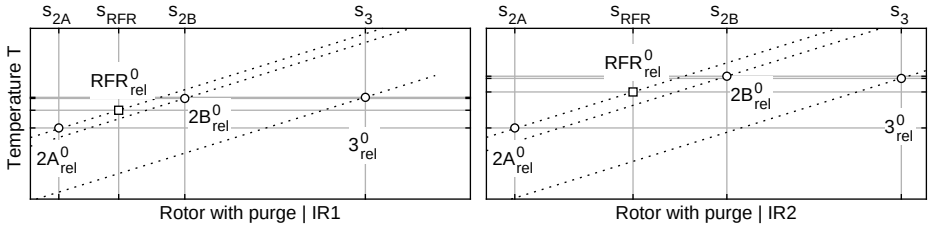

Figure 4.12: T-s diagram of the rotor including the rim seal purge flow injection

configuration is therefore limited to the entropy production $\Delta s = s_3 - s_{\mathrm{RFR}}$. As mentioned before, the control volume boundaries include the seal itself, in which the wall shear leads to the increase in total temperature. As highlighted in the introduction of potential rim seal optimization strategies, Section 1.3, it is primarily the complex interaction of stationary and rotating flow features, which are responsible for the spatio-temporal character of the aero-thermal boundary condition in the seal region. An optimization strategy of the hub side purge flow system though needs to at least consider the thermodynamic path, as taken into account in this section. In the setup of a feasible automatic optimization approach, results can be first rated with 1D parameters, where the energy and entropy based ideal mixing between main and purge flow is included.

4.3 Spatio-Temporal Considerations

4.3.1 Phase-Locked Time Average

The 3D distribution of the identified vortical structures is now considered phase-locked for $t_{\mathrm{n}} = 0$. Referencing Fig. 4.13, the phase-locked average allows a robust assignment of the stator outlet vortical structures and their positioning in the rotating frame of reference. Comparing the circumferential distribution of $\omega_{\mathrm{SW,n}}$ in Fig. 4.13b with the back view in Fig. 2.10b, the dominance of the TESV in conjunction with the stator passage vortex is clearly identified. With their highest magnitudes at around $\mathrm{r_n} = 0.2$ and 0.3, respectively, they are inducing the bands of positive and negative vorticity, as detected in the unrelated time-averaged consideration.
Their impact and convection scheme inside the rotor passages can be brought into line taking the phase-locked planar views, as depicted in Fig. 4.15. It is highlighted again, that a phase-locked average is suitable to derive general spatial interrelations of stator and rotor vortex structures. It may however not be misused for any *tracking* approach, as it still only represents one single flow situation at one instant of time [2].
Based on Fig. 4.15, the general stator-rotor interaction is now derived. In the considered

[2] which is the natural consequence of an Eulerian flow field specification

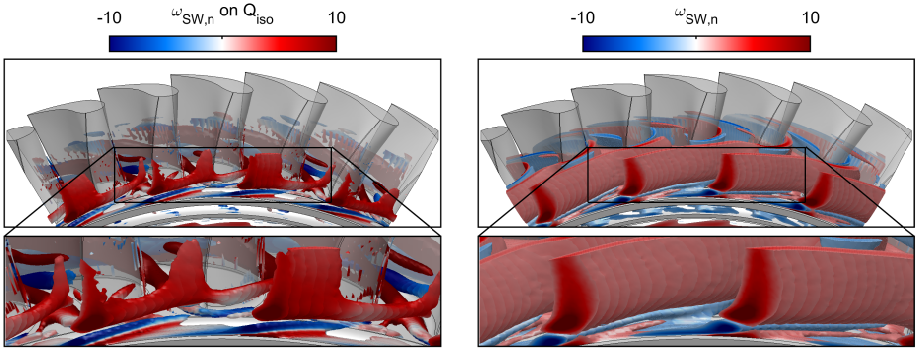

(a) Normalized stream-wise vorticity $\omega_{\mathrm{SW,n}}$ on iso-surfaces of $Q = 1 \times 10^5$

(b) Iso-surfaces of normalized stream-wise vorticity with $\omega_{\mathrm{SW,n}} = [-2,\ 2]$

Figure 4.13: Three-dimensional front view of the secondary flow pattern in the rotor passage: images are based on the phase-locked averaged CFD.

ϕ_{R} range, their are two stator outlet flow patterns interacting with three blades. The actual phase-locked position with $t_{\mathrm{n}} = 0$, where stationary and rotating coordinate systems are aligned, the leading edge of the blade at $\phi_{\mathrm{R,n}} = -1$ is located in a trailing edge pattern. Referencing the view in the right hand side of Fig. 4.15a, the orientation of the blades at $\phi_{\mathrm{R,n}} = 0$ and -1 is clearly represented. While the blade in the middle is influenced by the stator main flow, the blade at $\phi_{\mathrm{R,n}} = 1$ is located short after bypassing the second trailing edge structure, which is convecting towards the pressure side.

Compared to the unrelated time-average, the roll-up of the HV is nearly unaltered. The influence to the near wall flow is then increased further downstream, where a passage-to-passage comparison shows large deviations in the vorticity pattern. While the counter-rotating stator PV is attenuated on its way towards the rotor leading edge region, the respective TESV can be traced in a large portion of the passage, the propagation however depends on which passage is considered. Where apparent though, it is accompanied by counter-rotating flow, which is located radially inwards and a comparison with the unrelated averaged vorticity distribution suggests, that it must be connected to the stator passage vortex.

The governing mechanism between $z_{\mathrm{R,n}} = -0.6$ to -0.1 is complex, as it incorporates the full pattern of the 3D interaction of the stator exit flow with that one from the outer part of the seal. In accordance to the localization of the stationary and rotating structures at $r_{\mathrm{n}} = 0.20$, Fig. 4.15a, a similar pattern is identified in the main annulus, compare $z_{\mathrm{R,n}} = -0.43$ in Fig. 4.15b. Here, a pattern of three regions with negative vorticity emerges. They athen converge with the two stator PV and the lower part of

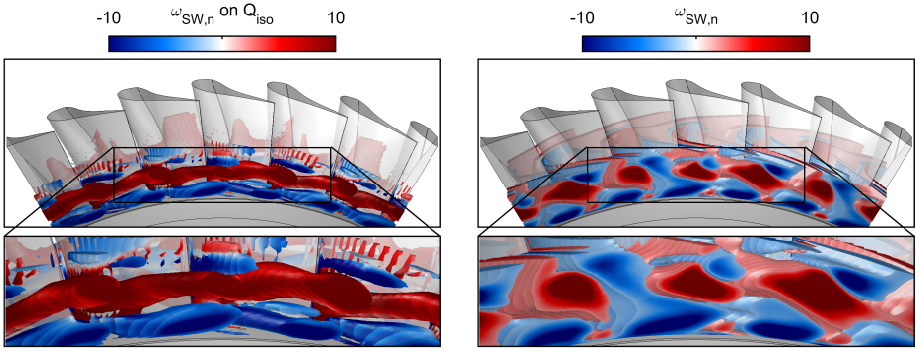

(a) Normalized stream-wise vorticity $\omega_{\mathrm{SW,n}}$ on iso-surfaces of $Q = 1 \times 10^5$

(b) Iso-surfaces of normalized stream-wise vorticity with $\omega_{\mathrm{SW,n}} = [-2,\ 2]$

Figure 4.14: Three-dimensional back view of the secondary flow pattern in the rotor passage: images are based on the phase-locked averaged CFD.

the TESV. This clash of vortical structures with different rates of rotation is of intense complexity. Besides the local vorticity distribution, the overall flow characteristic of stator exit and seal flow diverge considerably in magnitude and direction.

The location of convergence is assumed to be pivotal for the entire near wall flow field of the rotor passage. While only noticed slightly at $\mathrm{z_{R,n}} = -0.27$, the flow region with initially high negative vorticity is releasing its strength of rotation. As a negative stream-wise vorticity has theoretically a negative ϕ-component at its outer bounding, this assumption agrees well with the overall positive ϕ-component of the emerging stator exit flow. With a stator PV-TESV-combination being present however, the attenuation is periodically altered. With the TESV having a positive vorticity, it is enforced by the two radially adjacent, counter-rotating vortices. Emerging the rotor passages, the vortex pattern is finally chopped to meet its circumferential periodicity.

Inside the rotor passage, the seal-stator vortex pattern then encounters the rotor HV, which is developed similarly at every leading edge. The further progress then depends on the respective share of the stator related flow pattern. Depending on the phase-angle, a single rotor will receive a full pattern at its opening, its leading edge or somewhere in between. The different propagation is now introduced for the two rotor passages, which are entirely visible (left: $-1 < \phi_{\mathrm{R,n}} < 0$) and (right: $0 < \phi_{\mathrm{R,n}} < 1$).

For the left passage, the stationary pattern enters close to the suction side. Radially, the center of the TESV is constantly at around $\mathrm{r_n} = 0.2$ and does not generally change its overall location or shape. The counter-rotating fluid underneath however is changing from the transition between suction side and endwall towards the pressure side, virtually passing over the rotor PV, which is by its own moving to the suction side,

where it is finally merging with the stator TESV. The combination of both leaves the passage together, now at a circumferential location $\phi_{\mathrm{R,n}} = 1.2$ at $\mathrm{z_{R,n}} = 0.92$.
Looking at the passage to the right, the same pattern has generally a weaker appearance, where the portion with negative vorticity quickly disappears. At the exit, $\phi_{\mathrm{R,n}} = -1$ at $\mathrm{z_{R,n}} = 0.92$, no flow with a distinct negative vorticity is present, while the overall suction side already developed the TESV. The third rotor passage, which is mainly supplied with stator main flow, shows most likely the development of a classical secondary flow pattern.

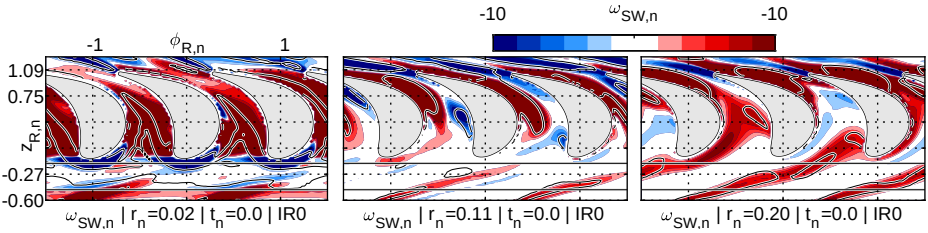

(a) Rotor hub side vortex system in three $\mathrm{r_n}$ planes, phase-locked time average

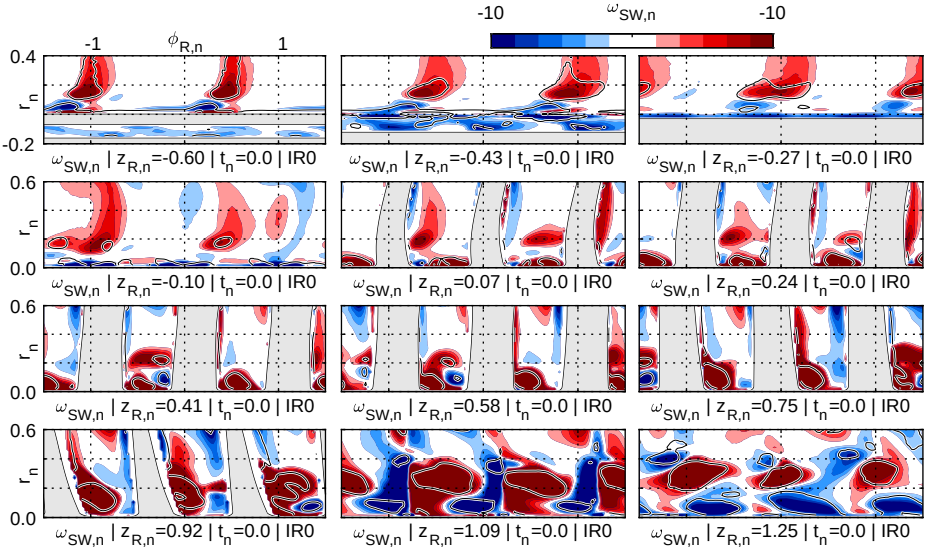

(b) Rotor hub side vortex system in twelve $\mathrm{z_{R,n}}$ planes, phase-locked time average

Figure 4.15: Contours of $(\omega_{\mathrm{SW,n}})_{\mathrm{iso}}$ together with iso lines of Q rotor

4.3.2 Three-Dimensional, Instantaneous Aero-Thermal Flow Situation

In this work, a sound interpretation of the instantaneous, aero-thermal, spatio-temporal character of the flow situation at the rotor hub side is unfortunately out of reach. Nonetheless, the aero-thermal effect of a bypassing cavity structure is depicted exemplary for two selected but characteristic instances. Based on the CFD results for a purge flow mass fraction of 1 %, a qualitative comparison between the phase-locked averaged and instantaneous aero-thermal patterns is presented in Fig. 4.16.
The phase-locked vortex distribution in Fig. 4.16a, which is the equivalent image to Fig. 4.13a, leads to a generally homogeneous ejection pattern inside the seal, as visualized in the corresponding normalized relative total temperature distribution in Fig. 4.16b. For a potential judgment of this specific stage-seal combination, the sealing performance could now be rated satisfactorily. A further investigation of the corresponding instantaneous phase-locked instances now however allows to uncover highest inhomogeneities actually apparent in the true spatio-temporal distribution of the purge flow.
With reference to Figs. 4.16c to 4.16f, the aero-thermal effect of the rotating purge flow patterns is impressively dominant. While the overall purge flow distribution is hard to be identified on the vortex pattern alone, Figs. 4.16c and 4.16e, a look to the corresponding flow temperatures however reveals strongest circumferential inhomogeneities. As quantified in Section 4.1.4, the pressure pattern inside the seal has two lobes (per investigated sector) and rotates slightly above the rotor angular speed with $\omega_s = 1.10\Omega$.
At least qualitatively, the ejection pattern correlates well with the detected pressure fluctuations. Between the two instances considered here ($t_\mathrm{n} = 0$ and 36), the rotor has fulfilled one full revolution and the rotating pattern should, at least statistically, moved between three and four rotor pitches, which is obviously true for the instantaneous global character of the ejected purge flow.
Qualitatively, this observation first of all highlights, that the locally identified rotating pressure fluctuations inside the seal can potentially dominate the aero-thermal flow character in the entire rotor passage, with a focus to the hub side endwall region. For the presented case, the instantaneous redistribution of purge flow leads to rotor endwall segments, which are periodically exposed entirely to the main flow.
To systematically avoid these undesired aero-thermal flow characteristics, new stage-seal designs must be investigated in such a way, that potential rotating rim seal patterns can develop and that their aero-thermal influence can be quantified. This is true for both, experimental and numerical setups, and a framework to to so is presented in this work.

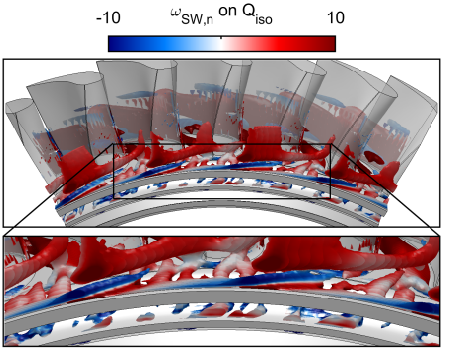

(a) Phase-locked $\omega_{\mathrm{SW,n}}$ at $t_{\mathrm{n}} = 0$

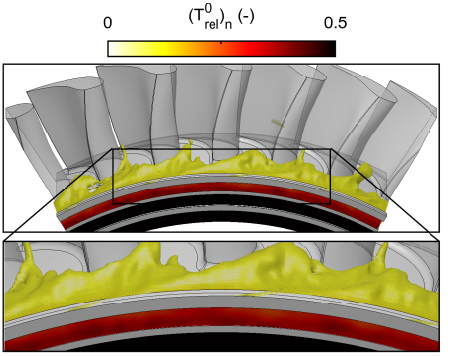

(b) Phase-locked $(T^0_{\mathrm{rel}})_{\mathrm{n}} = 0.1$ at $t_{\mathrm{n}} = 0$

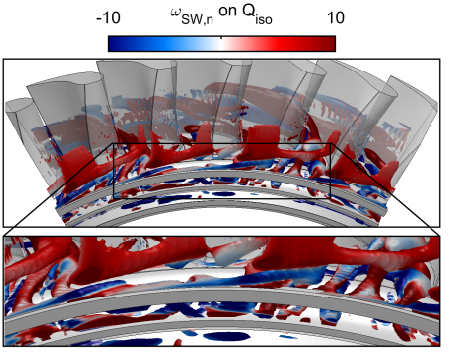

(c) Instantaneous $\omega_{\mathrm{SW,n}}$ at $t_{\mathrm{n}} = 0$

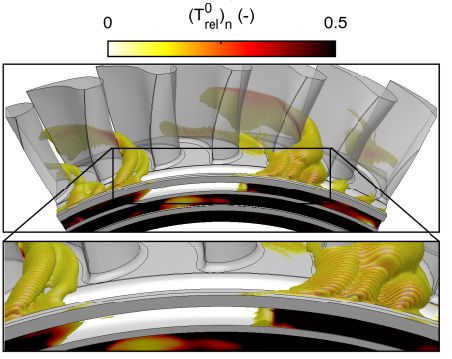

(d) Instantaneous $(T^0_{\mathrm{rel}})_{\mathrm{n}} = 0.1$ at $t_{\mathrm{n}} = 0$

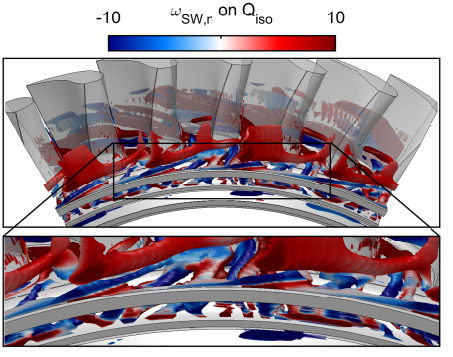

(e) Instantaneous $\omega_{\mathrm{SW,n}}$ at $t_{\mathrm{n}} = 36$

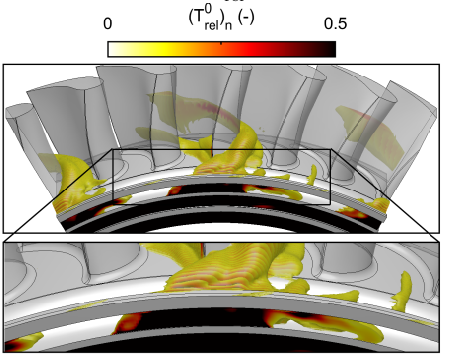

(f) Instantaneous $(T^0_{\mathrm{rel}})_{\mathrm{n}} = 0.1$ at $t_{\mathrm{n}} = 36$

Figure 4.16: Comparison of phase-locked averaged and corresponding phase-locked instances of the three-dimensional aero-thermal flow character in the seal region

5 Conclusion and Outlook

5.1 Conclusion

The tested turbine stage has a scaled seal geometry between stator and rotor, which is connected to a secondary air supply system. The temperature and mass flow of both, the main flow and secondary air, can be controlled independently, allowing the investigation of aerodynamic and thermal performance parameters, which are influenced by the purge flow injection. The possible depth of investigation is incredibly large, ranging from one-dimensional, time-averaged global stage ratings to the very detailed survey of the tempo-spatial characterization of individual vortices.
As a large scale, low-speed environment does not represent the influence of compressibility, it is not applicable for the deviation of absolute performance parameters of engine relevant turbine components. Therefore, such kind of investigation can not be the main objective of this work. Where the rig is perfectly suited for, though, is the development of evaluation approaches, including the corresponding data processing procedures. With this perspective in mind, the main objective of the present dissertation can be clearly positioned in the methods development. Throughout this work, the thematic link to the aero-thermal phenomena is tried to be constantly held, the main attempt however is to present the overall framework.
Individually considered, both unsteady experiments as well as numerical unsteady computations in turbo-machinery research, are a challenging task. This is especially true for the detailed investigation or the optimization of a sub-component, where the requirement on the absolute uncertainty is nowadays on a very high level. To remember, for the further optimization of a rim seal-rotor blade combination, possible improvements can be in the range of a few tenths of a percent. The general requirements on high absolute accuracies also points in the same direction for the experimental and numerical approach. It is, in most cases, coming along with a higher demand of resources. For the realistic representation of a purge flow system, including the potential rotating instabilities, the consequences are highlighted more then once (full circle, rotating, unsteady). Where the complexity is triggered by high fidelity, the amount of data is, too.
Representing a general challenge of our time, the shear amount of data, which is generated in the design and optimization of turbo-machinery, need to be handled. As exemplified for a state-of-the-art, hypothetical optimization strategy, the rating of a single variant is not limited to one-dimensional performance parameters, even if the data is massively down-sampled. If the spatio-temporal character of the physical problem is well-considered in the data reduction procedure, the governing mechanism can be preserved entirely. The fundamental question is, how to define the reduction factor of the individual coordinates (of the problem). The process of data reduction, evaluation, validation and presentation, as presented in this work, was formed iteratively. Without an analytical narrowing of the problem (in the present work the thermodynamically

sound description of the cooled turbine), the valuation of a potential data reduction approach is impossible, as the choice of the performance indicators would be random. Beside the analytical framework, appropriate test data is the key. Without having highly resolved reference data, the reduction procedure can not be valuated. This is highlighted in the comparison of the different time-averages and the choice of the frame of reference. Without the three-dimensional, unsteady computational results, the loss of information, coming along with the respective averaging method, could not be evaluated.

5.2 Summary and Key Findings

Conclusion to the Experimental Approaches

The flow regime in the seal region is highly three-dimensional and shows a predominantly temporal dependency. For the tested turbine stage, experiments are performed with a focus on the aero-thermal flow quantities, as they are expected in the hub side region of the stator-rotor interface and the rotating blade passages. Experimental methods are chosen to capture the dominating spatio-temporal characteristic of the flow in the region of interest.

- The unsteady validation has a qualitative character. As the true time-series of the transducers are finally used for a frequency based analysis, the aerodynamic calibration of the probes, based on phase-locked averages, is entirely disregarded. The qualitative agreement of unsteady pressure measurements and the corresponding spatio-temporal equivalent in the computational results show good agreement. Magnitudes and the distribution of pressure gradients are viewed in different spatio-temporal dimensions. With the side-by-side consideration of experiment and computation, the robustness of the evaluation procedure is proven in the different spatio-temporal coordinate systems.

- Cross-correlating the unsteady pressure signals from inside the cavity provides evidence of the existence of large scale, rotating fluctuations in the seal region (Section 4.1.4). Where the experimental data allowed to develop the procedure, its application to the numerical data then enabled the investigation of the consequences to the entire rotor hub region.

Numerical Approach and Data Processing

Experiments are accompanied by three-dimensional unsteady flow field simulations. Using experimental results at the inlet and outlet of the main annulus as well at the inlet of the cavity, aero-thermal boundary conditions are used to initialize the numerical setups. The computed flow field is validated with experimental results in the stator-rotor interface, within the seal and and at the rotor exit.

- The computational domain is an idealized representation of a 60° segment of the 1.5 stages of the test turbine, in which the seal and the sub-cavity are largely represented (Section 3.2). To enable a good discretization of the rim seal region and the rotor passage, the first stator is strongly de-featured. The advantages coming along with the unsteady computations (to acceptable computational costs) is seen to outweigh the geometrical inaccuracy in the stator. The validity of the computational setup is primarily rated in the prediction of the large-scale rotating fluctuations in the seal region. Concerning the geometrical periodicity (ratio of blade counts), a 30° segment would be sufficient. A small sector however comes along with the restriction of the possible circumferential periodicity of the large scale fluctuations. The 60° sector approach is a tradeoff between circumferential independence and computational costs. The quantification of the rotating structures (Section 4.1.4) highlights the constraining character of the sector approach. For the presented operating point, the computation predicts 12 limbs (2 in each 60° sector) compared to 18 in the experiment. As the model is limited to integral values, one structure will always represent six on the full circle.

- The domain is discretized with 84.4 million volumes (Section 3.2.1). Even with the temporally coarse export resolution of every fourth time-step, the investigated period of two full revolutions lead to 720 files. Exporting only the basic flow variables (flow vector, pressure and temperature), the memory requirement for each configuration exceeds 250 GB. The processing and evaluation of the unsteady flow data with a free choice of the frame of reference and the time-averaging approach is impossible, if the area of interest is not strongly restricted in advance. The spatial down-sampling approach, as applied to the unsteady computational result files, can be the pivotal step in the investigation of large scale unsteady flow phenomena.

A One-Dimensional Framework to Implement Rim Seal Purge Flow to Cycle Prediction

As generally true for the supply of the secondary air system, the purge flow is extracted from the compressor section. In contrast to the main flow, the secondary air bypasses the heat addition in the combustion section influencing the characteristic of the entire thermodynamic cycle of the gas turbine. To consider purge flow in a cycle performance prediction, its influence to the aerothermal turbine performance has to be known or estimated. To implement a specific turbine stage design, a set of one-dimensional stage performance parameters is usually transferred to the cycle prediction.
Based on the first and second law of thermodynamics, an established framework for turbine stage performance ratings, including cooling flows, is concretized to a rim seal injection at the stator-rotor interface. Using unsteady computational fluid dynamic results from the stage, time and space averaged quantities are evaluated at selected

axial and radial positions to present the application of the method.

- A thermodynamically sound formulation of stage efficiency with rim seal injection is presented. Strict definitions of the one-dimensional thermodynamic states of main and purge flow are used to separate the individual stator and rotor blade rows from the area of purge flow introduction (Section 2.2.2). Levels of temperature and entropy are balanced and separated into the individual segments. The portion of unavoidable entropy coming along with the thermal equilibration is considered in the quantification of the aero-thermal rating.

- The concept is first applied to the overall stage (Section 4.2.1). When the purge flow fraction is varied (0, 1 and 2 %), the consideration of a fully reversible mixing process does only marginally alter the stage performance (88.25, 88.58 and 88.65 %). Using the conventional approach though, the stage efficiency drops considerably ((88.30, 87.82 and 87.09 %).

- When the stator is rated separately, the blade row performance is unaffected by the purge flow variation. The enthalpy based total-to-static efficiency is close to 95 % (Section 4.2.2). The level of the rotor blade row performance is approx. 6 % lower, however increases with raising purge flow mass fraction (enthalpy based total-to-static efficiency 87.08, 88.25 and 88.75 %)

- Adjoining the purge flow region to the rotor blade row rating and rating its performance with the adapted model for the cooled stage, the performance decreases, 85.03, 84.28 and 83.19 %, (Section 4.2.3). The implicit treatment of the thermodynamic paths of main and purge flow from their individual inlets to the rotor exit enables a hierarchical decomposition of losses. The introduction of the virtual inlet condition with the fully reversible mixing of main and purge flow allows the differentiation of losses, which are truly chargeable to the aero-thermal performance of the rotor blade row. Furthermore, the steady state energy equation allows to quantify the power induced by wall friction. Appending the seal region to the control volume, the interrelation of pressure loss as well as the total temperature and entropy levels allow an implicit performance rating of the blade-seal configuration. In contrast to a higher order evaluation, the one-dimensional framework has the potential to be integrated into a performance prediction tool. The implementation into an automatic optimization algorithm is possible.

5.3 Outlook

The data reduction method was applied to the entire time-series of the three different unsteady flow simulations. In the scope of this work, the capabilities of the data post processing procedure are only presented rudimentary, where the characterization of the spatio-temporal vortex patterns in the rim seal region is exemplary shown for one

purge flow fraction. The presentation of the possibilities, which are sticked into the reduced data library, are further conducted on the basis of one single phase-locked situation. Consequently, only a fractional amount of the ready-to-use data base is presented in this thesis. Sarcastically spoken, there is an entire unwritten or hidden book, where all the dynamic, time-resolved, three-dimensional sequences are utilized, to generate the ultimate understanding of the spatio-temporal interaction mechanism in the rim seal region. That this will ever occur, is highly unlikely.

During the preparation of this thesis, a large export library was produced, where all kinds of sectional and three-dimensional perspective views of a whole range of flow variables are archived. Where appropriate, they are concatenated to sequences, allowing humans to judge the flow situation intuitively. Nice to watch, however immensely time-consuming. Furthermore, the multi-dimensionality quickly leads to visual overburdening.

So, here is a possible outlook. With the current ongoing explosive development of teaching AI-based models with image sequences, the library is thinkable to be used to train a large scale purge-to-main flow interaction model. Speaking a rudimentary form of the *language of rim seal purge flow*, the model can be further trained on other experimentally and numerically based purge flow data. As highlighted in the fundamentals of this thesis: The potential of an optimized rim seal purge flow system is of global scale, where the entire thermodynamic cycle is seen to be the globe.

List of Figures

List of Tables

List of Symbols

Symbols

Greek	Description	Unit
Λ	degree of reaction	–
T	torque	$\mathrm{N\,m}$
Φ	flow coefficient	–
Ψ	temperature drop coefficient	–
Ω	angular velocity	$\mathrm{rad\,s^{-1}}$
α	absolute whirl angle	rad
β	relative whirl angle	rad
γ	heat capacity ratio	–
ζ	enthalpie loss coefficient	–
η	efficiency	–
θ	maximum temperature ratio	–
θ'	maximum temperature ratio (cooled cycle)	–
μ	normalized cooling flow rate	–
π	pressure ratio	–
τ	compressor temperature ratio (cycle)	–
ψ	coolant mass fraction	–
ω	vorticity	$\mathrm{s^{-1}}$
$\vec{\omega}$	vorticity vector	$\mathrm{s^{-1}}$

Roman	Description	Unit
c_p	specific heat capacity	–
b	seal radius	m
c	velocity in absolute frame of reference	$\mathrm{m\,s^{-1}}$
f	frequency	$\mathrm{s^{-1}}$
h	height	m
h	specific enthalpy	$\mathrm{J\,kg^{-1}}$
m	mass flow	$\mathrm{kg\,s^{-1}}$
n	number of periods	–
n	rotational speed	$\mathrm{s^{-1}}$
p	pressure	Pa
P	power	W
Q	Q-criterion	–
q	specific heat flux	$\mathrm{W\,m^{-2}}$
r	radius	m

(Symbols continued)

R	specific gas constant	$\mathrm{J\,kg^{-1}\,K^{-1}}$
Re	Reynolds number	–
S	static entropy	$\mathrm{J\,K^{-1}}$
s	seal	m
s	static specific entropy	$\mathrm{J\,kg^{-1}\,K^{-1}}$
T	temperature	K
T	period of fluctuation	s
t	time	s
u	velocity of the rotor	$\mathrm{m\,s^{-1}}$
v	specific volume	$\mathrm{m^3\,kg^{-1}}$
v	velocity in relative frame of reference	$\mathrm{m\,s^{-1}}$
w	specific work	$\mathrm{J\,kg^{-1}}$
w	specific work	J
Y	pressure loss coefficient	–

Sub- and Superscripts

Subscripts

1	compressor inlet (cycle)
1	stator inlet
12s	isentropic stator inlet to stator outlet
13s	isentropic stator inlet to rotor outlet
2	compressor outlet (cycle)
2	stator rotor interface
23s	isentropic rotor inlet to rotor outlet
2A	stator outlet
2A3s	isentropic stator out rotor in
2B	rotor inlet
2B3s	isentropic rotor inlet to rotor outlet
3	rotor outlet
3	turbine inlet (cycle)
4	turbine outlet (cycle)
5	turbine inlet (cooled cycle)
5′	isentropic turbine inlet (cooled cycle)
6	turbine outlet (cooled cycle)
9	outlet cooling (cooled cycle)
c	casing
C	cooling inlet
c	clearance
c	compressor
C	cooling air supply
C3s	isentropic cooling inlet to rotor outlet
FR	fully reversible mixing
gen	generated
H	Hartsel's definitions
h	hub
iso	iso-value
m	after mixing
MP	mainstream pressure mixing
n	normalized
p	polytropic
pr	reduced polytropic
R	rotor
r	radial
ref	reference state
rel	rotor relative
RFR	fully reversible mixing - rotor

s	isentropic
S	stator
St	stage
SW	stream-wise
t	turbine
th	thermal efficiency (cycle)
WP	weighted pressure mixing
z	axial
ϕ	circumferential

Superscripts

0	total conditions

Acronyms

Short	Description
1D	one-dimensional
2D	two-dimensional
3D	three-dimensional
5HP	Five Hole Probe
7HP	Seven Hole Probe
AI	Artificial Inteligence
AOI	Area of Interest
ATAG	Air Transport Action Group
BPF	Blade Passing Frequency
BWB	Blended Wing Body
CAD	Computer Aided Design
CAEP	Committee on Aviation Environmental Protection
CCGT	Combined Cycle Gas Turbine
CFD	Computational Fluid Dynamics
CM	Cavity Mode
CMC	Ceramic Matrix Composites
CO_2	Carbon Dioxide
EU	European Union
FFT	Fast Fourier Transformation
GCF	greatest common factor
GHG	greenhouse gas
GLR	Institute of Gas Turbines and Aerospace Propulsion
GTCC	Gas Turbine Combined Cycle
HGP	Hot Gas Path
HPT	high pressure turbine
HV	horseshoe vortex
HVp	pressure side leg of the horseshoe vortex
HVs	suction side leg of the horseshoe vortex
IC	Irreversible Cooled Cycle

(Abbreviations continued)

Short	Description
ICAO	International Civil Aviation Organization
IGES	Initial Graphics Exchange Specification
IU	Irreversible Uncooled Cycle
JBC	Joule-Brayton Cycle
LSTR	Large Scale Turbine Rig
LTAG	Long Term Global Aspirational Goal
ML	Machine Learning
NGV	Nozzle Guide Vane
NO_x	nitrogen oxides
PCF	Purge Control Feature
PR	Pressure Ratio
PV	passage vortex
R&D	Research and Development
RANS	Reynolds averaged Navier-Stokes
RC	Reversible Cooled Cycle
RIT	Rotor Inlet Temperature
RSPF	Rim Seal Purge Flow
RU	Reversible Uncooled Cycle
SAF	Sustainable Aviation Fuels
SAS	Secondary Air System
SFC	Specific Fuel Consumption
SST	Shear Stress Transport
TESV	trailing edge shed vortex
TET	Turbine Entry Temperature
TU	Technical University
UPP	Unsteady Pressure Probe
UPP1	Unsteady Pressure Probe with One Sensor
UPP2	Unsteady Pressure Probe with Two Sensor
URANS	unsteady Reynolds averaged Navier-Stokes

Bibliography

[1] Agora Energiewende (2019). European Energy Transition 2030: The Big Picture. Ten Priorities for the next European Commission to meet the EU's 2030 targets and accelerate towards 2050.

[2] Agora Energiewende (2021). 12 Insights on Hydrogen.

[3] P. Allmann. *Konstruktion einer rotierenden Signalverteilereinheit für den Large Scale Turbine Rig: Design of a rotating signal distributor unit for the Large Scale Turbine Rig*. Bachelor-Thesis, Technische Universität Darmstadt, 2016.

[4] ATAG. waypoiont 2050: Balancing growth in connectivity with a comprehensive global air transport response to the climate emergency: a vision of net-zero aviation by mid-century.

[5] J. Bargon. *Profildruckmessungen an einer Hochdruckturbine für verschiedene Eintrittsbedingungen: Profile Pressure Measurements at a High Pressure Turbine for Different Inlet Conditions*. Bachelor-Thesis, Technische Universität Darmstadt, 2018.

[6] P. F. Beard, F. Gao, K. S. Chana, and J. Chew. Unsteady flow phenomena in turbine rim seals. *Journal of Engineering for Gas Turbines and Power*, 139(3): 032501, 2017. ISSN 0742-4795. doi: 10.1115/1.4034452.

[7] J. Boudet, N. J. Hills, and J. W. Chew. Numerical Simulation of the Flow Interaction Between Turbine Main Annulus and Disc Cavities. In *Proceedings of the ASME Turbo 2006*, pages 553–562. doi: 10.1115/GT2006-90307.

[8] W. J. G. Bräunling. *Flugzeugtriebwerke: Grundlagen, Aero-Thermodynamik, ideale und reale Kreisprozesse, thermische Turbomaschinen, Komponenten, Emissionen und Systeme*. VDI-Buch. Springer Vieweg, Berlin, 4. aufl. edition, 2015. ISBN 3642345395. doi: 10.1007/978-3-642-34539-5.

[9] C. Camci, M. Averbach, and J. Town. Unsteady flow structures within a turbine rim seal cavity in the presence of purge flow—an experimental and computational unsteady aerodynamics investigation. *Aerospace*, 6(5):60, 2019. doi: 10.3390/aerospace6050060.

[10] C. Cao, J. W. Chew, P. R. Millington, and S. I. Hogg. Interaction of rim seal and annulus flows in an axial flow turbine. *Journal of Engineering for Gas Turbines and Power*, 126(4):786, 2004. ISSN 07424795. doi: 10.1115/1.1772408.

[11] J. W. Chew, F. Gao, and D. M. Palermo. Flow mechanisms in axial turbine rim sealing. *Proceedings of the Institution of Mechanical Engineers, Part C: Journal of Mechanical Engineering Science*, 233(23-24):7637–7657, 2019. ISSN 0954-4062. doi: 10.1177/0954406218784612.

[12] M. Chilla, H. Hodson, and D. Newman. Unsteady interaction between annulus and turbine rim seal flows. *Journal of Turbomachinery*, 135(5):51024, 2013. ISSN 0889-504X. doi: 10.1115/1.4023016.

[13] M. Chilla, H. P. Hodson, G. Pullan, and D. Newman. High-pressure turbine rim seal design for increased efficiency. In *ASME Turbo Expo 2016*, page V02BT38A046, New York, N.Y., 2016. ASME. ISBN 978-0-7918-4970-5. doi: 10.1115/GT2016-57495.

[14] COM(2020a). Communication from the commission to the european parliament, the council, the european economic and social committee and the committee of the regions: Powering a climate-neutral economy: An eu strategy for energy system integration.

[15] J. D. Denton. The 1993 igti scholar lecture: Loss mechanisms in turbomachines. *Journal of Turbomachinery*, 115(4):621–656, 1993. ISSN 0889-504X. doi: 10.1115/1.2929299.

[16] J. Eitenmüller, M. Wilhelm, L. Gresser, T. Ostrowksi, S. Leichtfuss, H.-P. Schiffer, C. Lyko, and S. Naik. Highly accurate delta efficiency measurements at the large scale turbine rig. In *Proceedings of the ASME Turbo Expo 2019*, New York, N.Y. ISBN 978-0-7918-5856-1. doi: 10.1115/GT2019-90294.

[17] M. A. El-Masri. On thermodynamics of gas-turbine cycles: Part 1—second law analysis of combined cycles. *Journal of Engineering for Gas Turbines and Power*, 107(4):880–889, 1985. ISSN 07424795. doi: 10.1115/1.3239832.

[18] M. A. El-Masri. On thermodynamics of gas-turbine cycles: Part 2—a model for expansion in cooled turbines. *Journal of Engineering for Gas Turbines and Power*, 108(1):151–159, 1986. ISSN 07424795. doi: 10.1115/1.3239862.

[19] A. Filius. *Experimental Investigation of the Transient Interaction between Main Annulus Flow and Seal Air in an Axial Turbine with High Inlet Swirl: Experimentelle Untersuchung der instationären Interaktion zwischen Hauptstrom und Sperrluft an einer Axialturbine unter dem Einfluss von stark verdrallter Zuströmung*. Master-Thesis, Technische Universität Darmstadt, 2018.

[20] Y. Fischer. *Anwendung der Infrarotthermographie zur Analyse des Wärmeübergangs auf der Rotorendwand einer Axialturbine: Application of Infrared Thermography for the Analysis of Heat Transfer on the Rotor Endwall of an Axial Turbine*. Master-Thesis, Technische Universität Darmstadt, 2019.

[21] P. Gaetani and G. Persico. Influence of the Rotor-Driven Perturbation on the Stator-Exit Flow within a High-Pressure Gas Turbine Stage. *International Journal of Turbomachinery, Propulsion and Power*, 6(3):28, 2021. doi: 10.3390/ijtpp6030028.

[22] F. Gao, J. Chew, P. Beard, D. Amirante, and N. Hills. Numerical studies of turbine rim sealing flows on a chute seal configuration. In *European Conference on Turbomachinery Fluid Dynamics and Thermodynamics*, 2017. doi: 10.29008/ETC2017-284.

[23] S. C. Gülen. *Gas turbines for electric power generation*. Cambridge University Press, Cambridge and New York, NY, 2019. ISBN 9781108241625. doi: 10.1017/9781108241625.

[24] S. C. Gülen. *Gas Turbine Combined Cycle Power Plants*. CRC Press LLC, Boca Raton, 2019. ISBN 9780429244360. doi: 10.1201/9780429244360.

[25] D. D. Hänni, R. S. Abhari, R. Schädler, A. I. Kalfas, G. Schmid, E. Lutum, and N. Lecoq. Purge flow effects on rotor hub endwall heat transfer with extended endwallcontouring into the disk cavity. In *Global Power and Propulsion Zurich19: Technical Conference*, GPPS Zurich19. GPPS, 2019. doi: 10.33737/GPPS19-TC-014.

[26] J. Hartsel. Prediction of effects of mass-transfer cooling on the blade-row efficiency of turbine airfoils. In *10th Aerospace Sciences Meeting*, Reston, Virigina, 1972. American Institute of Aeronautics and Astronautics. doi: 10.2514/6.1972-11.

[27] W. R. Hawthorne. The thermodynamics of cooled turbines: Part 1—the turbine stage. *Journal of Fluids Engineering*, 78(8):1765–1779, 1956. ISSN 00982202. doi: 10.1115/1.4014181.

[28] W. R. Hawthorne. The thermodynamics of cooled turbines: Part 2—the multistage turbine. *Journal of Fluids Engineering*, 78(8):1781–1785, 1956. ISSN 00982202. doi: 10.1115/1.4014182.

[29] J. H. Horlock. The basic thermodynamics of turbine cooling. *Journal of Turbomachinery*, 123(3):583–592, 2001. ISSN 0889-504X. doi: 10.1115/1.1370156.

[30] J. H. Horlock. *Advanced Gas Turbine Cycles*. Elsevier, 2003. ISBN 9780080442730. doi: 10.1016/B978-0-08-044273-0.X5000-7.

[31] J. T. M. Horwood, F. P. Hualca, M. Wilson, J. A. Scobie, C. M. Sangan, and G. D. Lock. Unsteady Computation of Ingress Through Turbine Rim Seals. In *ASME Turbo Expo 2018: Turbomachinery Technical Conference and Exposition*, 2018. doi: 10.1115/GT2018-75321.

[32] F. P. Hualca, J. T. M. Horwood, C. M. Sangan, G. D. Lock, and J. A. Scobie. The effect of vanes and blades on ingress in gas turbines. *Journal of Engineering for Gas Turbines and Power*, 142(2), 2020. ISSN 0742-4795. doi: 10.1115/1.4045149.

[33] ICAO. Environmental report 2019: Destination green the next chapter, .

[34] ICAO. Report on the feasibility of a long-term aspirational goal (ltag) for international civil aviation co2 emission reductions, .

[35] ICAO. Report on the feasibility of a long-term aspirational goal (ltag) for international civil aviation co2 emission reductions: Appendix m3 - technology sub group report, .

[36] ICAO. Report on the feasibility of a long-term aspirational goal (ltag) for international civil aviation co2 emission reductions: Appendix r1 - summary sheets, .

[37] V. Iranidokht, A. Kalfas, R. Abhari, S. Senoo, and K. Momma. Sensitivity analysis on the impact of geometrical and operational variations on turbine hub cavity modes and practical methods to control them. *Journal of the Global Power and Propulsion Society*, 5:66–78, 2021a. doi: 10.33737/jgpps/133736.

[38] V. Iranidokht, N. Purwar, A. I. Kalfas, R. S. Abhari, and S. Senoo. Turbine hub cavity modes and their impact on efficiency. *Journal of Turbomachinery*, 143(3), 2021b. ISSN 0889-504X. doi: 10.1115/1.4050110.

[39] R. Jakoby, T. Zierer, K. Lindblad, J. Larsson, L. deVito, D. E. Bohn, J. Funcke, and A. Decker. Numerical simulation of the unsteady flow field in an axial gas turbine rim seal configuration. In *ASME Turbo Expo 2004: Power for Land, Sea, and Air*, pages 431–440, 2004. doi: 10.1115/GT2004-53829.

[40] P. Jenny, R. S. Abhari, M. G. Rose, M. Brettschneider, K. Engel, and J. Gier. Unsteady rotor hub passage vortex behavior in the presence of purge flow in an axial low pressure turbine. *Journal of Turbomachinery*, 135(5), 2013. ISSN 0889504X. doi: 10.1115/1.4007837.

[41] J. Jeong and F. Hussain. On the identification of a vortex. *Journal of Fluid Mechanics*, 285:69–94, 1995. ISSN 0022-1120.

[42] S. Julien, J. Lefrancois, G. Dumas, G. Boutet-Blais, S. Lapointe, J.-F. Caron, and R. Marini. Simulations of flow ingestion and related structures in a turbine disk cavity. In *Proceedings of the ASME Turbo Expo 2010*, pages 1071–1080, New York, NY, 2010. ASME. ISBN 978-0-7918-4399-4. doi: 10.1115/GT2010-22729.

[43] A. Krichbaum, H. Werschnik, M. Wilhelm, H.-P. Schiffer, and K. Lehmann. A large scale turbine test rig for the investigation of high pressure turbine aerodynamics and heat transfer with variable inflow conditions. In *ASME Turbo Expo 2015*, page V02AT38A032, New York, N.Y., 2015. ASME. ISBN 978-0-7918-5663-5. doi: 10.1115/GT2015-43261.

[44] J. Kurzke and I. Halliwell. *Propulsion and Power: An Exploration of Gas Turbine Performance Modeling*. Springer International Publishing AG, Cham, 2018. ISBN 9783319759791.

[45] L. S. Langston. Secondary flows in axial turbines–a review. *Annals of the New York Academy of Sciences*, 934:11–26, 2001. ISSN 1749-6632. doi: 10.1111/j.1749-6632.2001.tb05839.x.

[46] L. S. Langston, M. L. Nice, and R. M. Hooper. Three-dimensional flow within a turbine cascade passage. *Journal of Engineering for Power*, 99(1):21–28, 1977. ISSN 00220825. doi: 10.1115/1.3446247.

[47] S. Lazzi Gazzini, R. Schädler, A. I. Kalfas, R. S. Abhari, S. Hohenstein, G. Schmid, and E. Lutum. Effect of Purge Air on Rotor Endwall Heat Transfer of an Axial Turbine. In *Proceedings of the 1st Global Power and Propulsion Forum*, volume GPPF-2017-95.

[48] S. Lazzi Gazzini, R. Schädler, A. I. Kalfas, and R. S. Abhari. Infrared thermography with non-uniform heat flux boundary conditions on the rotor endwall of an axial turbine. *Measurement Science and Technology*, 28(2):025901, 2017. ISSN 0957-0233. doi: 10.1088/1361-6501/aa5174.

[49] T. Ostrowski and H.-P. Schiffer. Aerothermische interaktion zwischen brennkammer und turbine: Rotorplattform : Schlussbericht : Verbundprojekt: Ag turbo cooreflex-turbo, vorhaben-nr.: 3.1.2 : Zeitraum: 01. august 2015-31. dezember 2019, 2020.

[50] T. Ostrowski and H.-P. Schiffer. High-resolution heat transfer measurements on a rotating turbine endwall with infrared thermography. *Measurement Science and Technology*, 32(12):125207, 2021. ISSN 0957-0233. doi: 10.1088/1361-6501/ac2553. URL `https://iopscience.iop.org/article/10.1088/1361-6501/ac2553`.

[51] T. Ostrowski and H.-P. Schiffer. Investigation of large scale unsteady rim seal flow structures and their influence on the rotor hub side endwall heat transfer. In *Global Power and Propulsion Technical Conference Chania 2022*, 2022. doi: 10.33737/gpps22-tc-26.

[52] D. M. Palermo, F. Gao, J. W. Chew, and P. F. Beard. Effect of annulus flow conditions on turbine rim seal ingestion. In *Proceedings of the ASME Turbo Expo: Turbomachinery Technical Conference and Exposition -2019-*, New York, N.Y., 2019. The American Society of Mechanical Engineers. ISBN 978-0-7918-5865-3. doi: 10.1115/GT2019-90489.

[53] A. Polidar. *Zeitaufgelöste Vermessung der Rotorabströmung einer Axialturbine unter Anwendung einer virtuellen Vierlochsonde: Time-Resolved Investigation of the Rotor Exit Flow Field of an Axial Turbine Based on a Virtual Four-Hole Probe*. Bachelor-Thesis, Technische Universität Darmstadt, 2018.

[54] H. Rick. *Gasturbinen und Flugantriebe: Grundlagen, Betriebsverhalten und Simulation*. VDI-Buch. Springer Berlin Heidelberg, 2013. ISBN 9783540794462.

[55] W. M. Rohsenow. Effect of turbine-blade cooling on efficiency of a simple gas-turbine power plant. *Journal of Fluids Engineering*, 78(8):1787–1793, 1956. ISSN 00982202. doi: 10.1115/1.4014184.

[56] A. Roy, J. Fridh, J. Scobie, C. Sangan, and G. Lock. Flow instability effects related to purge through a gas turbine chute seal. *Journal of the Global Power and Propulsion Society*, 5:111–125, 2021. doi: 10.33737/jgpps/140172.

[57] C. M. Sangan, O. J. Pountney, K. Zhou, M. Wilson, J. Michael Owen, and G. D. Lock. Experimental Measurements of Ingestion Through Turbine Rim Seals—Part I: Externally Induced Ingress. *Journal of Turbomachinery*, 135(2):021012, 2013. ISSN 0889504X. doi: 10.1115/1.4006609.

[58] H. I. H. Saravanamuttoo, G. F. C. Rogers, H. Cohen, P. Straznicky, and A. Nix. *Gas turbine theory*. Pearson, Harlow and New York and Toronto, 7th edition edition, 2017. ISBN 9781292093093.

[59] R. Schädler, A. I. Kalfas, R. S. Abhari, G. Schmid, and S. Voelker. Modulation and radial migration of turbine hub cavity modes by the rim seal purge flow. *Journal of Turbomachinery*, 139(1):011011, 2017. ISSN 0889-504X. doi: 10.1115/1.4034416.

[60] P. Schüpbach, R. S. Abhari, M. G. Rose, T. Germain, I. Raab, and J. Gier. Effects of suction and injection purge-flow on the secondary flow structures of a high-work turbine. In *ASME Turbo Expo 2008: Power for Land, Sea, and Air*, pages 1135–1145, 2008. doi: 10.1115/GT2008-50471.

[61] J. A. Scobie, C. M. Sangan, J. Michael Owen, and G. D. Lock. Review of ingress in gas turbines. *Journal of Engineering for Gas Turbines and Power*, 138(12):120801, 2016. ISSN 07424795. doi: 10.1115/1.4033938.

[62] A. H. Shapiro. *The dynamics and thermodynamics of compressible fluid flow: In two volumes*, volume 1. Ronald Press, New York, 1953.

[63] J. H. Spurk and N. Aksel. *Strömungslehre: Einführung in die Theorie der Strömungen ; mit Aufgaben und Übungsbeispielen auf CD-ROM*. Springer, Berlin u.a, 6., erw. aufl edition, 2006. ISBN 3-540-26293-8.

[64] P. Stephan, K. Schaber, K. Stephan, and F. Mayinger. *Thermodynamik*. Springer Berlin Heidelberg, Berlin, Heidelberg, 2009. ISBN 978-3-540-92894-2.

[65] W. Traupel. *Thermische Turbomaschinen*. Klassiker der Technik. Springer, Berlin, 4. aufl. edition, 2001. ISBN 978-3-642-62102-4. doi: 10.1007/978-3-642-17469-8.

[66] H. Werschnik, J. Hilgert, M. Wilhelm, M. Bruschewski, and H.-P. Schiffer. Influence of combustor swirl on endwall heat transfer and film cooling effectiveness at the large scale turbine rig. *Journal of Turbomachinery*, 139(8):081007, 2017. ISSN 0889-504X. doi: 10.1115/1.4035832.

[67] M. Wilhelm. *Aerothermal Impact of Low Emission Combustion on the Turbine Blade Tip*. Dissertation, Technische Universität Darmstadt, 2020.

[68] D. Woelki. *Modulated Secondary Air Systems for Modulated Secondary Air Systems for Enhanced Off-Design Operation of Stationary Gas Turbines and Aero Engines*. Dissertation, Technische Universität Berlin, 2022.

[69] J. B. Young and J. H. Horlock. Defining the efficiency of a cooled turbine. *Journal of Turbomachinery*, 128(4):658–667, 2006. ISSN 0889-504X. doi: 10.1115/1.2218890.

[70] J. B. Young and R. C. Wilcock. Modeling the air-cooled gas turbine: Part 1—general thermodynamics. *Journal of Turbomachinery*, 124(2):207–213, 2002. ISSN 0889-504X. doi: 10.1115/1.1415037.

[71] Y. Zhou, S. Searle, and N. Pavlenko. Current and future cost of e-kerosene in the united states and europe: Working paper 2022-14.